STATE OF THE CLIMATE IN 2022

THE ARCTIC

T. A. Moon, R. Thoman, and M. L. Druckenmiller, Eds.

Special Online Supplement to the *Bulletin of the American Meteorological Society* Vol. 104, No. 9, September, 2024

https://doi.org/10.1175/BAMS-D-23-0079.1

Corresponding author: Twila Moon / Twila.Moon@colorado.edu

STATE OF THE CLIMATE IN 2022

The Arctic

Editors

Ellen Bartow-Gillies
Jessica Blunden
Tim Boyer

Chapter Editors

Peter Bissolli
Kyle R. Clem
Howard J. Diamond
Matthew L. Druckenmiller
Robert J. H. Dunn
Catherine Ganter
Nadine Gobron
Gregory C. Johnson
Rick Lumpkin
Ademe Mekonnen
John B. Miller
Twila A. Moon
Marilyn N. Raphael
Ahira Sánchez-Lugo
Carl J. Schreck III
Richard L. Thoman
Kate M. Willett
Zhiwei Zhu

Technical Editor

Lukas Noguchi

BAMS Special Editor for Climate

Michael A. Alexander

American Meteorological Society

Cover Credit:
Patterned Ground in the Arctic by Ina Timling.

Ice wedge polygons are a common form of patterned ground in the Arctic. They occur in areas of continuous permafrost, such as the arctic coastal plain of Alaska, and are the result of freeze-thaw processes. These polygons create striking patterns on the landscape and provide habitats for many organisms. However, increased warming of the Arctic leads to the degradation/thawing of these ice wedges. As a result, not only the appearance of the patterned ground features changes but also their function as habitat.

How to cite this document:
The Arctic is one chapter from the *State of the Climate in 2022* annual report and is available from https://doi.org/10.1175/BAMS-D-23-0079.1. Compiled by NOAA's National Centers for Environmental Information, *State of the Climate in 2022* is based on contributions from scientists from around the world. It provides a detailed update on global climate indicators, notable weather events, and other data collected by environmental monitoring stations and instruments located on land, water, ice, and in space. The full report is available from https://doi.org/10.1175/2023BAMSStateoftheClimate.1.

Citing the complete report:
Blunden, J., T. Boyer, and E. Bartow-Gillies, Eds., 2024: "State of the Climate in 2022". Bull. Amer. Meteor. Soc., 104 (9), Si–S501 https://doi.org/10.1175/2023BAMSStateoftheClimate.1.

Citing this chapter:
Moon, T. A., R. Thoman, and M. L. Druckenmiller, Eds., 2024: The Arctic [in "State of the Climate in 2022"]. Bull. Amer. Meteor. Soc., 104 (9), S271–S321, https://doi.org/10.1175/BAMS-D-23-0079.1.

Citing a section (example):
Walsh, J. E., S. Bigalke, S. A. McAfee, R. Lader, M. C. Serreze, and T. J. Ballinger, 2023: Precipitation [in "State of the Climate in 2022"]. Bull. Amer. Meteor. Soc., 104 (9), S281–S284, https://doi.org/10.1175/BAMS-D-23-0079.1.

Editor and Author Affiliations (alphabetical by name)

Ahmasuk, Brandon, Kawerak Inc., Nome, Alaska

Backensto, Stacia A., National Park Service, Fairbanks, Alaska

Ballinger, Thomas J., International Arctic Research Center, University of Alaska Fairbanks, Fairbanks, Alaska

Benestad, Rasmus, Norwegian Meteorological Institute, Oslo, Norway

Berner, Logan. T., Northern Arizona University, Flagstaff, Arizona

Bernhard, Germar H., Biospherical Instruments Inc., San Diego, California

Bhatt, Uma S., Geophysical Institute, University of Alaska Fairbanks, Fairbanks, Alaska

Bigalke, Siiri, Plant, Soils and Climate Department, Utah State University, Logan, Utah

Bjerke Jarle, W., Department of Arctic Ecology, Norwegian Institute for Nature Research, Trondheim, Norway

Brettschneider, Brian, NOAA/NWS Alaska Region, Anchorage, Alaska

Christiansen, Hanne H., Geology Department, University Centre in Svalbard, Svalbard, Norway

Cohen, Judah L., Atmospheric and Environmental Research, Lexington, Massachusetts

Decharme, Bertrand, Centre National de Recherches Météorologiques, Météo-France/CNRS, Toulouse, France

Derksen, Chris, Climate Research Division, Environment and Climate Change Canada, Toronto, Canada

Divine, Dmitry, Norwegian Polar Institute, Fram Centre, Tromso, Norway

Drost Jensen, Caroline, Danish Meteorological Institute, Copenhagen, Denmark

Druckenmiller, Matthew L., National Snow and Ice Data Center, Cooperative Institute for Research in Environmental Sciences, University of Colorado, Boulder, Colorado

Elias Chereque, Alesksandra, Department of Physics, University of Toronto, Toronto, Canada

Epstein, Howard E., University of Virginia, Charlottesville, Virginia

Fausto, Robert S., Geological Survey of Denmark and Greenland (GEUS), Copenhagen, Denmark

Fettweis, Xavier, University of Liège, Belgium

Fioletov, Vitali E., Environment and Climate Change Canada, Toronto, Canada

Forbes, Bruce C., Arctic Centre, University of Lapland, Rovaniemi, Finland

Frost, Gerald V. (JJ), ABR Inc., Fairbanks, Alaska

Gerland, Sebastian, Norwegian Polar Institute, Fram Centre, Tromso, Norway

Goetz, Scott J., Northern Arizona University, Flagstaff, Arizona

Grooß, Jens-Uwe, Forschungszentrum Jülich, Jülich, Germany

Hanna, Edward, Department of Geography and Lincoln Climate Research Group, Lincoln, United Kingdom

Hanssen-Bauer, Inger, Norwegian Meteorological Institute, Oslo, Norway

Hendricks, Stefan, Alfred Wegener Institute, Helmholtz Centre for Polar and Marine Research, Bremerhaven, Germany

Holmes, Robert M., Woodwell Climate Research Center, Falmouth, Massachusetts

Ialongo, Iolanda, Finnish Meteorological Institute, Helsinki, Finland

Isaksen, Ketil, Norwegian Meteorological Institute, Oslo, Norway

Johnsen, Bjørn, Norwegian Radiation and Nuclear Safety, Østerås, Norway

Jones, Timothy, Coastal Observation and Seabird Survey Team, University of Washington, Seattle, Washington

Kaler, Robb S.A., U.S. Fish and Wildlife Service, Alaska Region, Anchorage, Alaska

Kaleschke, Lars, Alfred Wegener Institute, Helmholtz Centre for Polar and Marine Research, Bremerhaven, Germany

Kim, Seong-Joong, Korea Polar Research Institute, Incheon, South Korea

Labe, Zachary M., Princeton University, Princeton, New Jersey

Lader, Rick, International Arctic Research Center, University of Alaska Fairbanks, Fairbanks, Alaska

Lakkala, Kaisa, Finnish Meteorological Institute, Sodankylä, Finland

Lara, Mark J., University of Illinois at Urbana-Champaign, Urbana, Illinois

Lindsey, Jackie, Coastal Observation and Seabird Survey Team, University of Washington, Seattle, Washington

Loomis, Bryant D., NASA Goddard Space Flight Center, Greenbelt, Maryland

Luojus, Kari, Arctic Research Centre, Finnish Meteorological Institute, Helsinki, Finland

Macander, Matthew J., ABR Inc., Fairbanks, Alaska

Mamen, Jostein, Norwegian Meteorological Institute, Oslo, Norway

Mankoff, Ken D., Business Integra, New York, New York; NASA Goddard Institute for Space Studies, New York, New York

Manney, Gloria L., NorthWest Research Associates, Socorro, New Mexico

McAfee, Stephanie A., Department of Geography, University of Nevada Reno, Reno, Nevada

McClelland, James W., Marine Biological Laboratory, Woods Hole, Massachusetts

Meier, Walter N., National Snow and Ice Data Center, Cooperative Institute for Research in Environmental Sciences, University of Colorado, Boulder, Colorado

Moon, Twila A., National Snow and Ice Data Center, Cooperative Institute for Research in Environmental Sciences, University of Colorado, Boulder, Colorado

Moore, G. W. K., University of Toronto Mississauga, Mississauga, Canada

Mote, Thomas L., University of Georgia, Athens, Georgia

Mudryk, Lawrence, Climate Research Division, Environment and Climate Change Canada, Toronto, Canada

Müller, Rolf, Forschungszentrum Jülich, Jülich, Germany

Nyland, Kelsey E., Department of Geography, George Washington University, Washington, DC

Overland, James E., NOAA Pacific Marine Environmental Laboratory, Seattle, Washington

Parrish, Julia K., Coastal Observation and Seabird Survey Team, University of Washington, Seattle, Washington

Perovich, Donald K., University of Dartmouth, Hanover, New Hampshire

Petersen, Guðrún Nína, Icelandic Meteorological Office, Reykjavik, Iceland

Petty, Alek, NASA Goddard Space Flight Center, Greenbelt, Maryland

Phoenix, Gareth, K., University of Sheffield, Sheffield, United Kingdom

Poinar, Kristin, University at Buffalo, Buffalo, New York

Rantanen, Mika, Finnish Meteorological Institute, Helsinki, Finland

Ricker, Robert, NORCE Norwegian Research Centre, Tromso, Norway

Romanovsky, Vladimir E., Geophysical Institute, University of Alaska Fairbanks, Fairbanks, Alaska; Earth Cryosphere Institute, Tyumen Science Center, Tyumen, Russia

Serbin, Shawn P., Brookhaven National Laboratory, Upton, New York

Serreze, Mark C., National Snow and Ice Data Center, University of Colorado, Boulder, Colorado

Sheffield, Gay, Alaska Sea Grant, Marine Advisory Program, University of Alaska Fairbanks, Nome, Alaska

Shiklomanov, Alexander I., University of New Hampshire, Durham, New Hampshire; Arctic and Antarctic Research Institute, St. Petersburg, Russia

Shiklomanov, Nikolay I., Department of Geography, George Washington University, Washington, DC

Smith, Sharon L., Geological Survey of Canada, Natural Resources Canada, Ottawa, Canada

Editor and Author Affiliations (continued)

Spencer, Robert G. M., Florida State University, Tallahassee, Florida
Streletskiy, Dmitry A., Department of Geography, George Washington University, Washington, DC
Suslova, Anya, Woodwell Climate Research Center, Falmouth, Massachusetts
Svendby, Tove, Norwegian Institute for Air Research, Kjeller, Norway
Tank, Suzanne E., University of Alberta, Edmonton, Canada
Tedesco, Marco, Lamont-Doherty Earth Observatory, Columbia University, Palisades, New York; NASA Goddard Institute of Space Studies, New York, New York
Thoman, Richard L., International Arctic Research Center, University of Alaska Fairbanks, Fairbanks, Alaska
Tian-Kunze, Xiangshan, Alfred Wegener Institute, Helmholtz Centre for Polar and Marine Research, Bremerhaven, Germany
Timmermans, Mary-Louise, Yale University, New Haven, Connecticut
Tømmervik, Hans, Arctic Department, Norwegian Institute for Nature Research, Tromsø, Norway
Tretiakov, Mikhail, Arctic and Antarctic Research Institute, St. Petersburg, Russia
Walker, Donald (Skip) A., Institute of Arctic Biology, University of Alaska Fairbanks, Fairbanks, Alaska
Walsh, John E., International Arctic Research Center, University of Alaska Fairbanks, Fairbanks, Alaska
Wang, Muyin, NOAA Pacific Marine Environmental Laboratory, Seattle, Washington; Cooperative Institute for Climate, Ocean, and Ecosystem Studies, University of Washington, Seattle, Washington
Webster, Melinda, University of Washington, Seattle, Washington
Wehrlé, Adrian, University of Zürich, Zürich, Switzerland
Yang, Dedi, Environmental and Climate Sciences Department, Brookhaven National Laboratory, Upton, New York; Department of Ecology and Evolution, Stony Brook University, Stony Brook, New York
Zolkos, Scott, Woodwell Climate Research Center, Falmouth, Massachusetts

Editorial and Production Team

Allen, Jessicca, Graphics Support, Cooperative Institute for Satellite Earth System Studies, North Carolina State University, Asheville, North Carolina
Camper, Amy V., Graphics Support, Innovative Consulting and Management Services, LLC, NOAA/NESDIS National Centers for Environmental Information, Asheville, North Carolina
Haley, Bridgette O., Graphics Support, NOAA/NESDIS National Centers for Environmental Information, Asheville, North Carolina
Hammer, Gregory, Content Team Lead, Communications and Outreach, NOAA/NESDIS National Centers for Environmental Information, Asheville, North Carolina
Love-Brotak, S. Elizabeth, Lead Graphics Production, NOAA/NESDIS National Centers for Environmental Information, Asheville, North Carolina
Ohlmann, Laura, Technical Editor, Innovative Consulting and Management Services, LLC, NOAA/NESDIS National Centers for Environmental Information, Asheville, North Carolina
Noguchi, Lukas, Technical Editor, Innovative Consulting and Management Services, LLC, NOAA/NESDIS National Centers for Environmental Information, Asheville, North Carolina
Riddle, Deborah B., Graphics Support, NOAA/NESDIS National Centers for Environmental Information, Asheville, North Carolina
Veasey, Sara W., Visual Communications Team Lead, Communications and Outreach, NOAA/NESDIS National Centers for Environmental Information, Asheville, North Carolina

5. Table of Contents

Please refer to Chapter 8 (Relevant Datasets and Sources) for a list of all climate variables and datasets used in this chapter for analyses, along with their websites for more information and access to the data.

5. THE ARCTIC

T. A. Moon, R. Thoman, and M. L. Druckenmiller, Eds.

a. Overview

—T. A. Moon, R. Thoman, and M. L. Druckenmiller

Rapid warming due to human-caused climate change is reshaping the Arctic, enhanced by physical processes that cause the Arctic to warm more quickly than the global average, collectively called Arctic amplification. Observations over the past 40+ years show a transition to a wetter Arctic, with seasonal shifts and widespread disturbances influencing the flora, fauna, physical systems, and peoples of the Arctic.

For the Arctic (poleward of 60°N), 2022 surface air temperatures were the fifth highest since records began in 1900, reaching 0.76°C above the 1991–2020 mean. Evidence of Arctic amplification is becoming more consistent, with 2022 being the ninth consecutive year with Arctic temperature anomalies exceeding global mean anomalies. Higher up in the atmosphere, 2022 saw a greater loss of stratospheric ozone compared to the 2004–21 mean, but not approaching the record losses of 2011 and 2020.

Aligning with climate change projections (IPCC 2021), near-surface air over land had higher temperature anomalies in 2022 than air over the ocean, yet oceanic impacts of global warming are also evident. August mean sea-surface temperatures reveal that most ice-free regions of the Arctic Ocean show warming trends since 1982. Regional exceptions fail to counter a narrative of recent, rapid warming; the 1982–2022 cooling trend for the Barents Sea is notably influenced by anomalously high sea-surface temperatures in the 1980s and 1990s. One ecosystem impact of increasing sea-surface temperatures is an increase in ocean primary productivity, which has been observed since 2003 and was especially strong in the Eurasian Arctic and Barents Sea (Frey et al. 2022).

Continued low sea-ice extent is a contributor to warming ocean surface waters. Arctic sea-ice extent in 2022 was similar to 2021 and remains well below the long-term average. Moving beyond sea-ice extent to sea-ice age, which is related to sea-ice thickness (older sea ice is thicker), reveals more sobering observations. The Arctic has transitioned from a region dominated by multiyear ice to one dominated by first-year (seasonal) sea ice. While sea ice greater than four years old covered over 1 million km^2 in September 2006, it covered only 127,000 km^2 in September 2022. One impact likely connected to increased high-latitude ocean temperatures and reduced sea ice is the repeated recent instances of observed seabird die-offs along coastal Alaska (see Sidebar 5.2). This and other ecosystem impacts, including climate-related changes in fish, marine mammals, and land-based food sources, are a grave concern to Arctic Indigenous Peoples and residents as a matter of food security and ecosystem health (e.g., SEARCH et al. 2022; Crozier et al. 2021; Mallory and Boyce 2018).

Arctic warming has been accompanied by an increase in precipitation. This *State of the Climate* report represents the first time that the Arctic chapter includes a full section on precipitation (section 5c), supported by reanalysis data that allow a pan-Arctic assessment despite sparse in situ gauge measurements. Since 1950, every season has shown an average increase in Arctic precipitation, in line with climate model projections (IPCC 2021). In some regions, the increase in precipitation is experienced through heavier precipitation events (e.g., Arctic Atlantic sector), while for others there has been an increase in the number of consecutive wet days (e.g., Svalbard eastward to the Chukchi Sea).

Increases in precipitation, combined with warming, are linked to altered seasonal patterns. Although April 2022 snow accumulation was higher than the 1991–2020 average for both the Eurasian and North American Arctic, snow-cover extent by June 2022 dipped to the second lowest for the North American Arctic and third lowest for the Eurasian Arctic in the 56-year record. Seasonal shifts also complicate the story of Arctic river discharge. Overall, Arctic river discharge is increasing, consistent with the observations of increasing precipitation and intensification of the Arctic hydrologic cycle. When examining eight major Arctic river basins, 2021 discharge and 2022 discharge exceeded the 1991–2020 mean by 7% and 5%, respectively. Yet, 2021 and 2022 discharges in June (the month of peak discharge) were remarkably low for the Arctic's Eurasian river basins. In another example, despite 2022 glacial ice loss (totaling 165±18 Gt) that was slightly below the 2002–22 average, the Greenland Ice Sheet experienced unprecedented September melt events, bringing melt conditions to 36% of the ice sheet surface during a month that is usually marked by a return to cold conditions and snow accumulation.

Warming air and longer snow-free periods both contribute to continued overall increases in Arctic permafrost temperatures. Continuous and discontinuous permafrost (frozen ground) underlies almost all of the Arctic, and effects of thawing permafrost include infrastructure damage, river discharge changes, ecosystem composition alterations, and releases of greenhouse gases to the atmosphere. Permafrost temperatures in 2022 were the highest on record at 11 of 25 long-term measurement sites. Thirteen sites, however, showed cooling for 2022 compared to 2021 due to short-term reductions in regional air temperatures, demonstrating the importance of long-term monitoring.

As the Arctic subsurface changes, so too does the surface landscape itself. Arctic tundra greenness declined in 2022 from record-high 2020 and 2021 values, yet was still fourth highest across a 23-year record. But, as with other measurements of environmental change, regional variation remains an important part of the story. In this case, low productivity in northeastern Siberia was observed alongside high productivity in most of the North American Arctic.

One of the elements contributing to regional variability and the differing local experiences of Arctic residents is an increase in extreme events, which can include record-setting rainfall or snowfall, heatwaves, wildfire, and cyclones (see Sidebar 5.1). In 2022, 56 separate extreme events were recorded by Arctic-connected meteorological services, with impacts felt by communities throughout the Arctic. Of course, the Arctic is also undergoing changes beyond those discussed in this chapter. For example, coastal erosion (Brady and Leichenko 2020; Irrgang et al. 2022; Nielsen et al. 2022) and biological changes across fauna (Davidson et al. 2020) are impacting Arctic residents (SEARCH et al. 2022) and the connected physical-biological-human systems. There is no doubt that the Arctic is a region of rapid change with serious consequences across systems.

Special Note: This chapter includes a focus on Arctic river discharge, section 5h, which alternates yearly with a section on glaciers and ice caps outside of Greenland, as the scales of regular observation for both of these climate components are better suited for reporting every two years. Note that most Arctic chapter observations now use a 1991–2020 climate baseline (exceptions are noted) updated from 1981–2010, meaning the long-term average now includes more years with stronger climate change influence. Due to different disciplinary norms and physical processes, seasonal definitions also vary and are defined within each chapter section.

b. Surface air temperature

—T. J. Ballinger, J. E. Overland, M. Wang, J. E. Walsh, B. Brettschneider, R. L. Thoman, U. S. Bhatt, E. Hanna, I. Hanssen-Bauer, and S.-J. Kim

1. OVERVIEW

Relative to global mean temperatures, Arctic temperatures have warmed more rapidly since the start of the record in 1900 (Fig. 5.1). The amplified warming of Earth's northernmost latitudes, known as Arctic amplification (AA), is associated with various localized land–ocean–sea-ice interactions and large-scale atmospheric and oceanic energy transport processes (Previdi et al. 2021) that drive impactful Arctic atmospheric extremes (Walsh et al. 2020). Recent research has emphasized that the magnitude of AA is sensitive to multiple constraints, including how the southern limit of the Arctic region is defined, which datasets (i.e., observational versus modeled) are analyzed, and what time periods are considered (England et al. 2021; Chylek et al. 2022; Rantanen et al. 2022). As examples, Chylek et al. (2022) and Rantanen et al. (2022) showed that land and ocean areas poleward of 60°N have warmed ~2–4 times faster than the global mean during the past several decades.

This section examines Arctic annual temperatures for northern land (60°N–90°N), ocean, and total area (land and ocean) temperatures. A summary of seasonal air temperature anomalies is also discussed with an emphasis on the large-scale patterns observed during 2022 (see Sidebar 5.1 for some temperature highlights).

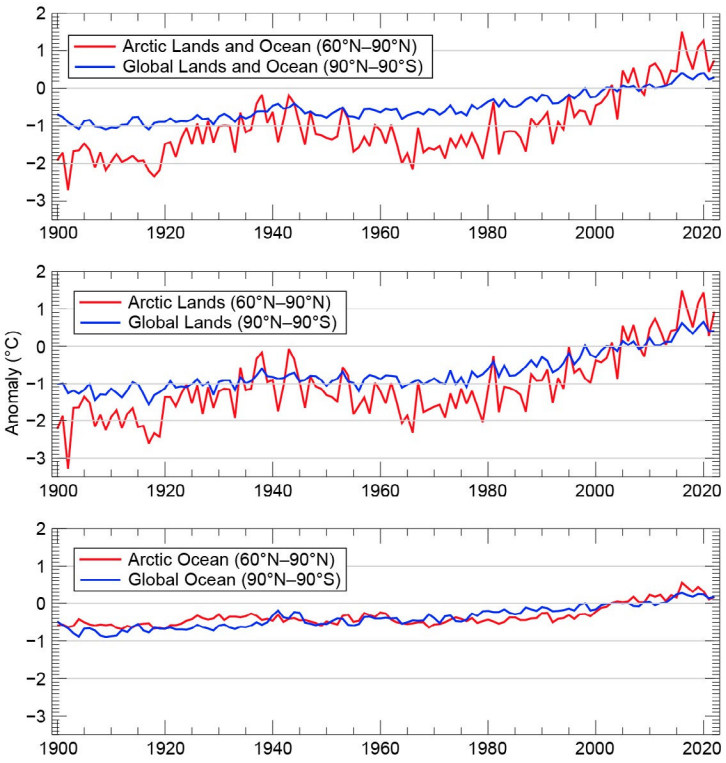

Fig. 5.1. Annual mean (Jan–Dec) Arctic (red lines) and global (blue lines) surface air temperature anomalies (°C) for (a) land and ocean areas, (b) land-only, and (c) ocean-only for 1900–2022. Spatial domains are listed in each panel. (Source: NASA GISTEMP v4.)

2. ARCTIC ANNUAL TEMPERATURES DURING 2022

The year 2022 was the fifth-warmest for land and ocean areas poleward of 60°N since 1900 (Fig. 5.1a), according to analysis of the NASA Goddard Institute for Space Studies Surface Temperature analysis version 4 (GISTEMPv4). As described in Lenssen et al. (2019), GISTEMPv4 is comprised of weather station data over land from the NOAA Global Historical Climatology Network version 4 and Extended Reconstructed Sea Surface Temperature version 5 over ocean areas without sea ice and that are not adjacent to land-based stations (see more detailed sea-surface temperature discussion in section 5d). The annual average surface air temperature for 2022 was 0.76°C higher than the 1991–2020 mean. This marks the 13th consecutive year when Arctic air temperatures were above average and the ninth consecutive year when Arctic temperature anomalies have exceeded global mean anomalies. Including 2022, the 15 warmest years observed in the Arctic have all occurred since 2005 (Fig. 5.1a).

Considered independently, Arctic lands (Fig. 5.1b) and the Arctic Ocean (Fig. 5.1c) each experienced notable annual warm anomalies during 2022. Land temperatures were 0.92°C above the 1991–2020 mean, the fifth highest on record, while the Arctic Ocean 2022 mean temperature anomaly (0.17°C) was the 11th highest, both since 1900. Over the last half century, increased temperatures are apparent in both environments, with greater year-to-year variability observed over land compared to the ocean due to water's greater thermal inertia and heat capacity.

3. SEASONAL PERSPECTIVES ON ARCTIC TEMPERATURES IN 2022

Arctic air temperature anomalies for 2022, compared to the 1991–2020 mean, are presented in Fig. 5.2 for each season defined as: winter (January–March, JFM), spring (April–June, AMJ), summer (July–September, JAS), and autumn (October–December, OND). These seasonal definitions are selected to coincide with annual cycles discussed in the other sections of this chapter, including the spring onset of snow and sea-ice melt on the Arctic Ocean and the Greenland Ice Sheet's period of peak ablation during summer. Data presented here are from the European Centre for Medium-Range Weather Forecasts Reanalysis version 5 (ERA5) reanalysis (Hersbach et al. 2020).

A Eurasian–North American temperature dipole was present during winter (Fig. 5.2a). This was characterized by above-normal air temperatures in the Eurasian Arctic and cold departures over the North American high latitudes, associated with prevailing positive Arctic Oscillation/North Atlantic Oscillation conditions during much of winter. A large region of ≥3°C positive anomalies was concentrated over the central Arctic extending south to western Siberia and stretching across northern Eurasia. This region of above-average temperatures was associated with southerly flow off the Eurasian continent from a large, below-normal sea-level pressure (SLP) pattern (≤–5 hPa) over the Barents and Kara Seas combined with broad, above-normal SLP spanning central Siberia into the North American Arctic (Fig. 5.3a). Contrasting winter cold temperature anomalies (≤–2°C) were noted across high-latitude North America, extending from northeastern Alaska southeastward over Hudson Bay and Labrador Sea to the east (Fig. 5.2a). These below-normal air temperatures were driven by a low-pressure anomaly north of Hudson Bay (≤–5 hPa) and the aforementioned upstream high-pressure anomaly pattern (Fig. 5.3a).

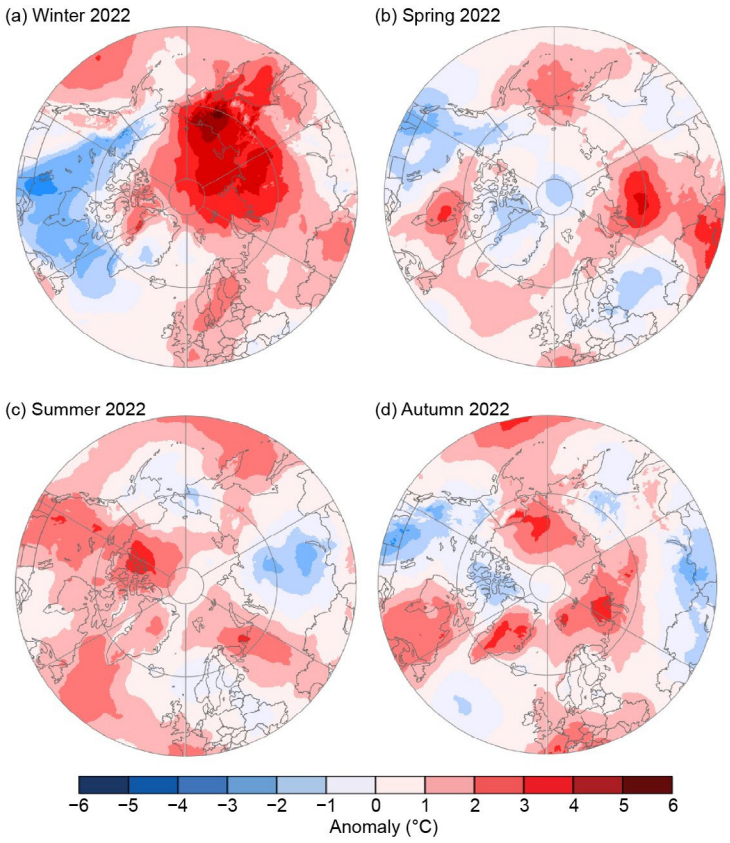

Fig. 5.2. Near-surface (925-hPa) air temperature anomaly maps (°C) for each season during 2022: (a) winter (Jan–Mar), (b) spring (Apr–Jun), (c) summer (Jul–Sep), and (d) autumn (Oct–Dec). Temperature anomalies are shown relative to the 1991–2020 means. (Source: ERA5 reanalysis.)

Spring air temperatures over the Arctic Ocean were near average, with relatively small air temperature anomalies over Arctic lands (Fig. 5.2b). This seasonal pattern was characterized by positive anomalies (≥+1°C) in central and eastern Siberia and atop Hudson Bay. A small area of the highest Arctic air temperature anomalies (+4°C to +5°C) was found just east of the Ural Mountains associated with low pressure anomalies (≤–3 hPa) that transported warm air into the area (Fig. 5.3b). Record-high June-averaged air temperatures were found over Svalbard (5°C–6°C; Mamen et al. 2022), though seasonal temperatures over the island were 2°C–3°C above normal. Meanwhile, near-normal air temperatures were found over the Arctic Ocean. Negative temperature anomalies (≤–1°C) were dispersed over northwestern North America, northwestern Greenland and adjacent Ellesmere Island, and westernmost Eurasia.

Summer air temperatures were above normal across much of the Arctic. Eastern Europe and eastern Siberia, and the Beaufort Sea and Canadian Archipelago saw positive anomalies ≥+1°C (Fig. 5.2c). Low pressure anomalies, suggestive of an active storm track, across Arctic Alaska and

northern Canada, supported the above-normal air temperatures in the latter areas (Fig. 5.3c). Below-normal temperatures were observed in central Eurasia and were associated with low pressure anomalies to the east that caused cold, northerly winds (Fig. 5.3c).

Autumn temperatures were characterized by above-normal temperatures in the Arctic marginal seas, with the largest temperature departures (≥+3°C) over Novaya Zemlya, Svalbard, the interior of the Greenland Ice Sheet, and the northern Chukchi Sea (Fig. 5.2d). Central Arctic Ocean air temperatures were near normal, but below-normal temperatures (≤–1°C) were found over the Canadian Archipelago. Higher-than-normal SLP and southerly flow were linked with the warm air temperature patterns (Fig. 5.3d). Notably, the southerly winds associated with the northern Chukchi Sea warm anomaly were a product of two strong pressure centers, with a positive pressure anomaly centered over mainland Alaska and the Gulf of Alaska (≥+5 hPa) coupled with a negative pressure anomaly over the East Siberian Sea (≤–5 hPa).

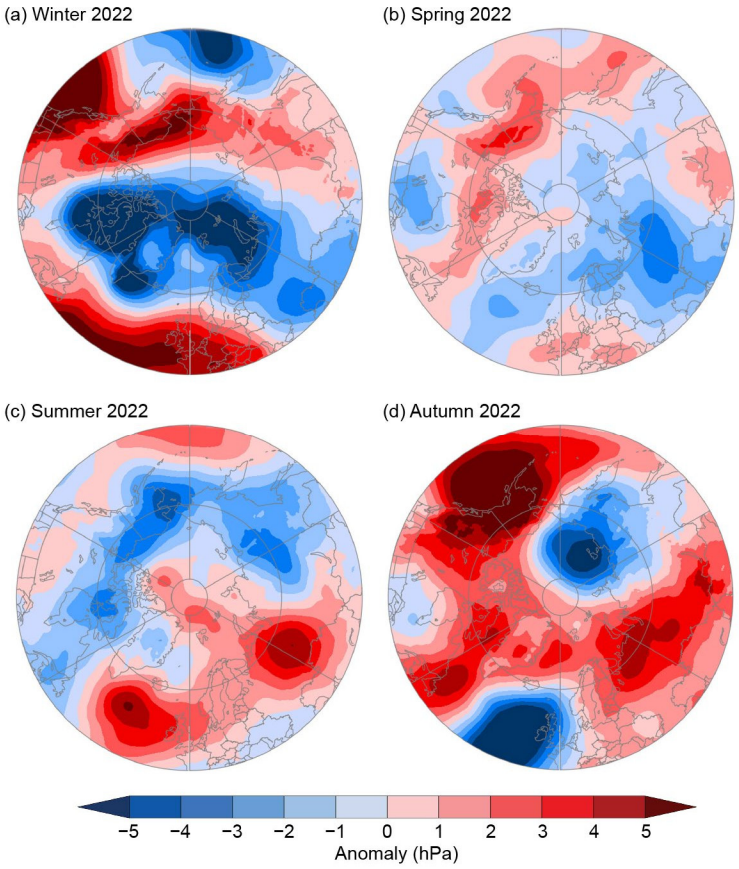

Fig. 5.3. Sea-level pressure (hPa) anomaly maps for each season during 2022: (a) winter (Jan–Mar), (b) spring (Apr–Jun), (c) summer (Jul–Sep), and (d) autumn (Oct–Dec). Anomalies are shown relative to the 1991–2020 means. (Source: ERA5 reanalysis.)

c. Precipitation

—J. E. Walsh, S. Bigalke, S. A. McAfee, R. Lader, M. C. Serreze, and T. J. Ballinger

1. OVERVIEW

Globally, precipitation over land has likely increased since 1950, consistent with increases in total atmospheric moisture (IPCC 2021). However, previous assessments of observed Arctic precipitation have not shown coherent trends (Walsh et al. 2020); results depend on the time period, region, and data product. Climate models project increased Arctic precipitation and more frequent heavy precipitation (e.g., Sillmann et al. 2013; Kusunoki et al. 2015; McCrystall et al. 2021).

Gauge measurements of precipitation are especially problematic in the Arctic, because the sparse gauge network does not provide representative measurements in many northern regions. Moreover, precipitation gauges suffer from undercatch in cold, windy conditions (Ye et al. 2021). For this reason, gridded reanalyses are increasingly used to assess Arctic precipitation. For example, Yu and Zhong (2021) and White et al. (2021) used the European Centre for Medium-Range Weather Forecasts Reanalysis-Interim (ERA-Interim) and ERA version 5 (ERA5) reanalyses, respectively, to show that Arctic precipitation trends vary regionally and seasonally over the past few decades. In this section, we use the newer and highly regarded ERA5 reanalysis (Hersbach et al. 2020) to provide an overview of 2022 Arctic precipitation anomalies in the context of recent and ongoing changes. Reanalyses have weaknesses related to changes in input data, notably the inclusion of satellite data beginning in 1979, thus we also use gridded station data from the Global Precipitation Climatology Centre's GPCC V.2022 (Becker et al. 2013; Schneider et al. 2022).

2. ARCTIC PRECIPITATION IN 2022

Arctic precipitation in 2022 was characterized by wetter-than-normal conditions in many areas, with record-breaking heavy precipitation events at various locations. Overall, 2022 pan-Arctic (north of 60°N) precipitation was the third highest since 1950, trailing only 2020 and 2017, according to ERA5 reanalysis. Winter (January–March), summer (July–September), and autumn (October–December) were all among the 10 wettest for their respective seasons.

In winter 2022, there were positive precipitation anomalies in the North Atlantic subarctic, the Gulf of Alaska, and much of southern Alaska (Fig. 5.4). The wet anomalies over Alaska link to anomalously high pressure over western Canada and low-pressure anomalies offshore (see Fig. 5.3a). The positive precipitation departures from Greenland to Norway are typical of those during La Niña conditions (NOAA 2022), which prevailed during 2022. Sea-level pressures were more than 5 hPa below average from northeastern Canada to northern Europe (Fig. 5.3a), indicative of an active cyclone pattern in the Atlantic. A mid-January storm set 32 local heavy-precipitation records in Norway and contributed to the positive seasonal departures there.

Spring is normally dry in the Arctic, and April–June (AMJ) 2022 was characterized by generally small departures from relatively low seasonal means. The atmospheric circulation anomalies were relatively weak (see Fig. 5.3b). For the 60°N–90°N region as a whole, AMJ precipitation was close to the 1950–2022 median. Negative precipitation anomalies across the North American subarctic (Fig. 5.4b) coincided with positive sea-level pressure anomalies (see Fig. 5.2b). In central and southern Alaska, where all three months had well-below-normal precipitation, drought developed during May over southwestern Alaska and northern Cook Inlet and expanded into Interior Alaska in June, setting the stage for severe wildfires in early summer (Alaska Division of Forestry 2022).

Overall, summer 2022 was the Arctic's third-wettest summer since 1950, but some areas were dry (Fig. 5.4c). Southeastern and southern Alaska were exceptionally wet, with some locations reporting their wettest summer on record. Western Alaska experienced heavy rain and coastal flooding from ex-Typhoon Merbok in September. New monthly records for July rainfall were set at various locations in northern Norway. However, dry conditions prevailed over parts of northern Canada and northeastern Europe, which contributed to low water levels in eastern European rivers (section 5h).

Autumn in the Arctic was the ninth wettest since 1950. Precipitation departures were generally positive in the Pacific subarctic, but mixed in the North Atlantic. In contrast to winter and summer, negative anomalies extended from the Labrador Sea northeastward across Iceland and into the Nordic seas, consistent with positive sea-level pressure anomalies in the region (see Fig. 5.3d). However, parts of northern Greenland were wetter than normal,

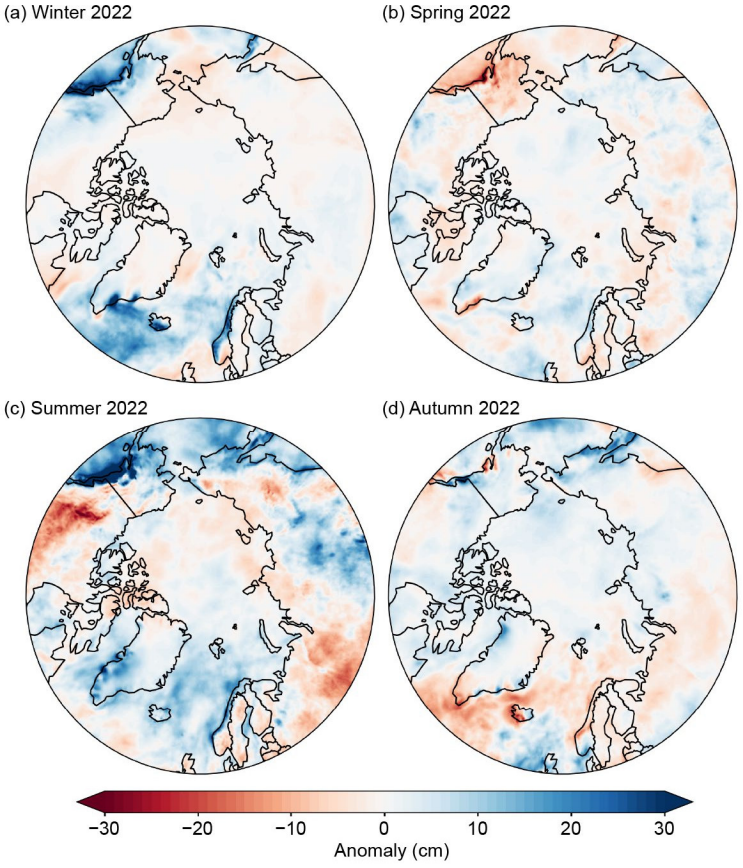

Fig. 5.4. Seasonal departures of 2022 precipitation (cm) from the 1991–2020 climatological means for the Arctic seasons: (a) winter (Jan–Mar), (b) spring (Apr–Jun), (c) summer (Jul–Sep), and (d) autumn (Oct–Dec). Blue shades denote above-normal precipitation; red shades denote below-normal precipitation. (Source: ERA5 reanalysis.)

especially in December. The southeastern Alaska Panhandle was also anomalously wet in autumn. Although south-central Alaska was seasonally dry (Fig. 5.4d), December was anomalously wet. These kinds of spatial and intraseasonal variability are not always well represented in seasonal average, relatively coarse data, such as ERA5.

3. HISTORICAL TRENDS

While there is considerable interannual variability in Arctic-wide average precipitation from 1950 to 2022, it is generally consistent across ERA5 and Global Precipitation Climatology Center (GPCC; Fig. 5.5). Both the reanalysis and gridded data show increases of about 10% in yearly total precipitation over this period, with more substantial increases in winter than summer. The consistency across seasons and datasets indicates that Arctic-wide precipitation is increasing, as expected from climate model simulations. For the more recent period 1979–2022, when ERA5 satellite data assimilation increased, trends in ERA5 (and also GPCC) precipitation are larger and remain statistically significant ($p < 0.05$) for the full year and for all seasons except AMJ. Spring trends for 1979–2022 are weaker than for 1950–2022 and insignificant in both datasets.

While the ERA5 product indicates scattered areas of decreasing precipitation in every season, areas of increase dominate (Fig. 5.6). Consistent with the area-averaged trends in Fig. 5.5, nearly

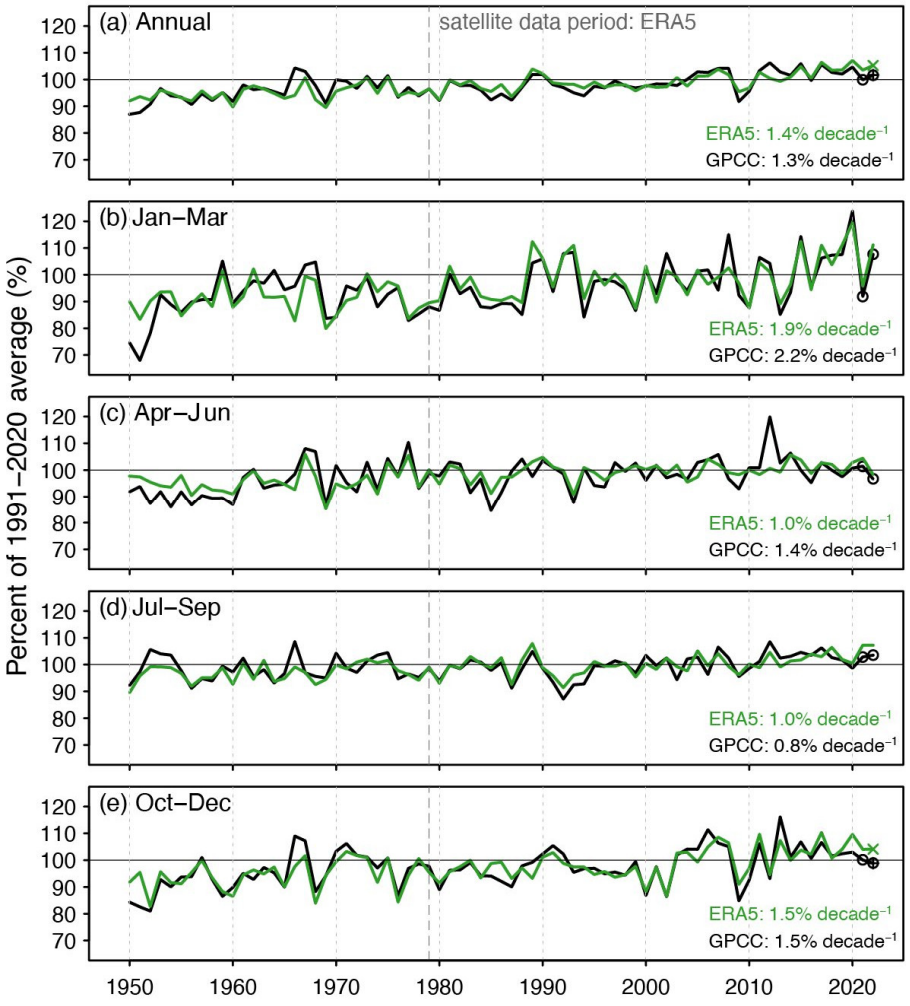

Fig. 5.5. Time series of Arctic (60°N–90°N) precipitation, expressed as percent departures from the corresponding 1991–2020 averages (%), for (a) the calendar years 1950–2022 and for each three-month Arctic season: (b) winter (Jan–Mar), (c) spring (Apr–Jun), (d) summer (Jul–Sep), and (e) autumn (Oct–Dec). Results are from ERA5 (green lines; "×" denotes value based in part on the ERA5 preliminary product for December 2022) and GPCC 1.0° data (black lines; "o" and "+" denote values based on GPCC monitoring and first-guess products, respectively). GPCC values are for land only, and ERA5 values are for land and ocean. Linear trends and are shown in lower right of each panel. All trends are significant at p <0.001.

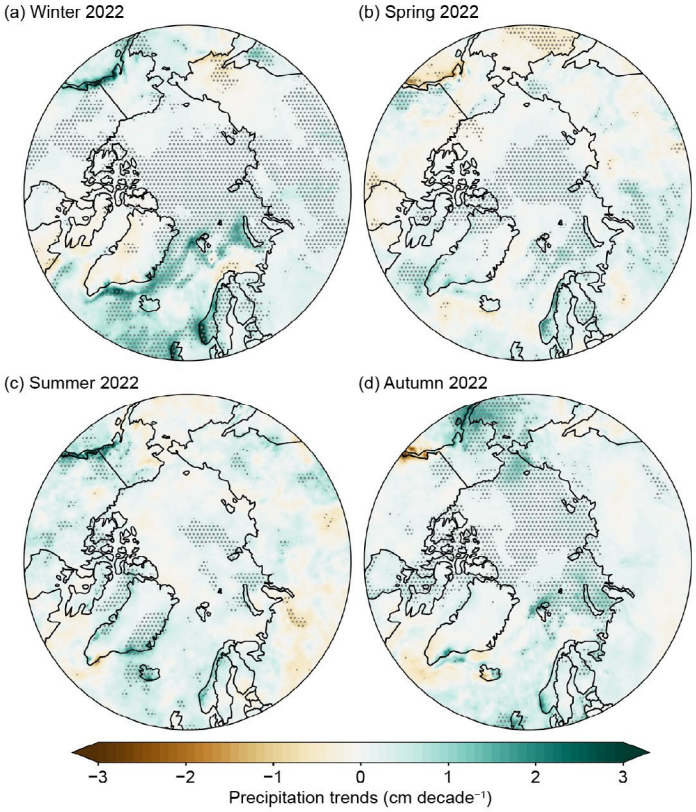

Fig. 5.6. Precipitation trends (cm decade^{-1}) over the period 1950–2022 for the Arctic seasons: (a) winter (Jan–Mar), (b) spring (Apr–Jun), (c) summer (Jul–Sep), and (d) autumn (Oct–Dec). Green shades denote trend increases and brown shades denote trend decreases. Stippling denotes trend significance at the 0.05 level. (Source: ERA5.)

all areas of statistically significant change are increases. Increased precipitation is especially pronounced in the subpolar Pacific south of Alaska during autumn, winter, and summer, and the subpolar North Atlantic during winter. The southwestern coast of Norway is dominated by increases in all seasons. Negative precipitation trends are most prominent in the subarctic during spring and summer.

4. INDICATORS OF PRECIPITATION EXTREMES

According to ERA5, heavy precipitation—defined here as yearly maximum one-day (Rx1) and five-day (Rx5) precipitation—shows no coherent trends over most of the Arctic. Large and significant increases in Rx1 and Rx5 as well as the annual maximum number of consecutive wet days (CWD) are apparent in the Atlantic sector, including northeastern Greenland (Fig. 5.7), indicating that heavy precipitation events contribute to the overall precipitation increase in these areas (Fig. 5.6). The CWD trend is positive from Svalbard eastward to the Chukchi Sea. Areas with increases in CWD generally coincide with areas of reduced sea-ice coverage. The annual maximum number of consecutive dry days (CDD) has decreased, especially in the European sector of the Arctic Ocean, the Canadian Archipelago, and north-central Asia. In moisture-limited areas such as the boreal forest during summer, these changes imply reduced vulnerability to drought stress and an increased potential for plant growth, although evapotranspiration also increases in a warming climate.

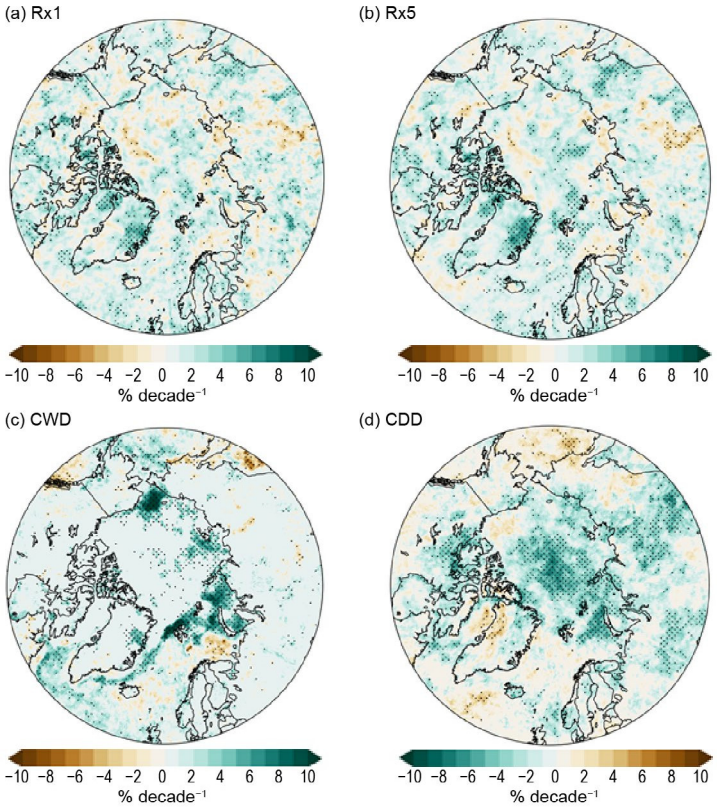

Fig. 5.7. Trends of daily extreme precipitation indices (% decade^{-1}) over the period 1950–2021. Plots are shown for yearly maximum one-day total precipitation (Rx1; upper left), yearly maximum five-day amount (Rx5; upper right), yearly maximum number of consecutive wet days (CWD; lower left), and yearly maximum number of consecutive dry days (CDD; lower right). Green shades denote trends toward wetter extremes; brown shades denote trends towards drier extremes. Stippling denotes trend significance at the 0.05 level. (Source: ERA5.)

Sidebar 5.1: Extreme weather and climate events in 2022

—R. BENESTAD, R. L. THOMAN, JR., J. L. COHEN, J. OVERLAND, E. HANNA, G. W. K. MOORE, M. RANTANEN, G. N. PETERSEN, AND M. WEBSTER

Arctic extreme events occur when natural weather variability interacts with the long-term climatic state, and vary by type, location, and season. They are also affected by long-term human-caused warming trends and arise from interactions between multiple anomalies in the atmosphere, ocean, and land, and can affect ecosystems and communities. These fluctuations, beyond typical variability, often have detrimental impacts. Global warming provides an ongoing thermodynamic response through Arctic amplification, which leads to temperature increases (see section 5b), permafrost thaw (see section 5i), and sea-ice loss/open water (see section 5e). These factors combine with the natural range of atmospheric and oceanic dynamics, e.g., jet-stream meanders, atmospheric blocking, weather patterns, storms, and upper ocean heat content (Overland 2022), to create extreme events. Thermodynamic responses to amplified Arctic warming provide precursors to major impacts. New extremes do not require much deviation from past ranges of atmospheric circulation patterns; hence, extreme events can occur in many locations with many different impacts. Weather and climate extremes influence ecosystems based on species-specific life histories (see section 5j), such as the timing of reproduction and migration (see Sidebar 5.2). Societal impacts on livelihoods follow from, for example, changes in sea ice, land cover, and ecosystems.

In a statistical sense, extremes are conditions that are infrequent and approach or exceed the limits of observed states. Record-breaking events are clear examples; however, previously unobserved events may also be extreme events (in 2022 for example, rain on Greenland and tongues of open water to the north of Novaya Zemlya and Franz Josef Land). We may consider extremes by their character in an objective scientific context, and through their effect on nature and society. Some events that may be characterized as "far out in the tail" may not necessarily have a strong impact on the environment, whereas others that are less spectacular in terms of statistical aspects may have catastrophic consequences for people, plants, or animals. The occurrence and nature of extreme weather and climate events reflect the state of Earth's climate. Hence, the number, type, and intensity of extreme events in the Arctic are expected to change with the ongoing global warming, and be exacerbated by Arctic amplification.

Extreme weather and climate events vary in time scales, ranging from short-lived storms to long-lasting droughts. In the Arctic, such rare and forceful meteorological phenomena include cyclones, avalanches, droughts, heatwaves, wildfires, and floods. Cyclones are associated with strong winds, heavy precipitation, and waves over open sea, but extreme winds are also caused by weather fronts, atmospheric convection, polar lows, and atmospheric rivers. Extreme precipitation involves both brief, intense rainfall and high accumulation over long wet spells. Droughts are also extreme events, caused by a lack of precipitation over longer periods. There are also compound extremes, such as rain-on-snow and freezing rain. Rain-on-snow may result in extreme transformations in the snow cover such as formations of ice layers. Extreme temperatures can be very cold or very hot, and both are typically due to long-lasting atmospheric blocking high pressure anomalies. Hot, dry conditions increase the risk of wildfires. Abrupt and extreme shifts or variations in conditions also create extreme events, such as the extreme warmth exceeding +8°C over central Greenland during 1–6 September 2022, which brought late-season melting over vast areas: the most on record in September (see section 5f). Other examples of abrupt changes include wildfires, which result in lasting transformation of the landscape and ecosystems.

Figure SB5.1 shows that 2022 was an extremely warm year over extensive regions of the Arctic. Much of the Eurasian Arctic was the second warmest since 1950 (see section 5b). The 2022 summer also brought the most extensive wildfire season on record to southwest Alaska, where wildfire is historically

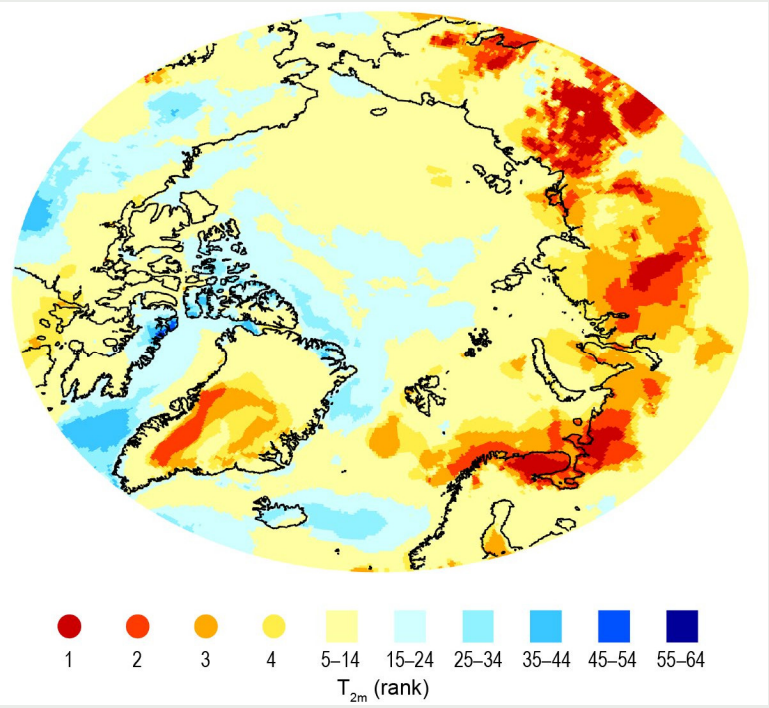

Fig. SB5.1. The historical temperature ranking (T_{2m}) of the 2022 mean air temperature compared to the 1950–2022 period. Note how many regions experienced air temperature rankings among the five highest temperatures on record, with extremely warm regions in the Barents Sea, central Greenland, and parts of Siberia.

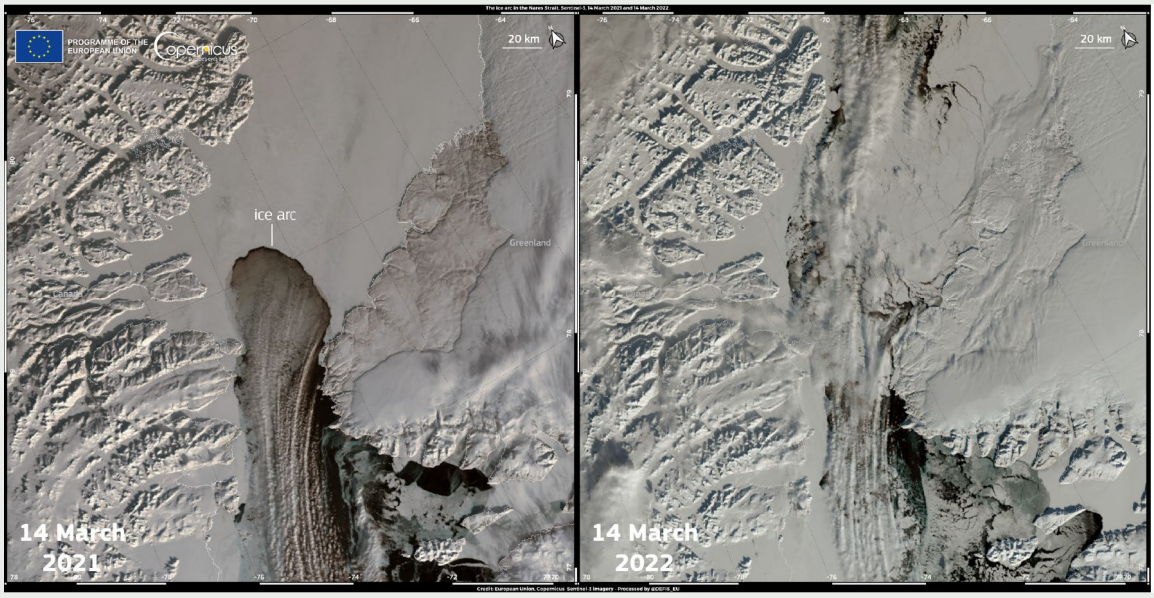

Fig. SB5.2. An ice arch in the Nares Strait between Canada and Greenland which typically appears in the winter such as in 2021 (left) but was absent in 2022 (right). Credit: European Union, Copernicus Sentinel-3 imagery. (Source: https://www.copernicus.eu/en/media/image-day-gallery/absence-ice-arch-nares-strait-2022-winter.)

rare. This was due to a warm, dry spring and an early snowpack melt-out. Heatwaves were observed in both the Barents and Beaufort Seas in 2022. Svalbard had a record-warm June, and November was the warmest on record for Iceland and the third warmest in Reykjavík, followed by the coldest December in Iceland since 1973. Early December brought extreme warmth to northwest Alaska, and some Bering Strait communities experienced a complete loss of snowpack due to rain and sustained above-freezing temperatures. On 5 December, the temperature at Utqiaġvik rose to 4.4°C, which was the highest winter temperature on record. No curve-shaped sea-ice edge spanning across the Nares Strait (known as "sea ice arches"; Fig. SB5.2) formed during 2022, only the third time since the early 1980s that such an arch has not formed. Thinning Arctic sea ice is a likely reason for the absent sea-ice arch (Moore et al. 2021).

Figure SB5.3 presents a summary of different categories of Arctic extremes reported for 2022. Of these, extremely high rainfall and temperatures accounted for most of the extreme Arctic events. Trends in extreme daily precipitation amounts (see section 5c) may be explained by increases in the number of days with precipitation (a dynamic effect) or increases in the mean precipitation intensity (a thermodynamic effect). It is also possible that daily precipitation has become more concentrated into smaller and more intense wet spots over Earth's surface over the recent decades (Benestad et al. 2022).

Extreme storms can cause extensive societal impact. One of the most impactful Arctic extreme events in 2022 was a historically powerful storm that struck western Alaska in September. The storm originated as Typhoon Merbok in the subtropical North Pacific and transitioned to a very strong extratropical cyclone just prior to reaching the Bering Sea, where the storm had the lowest pressure (932 hPa) of any storm to form that early in the autumn since at least 1950. Ex-Typhoon Merbok caused severe coastal flooding across western Alaska, with extensive infrastructure damage along a 1600-km stretch of coast from Kuskokwim Bay to the Bering Strait. Some communities experienced their highest water levels in at least the last 100 years. Another Arctic cyclone east of Svalbard, with record-low mean sea-level pressure (932 hPa) on 24 January, caused an unprecedented reduction in sea ice (Blanchard-Wrigglesworth et al. 2022). An extreme wind storm hit Iceland at the end of September with recorded wind speeds of up to 64 m s^{-1}. Due to the active North Atlantic storm track in February, extreme snowfall occurred in Reykjavik, Iceland,

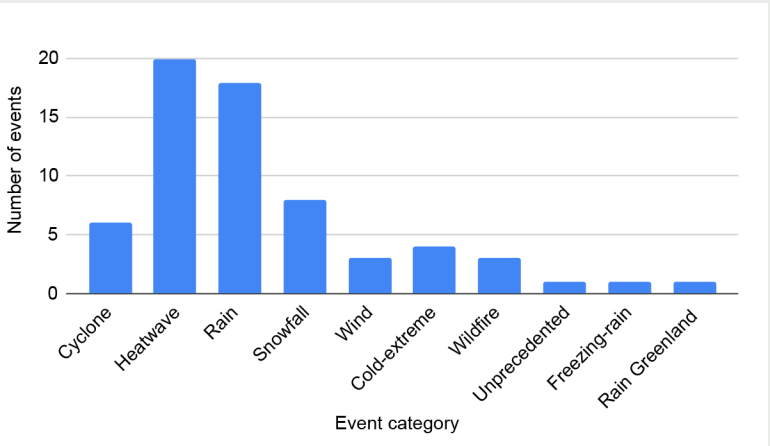

Fig. SB5.3. A summary of reported extreme event categories in the arctic in 2022. Cyclones and wind events may overlap. The total number of recorded events for 2022 was 56, and the summary is based on collected events from meteorological services connected to the Arctic, except from Russia. (Sources: National meteorological services associated with the Arctic.)

and a new national monthly rainfall record (142.7 mm) was set in Finland and Norway (see section 5c). In contrast, March was record dry in many places in Fennoscandia.

Changes in the Arctic may also contribute to extreme weather at lower latitudes, although there is not a scientific consensus on this issue (Cohen et al. 2020). North Pacific Arctic warming is a precursor to a polar vortex that stretches, resulting in Arctic cold surface air outbreaks across North America (Cohen et al. 2021). Following the record Alaskan warmth in early December 2022, the stretched polar vortex unleashed extreme cold and blizzards across Canada and the U.S. lower 48 states during 21–26 December, making it one of the costliest and deadliest U.S. weather disasters in 2022 (https://www.ncei.noaa.gov/access/billions/).

d. Sea-surface temperature

—M.-L. Timmermans and Z. Labe

Arctic Ocean sea-surface temperatures (SSTs) in the summer are driven by the amount of incoming solar radiation absorbed by the sea surface and by the flow of warm waters into the Arctic from the North Atlantic and North Pacific Oceans. Solar warming of the Arctic Ocean surface is influenced by the distribution of sea ice (with greater warming occurring in ice-free regions), cloud cover, and upper-ocean stratification. Discharge of relatively warm Arctic river waters can provide an additional source of heat in the coastal regions.

Arctic SST is an essential indicator of the role of the ice–albedo feedback cycle in any given summer sea-ice melt season. As the area of sea-ice cover decreases, more incoming solar radiation is absorbed by the darker ocean surface and, in turn, the warmer ocean melts more sea ice. Marine ecosystems are also influenced by SSTs, which affect the timing and development of production cycles, as well as available habitat. In addition, higher SSTs are associated with delayed autumn freeze-up and increased ocean heat storage throughout the year. An essential point for consideration, however, is that the total heat content contained in the ocean surface layer (i.e., the mixed layer) depends on its depth; a shallower mixed layer with higher SSTs could contain the same amount of heat as a deeper mixed layer with lower SSTs. We focus only on SSTs here and do not quantify ocean heat content due to a lack of in situ observations.

The SST data presented here are from the NOAA Optimum Interpolation (OI) SST version 2 product (OISSTv2; Reynolds et al. 2002, 2007) from 1982 to 2022, with comparisons made to the 1991–2020 baseline period. In the Arctic Ocean overall, the OISSTv2 product exhibits a cold bias (i.e., underestimates SST) of up to 0.5°C compared to ship-based measurements (Stroh et al. 2015). The OISSTv2 product uses a simplified linear relationship with sea-ice concentration to infer SST under sea ice (Reynolds et al. 2007), which means SSTs may be too cool by up to 0.2°C where there is sea-ice cover. There is an updated product (version 2.1) that employs a different method than OISSTv2 for setting a proxy SST in sea-ice-covered regions, applied only after January 2016 (in addition to some other differences that are not specific to the polar regions). See Huang et al. (2021) for a description. In our examination of trends in the Arctic Ocean, we require a product that estimates SST in the presence of sea ice using a consistent method for the duration of the data record. Otherwise, estimated trends might be artifacts of the change in methodology part way through the record. For this reason, we continue to use OISSTv2.

We focus primarily on August mean SSTs, which provide the most appropriate representation of Arctic Ocean summer SSTs. It is not appropriate to evaluate long-term SST trends in early summer (June and July) when most of the Arctic marginal seas still have significant sea-ice cover. SSTs generally plateau in the month of August, while surface cooling takes place in the latter half of September. This is evident, for example, in the fact that the mean of each year's standard deviation of weekly SST time series over 1991–2020 for the Arctic Ocean (north of 65°N) gives 0.1°C in August and 0.3°C in September (with even higher variance in September when individual marginal seas of the Arctic basin are considered separately).

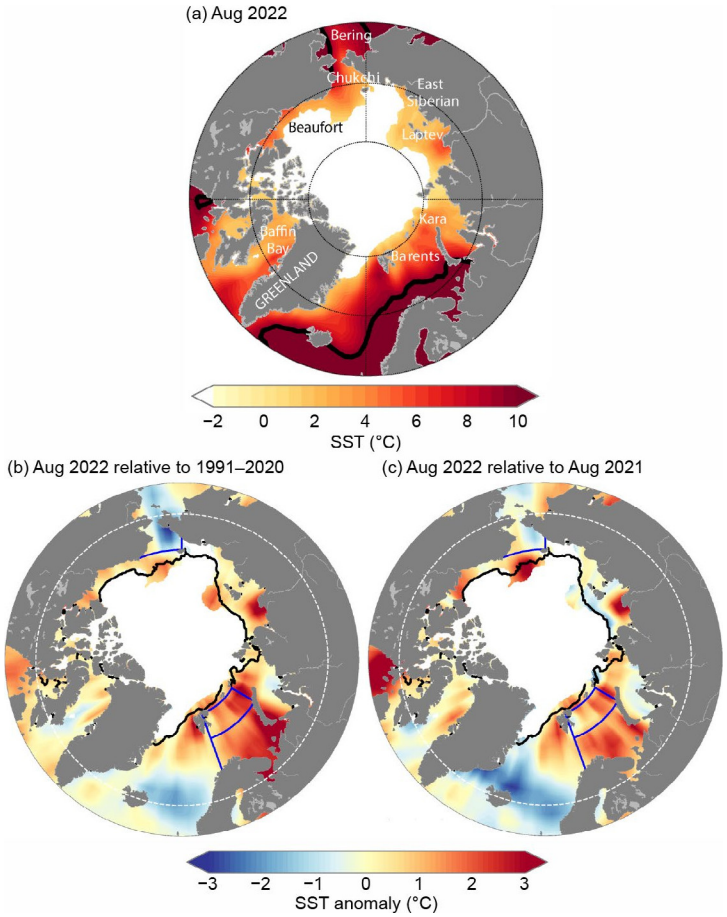

August 2022 mean SSTs were as high as ~12°C in the southern Barents Sea and as high as ~6°C in other marginal regions of the Arctic basin (northern Barents, Chukchi, Beaufort, East Siberian, Kara, and Laptev Seas; Fig. 5.8a). August 2022 mean SSTs were notably warm (~2°C–3°C higher than the 1991–2020 August mean) in the Barents and Laptev Seas and cool in the Chukchi Sea (~3°C lower than the 1991–2020 mean; Fig. 5.8b). In assessing these regional differences, it is important to note that SSTs exhibit significant variability from year to year. For example, there were considerably higher SSTs in the Barents Sea and lower SSTs in the waters off eastern Greenland in August 2022 compared to August 2021, with differences of up to 3°C in each case (Fig. 5.8c; see also Timmermans and Labe 2022). The August 2022 anomalously high SSTs in the Barents Sea, which were also observed in June and July (Fig. 5.9), aligned with anomalously high June–August 2022 surface air temperatures over northern Eurasia (section 5b).

Fig. 5.8. (a) Mean sea-surface temperature (SST; °C) in Aug 2022. Black contours indicate the 10°C SST isotherm. (b) SST anomalies (°C) in Aug 2022 relative to the Aug 1991–2020 mean. (c) Difference between Aug 2022 SSTs and Aug 2021 SSTs (negative values indicate where 2022 SSTs were lower). White shading in all panels is the Aug 2022 mean sea-ice extent. Black lines in (b) and (c) indicate the median ice edge for Aug 1991–2020. The regions marked by blue boundaries and the white dashed lines indicating 65°N in (b) and (c) relate to data presented in Fig. 5.10. Sea-ice concentration data are the NOAA/NSIDC Climate Data Record of Passive Microwave Sea Ice Concentration, version 4 (https://nsidc.org/data/g02202) and Near-Real-Time NOAA/NSIDC Climate Data Record of Passive Microwave Sea Ice Concentration, version 2 (https://nsidc.org/data/g10016; Peng et al. 2013; Meier et al. 2021a,b), where a threshold of 15% concentration is used to calculate sea-ice extent.

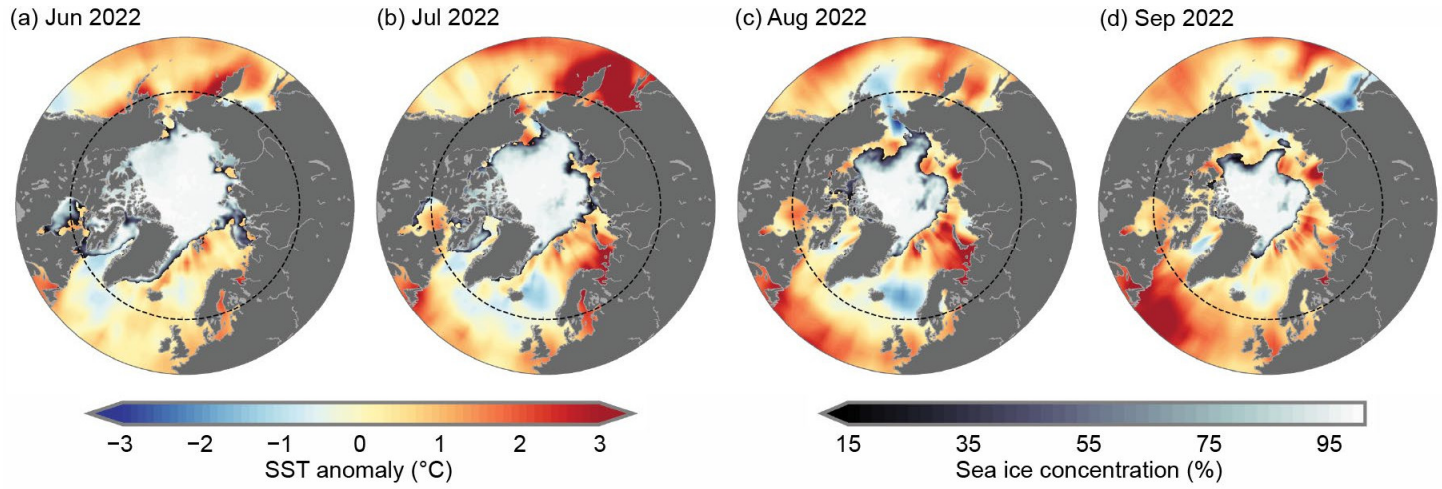

Fig. 5.9. Sea-surface temperature (SST) anomalies (°C) for (a) Jun 2022, (b) Jul 2022, (c) Aug 2022, and (d) Sep 2022 relative to the 1991–2020 mean for the respective month. The sea-ice concentration for the corresponding month is also shown. The evolution of sea-ice concentration over the months of Jun to Aug illustrates why it is not appropriate to evaluate long-term SST trends in Jun and Jul over most of the Arctic marginal seas, which still have significant sea-ice cover in those months. While sea-ice extent is lowest in Sep, SSTs cool in the latter part of the month (see text). The black dashed circle indicates the latitudinal bound of the map images shown in Figs. 5.8 and 5.10. See Fig. 5.8 caption for sea-ice dataset information.

The August 2022 anomalously cool SSTs in the Chukchi Sea are commensurate with below-normal surface air temperatures in the region in June–August 2022 (section 5b). The persistence of a tongue of late-season sea ice near the coast where the East Siberian Sea meets the Chukchi Sea is further consistent with these anomalously low SSTs (Fig. 5.8b; section 5e). Conversely, to the north of this region of cool SSTs, sea-ice area was below normal and SSTs were anomalously high (Fig. 5.8b).

Mean August SST warming trends from 1982 to 2022 persist over much of the Arctic Ocean, with statistically significant (at the 95% confidence interval) linear warming trends in most regions, except the Laptev, East Siberian, and northern Barents Seas (Fig. 5.10a). Mean August SSTs for the entire Arctic (the Arctic Ocean and marginal seas north of 65°N) exhibit a linear warming trend of +0.03±0.01°C yr^{-1} (Fig. 5.10b). Even while anomalously low SSTs in the Chukchi Sea were prominent in the August 2022 SST field (Fig. 5.8b), SSTs show a linear warming trend over 1982–2022 of +0.05±0.03°C yr^{-1} (Fig. 5.10c) for this region. The cooling trend in mean August SSTs in the northern Barents Sea (Fig. 5.10d) remains an exception. This cooling trend has been notably influenced by anomalously high SSTs in that sector of the Barents Sea in the 1980s and 90s (Fig. 5.10d), although anomalously high SSTs in recent years in the region continue to have an influence on reversing the overall trend.

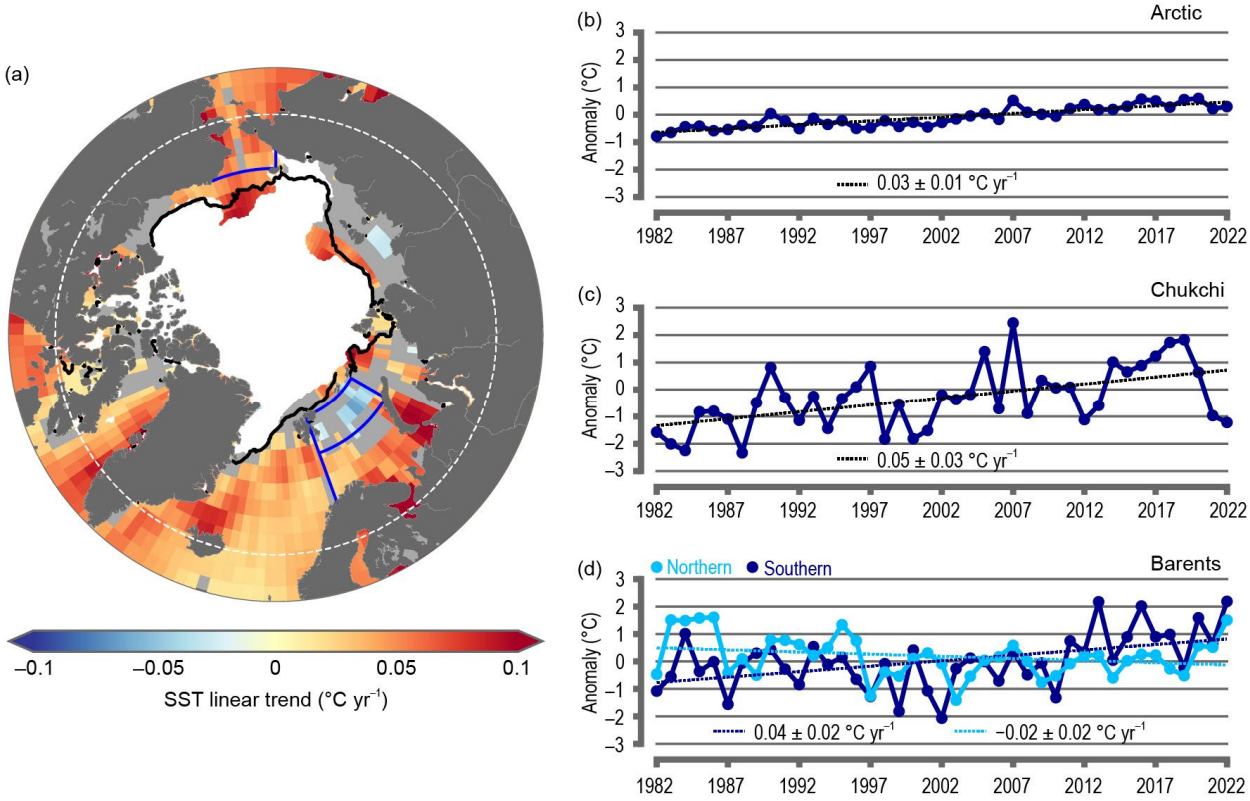

Fig. 5.10. (a) Linear sea-surface temperature (SST) trend (°C yr^{-1}) for Aug of each year from 1982 to 2022. The trend is only shown for values that are statistically significant at the 95% confidence interval; the region is shaded gray otherwise. White shading is the Aug 2022 mean sea-ice extent, and the black line indicates the median ice edge for Aug 1991–2020. (b),(c),(d) Area-averaged SST anomalies (°C) for Aug of each year (1982–2022) relative to the 1991–2020 Aug mean for (b) the entire Arctic Ocean north of 65°N, indicated by the dashed white circle in (a), (c) the Chukchi Sea, and (d) the northern and southern Barents Sea indicated by smaller blue boxes (intersecting with land boundaries) in (a). The dotted lines show the linear SST anomaly trends over the period shown and trends in °C yr^{-1} (with 95% confidence intervals) are indicated on the plots. See Fig. 5.8 caption for sea ice dataset information.

e. Sea ice

—W. N. Meier, A. Petty, S. Hendricks, D. Perovich, S. Farrell, M. Webster, D. Divine, S. Gerland, L. Kaleschke, R. Ricker, and X. Tian-Kunze

As the frozen interface between the ocean and atmosphere in the North, Arctic sea ice limits ocean–atmosphere exchanges of energy and moisture and plays a critical role in Arctic ecosystems and Earth's climate. The presence of sea ice affects human activities in the Arctic, including Indigenous hunting and transportation, marine navigation, and national security responsibilities. The profound changes underway in the region continued to be illuminated by Arctic sea-ice conditions during 2022.

1. SEA-ICE EXTENT

Arctic sea ice began 2022 with higher coverage than in January 2021. In January 2022, sea-ice extent (defined as the total area covered by at least 15% ice concentration) was within the inter-decile range of the 1991–2020 median extent, which has been rare in recent years. Extent values are from the National Snow and Ice Data Center's Sea Ice Index (Fetterer et al. 2017), one of several extent products (Lavergne et al. 2019; Ivanova et al. 2014) derived from satellite-borne passive microwave sensors operating since 1979. Persistently high sea-level pressure in the Siberian Arctic sector during January–February resulted in the divergence of ice from the Siberian coast as well as strong advection of thicker, multiyear ice into the Beaufort and Chukchi Seas from the north.

By March, the month with the greatest ice cover annually, the total sea-ice extent of 14.59×10^6 km^2 was 0.44×10^6 km^2 (5.1%) lower than the 1991–2020 average and the ninth-lowest March extent in the 44-year record. The March 2022 extent continued the statistically significant downward trend of –2.6% decade^{-1} over the 1979–2022 record (Fig. 5.11a). On a regional basis, March 2022 was characterized by below-average extent in the Barents Sea and the Sea of Okhotsk, above-average extent in the Baffin Bay and Davis Strait, and near-average extent elsewhere (Fig. 5.11b).

After March, the seasonal retreat of sea ice began. In contrast to recent years, ice lingered along the Siberian coast until late summer, particularly in the East Siberian and Chukchi Seas. Weak pressure gradients and somewhat lower temperatures (relative to recent years) slowed sea-ice melt. In contrast, open water regions developed in late July north of the Kara Sea, near 88°N latitude, and persisted for several weeks. The openings resulted from a thinner, less compact ice cover, which may have been subjected to melt from warm ocean water.

September, the month of the annual minimum extent, was characterized in 2022 by below-average coverage in the Pacific sector, with the exception of a tongue

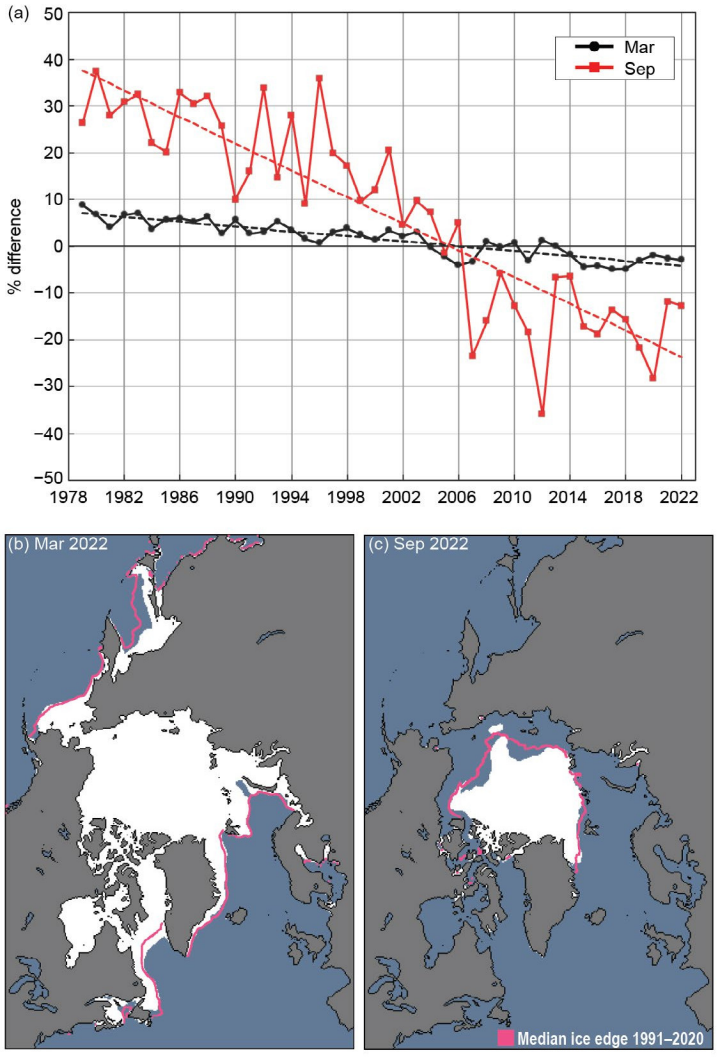

Fig. 5.11. (a) Monthly sea-ice extent anomalies (%, solid lines) and linear trend lines (dashed lines) for Mar (black) and Sep (red) from 1979 to 2022. The anomalies are relative to the 1991–2020 average for each month. (b) Mar 2022 and (c) Sep 2022 monthly average sea-ice extent; the median extent for 1991–2020 is shown by the magenta contour.

of ice in the East Siberian Sea that reached beyond the 1991–2020 median extent (Fig. 5.11c). The September 2022 Arctic sea-ice extent of 4.87×10^6 km^2 was 0.71×10^6 km^2 (12.7%) lower than the 1991–2020 average and the 11th-lowest September extent on record. The September trend from 1979 through 2022 is –14.2% decade^{-1}, and like all other months, is statistically significant. The 16 lowest September extents in the satellite record have all occurred in the last 16 years (2007–22), though the trend over that period has been near-zero.

2. SEA-ICE AGE, THICKNESS, AND VOLUME

Sea-ice age is a proxy for thickness as multiyear ice (ice that survives at least one summer melt season) grows thicker over successive winters. Sea-ice age is presented here (Fig. 5.12) for the period 1985–2022, based on Lagrangian tracking of ice parcels (Tschudi et al. 2019a,b). One week before the 2022 annual minimum extent, when the age values of the remaining sea ice are incremented by one year, the amount of multiyear ice remaining in the Arctic continued to be far lower than in the 1990s (Fig. 5.12). Since 2012, the Arctic has been nearly devoid of the oldest ice (>4 years old); this continued in 2022, with an end-of-summer oldest ice extent of 127,000 km^2. In the 38 years since ice-age records began, the Arctic has changed from a region dominated by multiyear sea ice to one where first-year sea ice prevails. A younger ice cover implies a thinner, less voluminous ice pack—one that is more sensitive to atmospheric and oceanic conditions.

Sea ice drifts with winds and ocean currents, while growing and melting thermodynamically. Ice divergence creates leads and, in freezing conditions, new ice, while ice convergence leads to dynamic thickening. Sea-ice thickness provides a record of the cumulative effect of dynamic and thermodynamic processes and thus is an important indicator of overall ice conditions. European Space Agency satellites carrying the CryoSat-2 radar altimeter and the Soil Moisture and Ocean

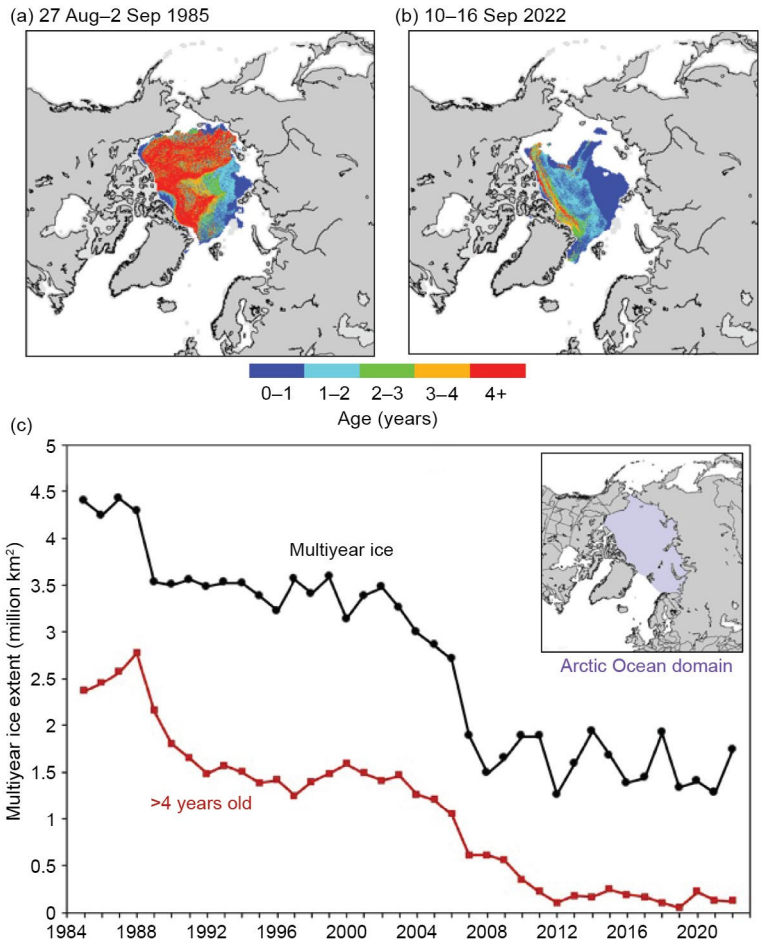

Fig. 5.12. Sea-ice age coverage map for the week before minimum total extent (when age values are incremented to one year older) in (a) 1985 and (b) 2022; (c) extent of multiyear ice (black) and ice >4 years old (red) within the Arctic Ocean (inset) for the week of the minimum total extent.

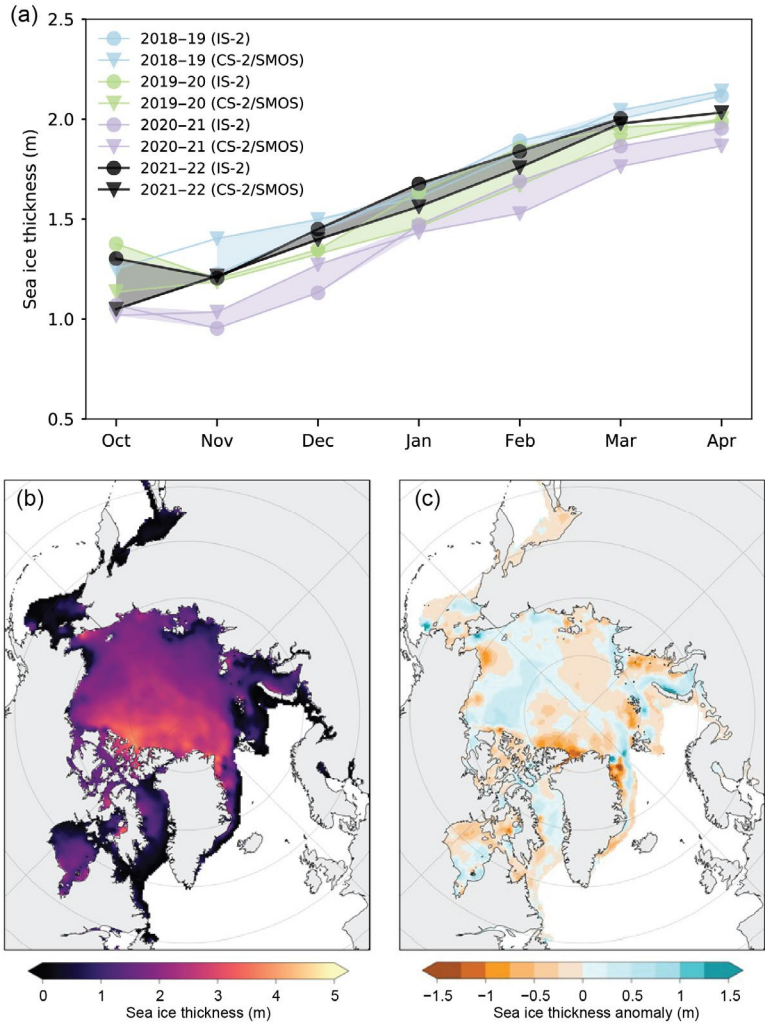

Fig. 5.13. (a) Oct–Apr monthly average sea-ice thickness, calculated over an inner-Arctic Ocean domain (inset of Fig. 5.12c), from ICESat-2 (circles) and CryoSat-2/SMOS (triangles) for 2018/19 (blue), 2019/20 (green), 2020/21 (lilac), and 2021/22 (black); (b) average Apr 2022 sea-ice thickness map from CryoSat-2/SMOS; (c) CryoSat-2/SMOS thickness anomaly map (relative to the 2010–21 average).

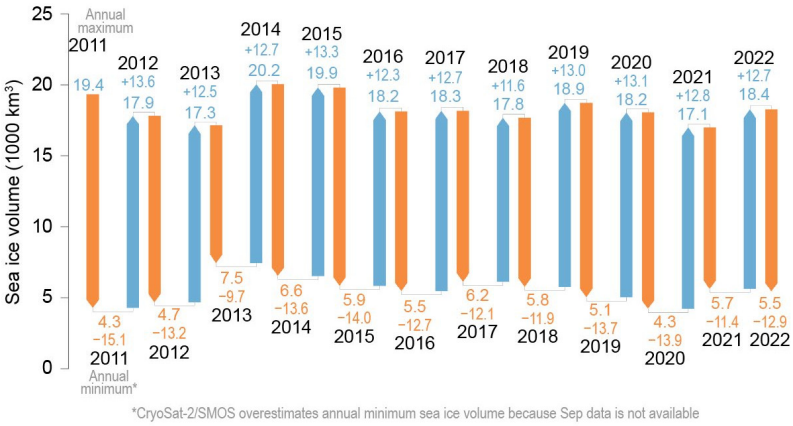

Fig. 5.14. Annual sea-ice volume loss (orange) and gain (blue) between annual maximum and minimum from the CryoSat-2/SMOS Sea Ice Thickness Version 205 product (https://earth.esa.int/eogateway/catalog/smos-cryosat-l4-sea-ice-thickness, accessed 5 Mar 2023). Volume is not estimated during summer, May–Sep. The volume gain represents the change in volume from the first autumn observation in Oct to the annual maximum observed volume, Apr of the following year. The volume loss is the difference between the maximum and Oct values.

Salinity (SMOS) microwave radiometer have provided a record of seasonal (October to April) ice thickness and volume (Ricker et al. 2017) since the 2010/11 winter; a summer record has also been developed (Landy et al. 2022). Since 2018, the laser altimeter on the NASA Ice, Cloud and land Elevation Satellite-2 (ICESat-2) satellite has also provided thickness estimates (Petty et al. 2020, 2021, 2023). Some differences between these two products are seen in the monthly winter average thickness, but both show 2022 thickness on the high end of the short time series (Fig. 5.13a); ICESat-2 did not compute an April 2022 average due to some missing data during the month. Spatially, the CryoSat-2/SMOS April thickness map (Fig. 5.13b) shows the typical pattern of thicker ice along the Canadian Archipelago. However, the anomaly map indicates thinner ice than the 2010–22 average in that region (Fig. 5.13c). Elsewhere, April 2022 ice was thicker in the Beaufort Sea and the East Siberian Sea (contributing to delayed ice loss there), but thinner in the Laptev and Kara Seas, and particularly along the north coast of Greenland.

Sea-ice thickness is integrated with ice concentration to provide winter volume estimates for 2010–22. The change from winter maximum volume to summer minimum and back to winter over the years illustrates the strong seasonal cycle and interannual variability (Fig. 5.14). There is little indication of a trend through the relatively short 11-year time series. After a record-low maximum volume in April 2021, there was a relatively small summer loss, which was then followed by a strong increase in sea ice through the October 2021 to April 2022 winter. This resulted in a notable increase in April 2022 volume compared to April 2021, as was also indicated by the average thickness (Fig. 5.13a).

f. Greenland Ice Sheet

—K. Poinar, K. D. Mankoff, T. A. Moon, B. D. Loomis, X. Fettweis, R. S. Fausto, T. L. Mote, C. D. Jensen, A. Wehrlé, and M. Tedesco

The Greenland Ice Sheet (GrIS) contributes directly to global sea levels when ice melts or breaks off into the ocean, increasing coastal erosion and flooding. Currently, the equivalent of ~7.4 m of eustatic sea level is contained in the GrIS (Morlighem et al. 2017). The GrIS has lost ice mass every mass balance year (1 September of the preceding year through 31 August) since 1998 (Mouginot et al. 2019). In 2022 (September 2021–August 2022), the Gravity Recovery and Climate Experiment Follow-on (GRACE-FO) satellite mission measured a GrIS mass loss of –165±18 Gt, the equivalent of ~0.5 mm eustatic sea level rise (Fig. 5.15). This loss was 95 Gt (37%) less than the 2002–22 average of –260±11 Gt.

The overall mass balance comprises surface mass balance (SMB, the accumulated snowfall minus the meltwater runoff) and solid ice discharge (break-off/calving of glacial ice directly into the ocean). In 2022, the SMB was above average, but within the 1991–2020 interannual variability. The highest cumulative snowfall since 1996 drove the relatively large SMB. However, melt in September 2022, just proceeding the standard mass balance year, was unprecedented, with a record-breaking number of melting days at multiple sites. This included melt at Summit Station (3216 m a.s.l.), which has been observed only four other times in its 34-year observation history, and never in September.

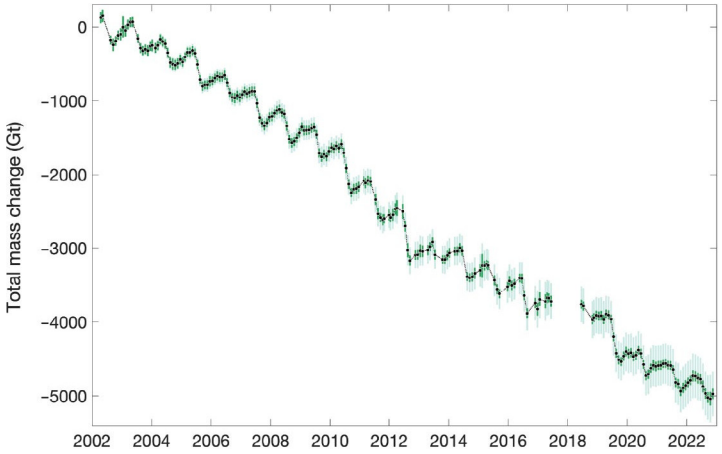

Fig. 5.15. Total mass change (Gt) of the GrIS from 2002 through mid-Nov 2022 determined from GRACE (2002–17) and GRACE-FO (2018–present; Tapley et al. 2019). Monthly estimates are shown as black circles, and 2-sigma uncertainties are provided with (light green) and without (dark green) errors due to leakage of external signals to the trend (i.e., mass changes near Greenland but not associated with the GrIS).

The 2-meter air temperature observations at 16 Danish Meteorological Institute predominantly coastal, land-based weather stations from September 2021 through August 2022 showed temperature anomalies between −0.3°C and +1.0°C, close to or slightly above the 1991–2020 average. While autumn (September–November 2021) temperatures were variable, winter (December 2021–February 2022) temperatures were predominantly close to or above average. Spring (March–May 2022) temperatures were also variable, but summer (June–August 2022) temperatures were slightly below average. On-ice weather stations operated by the Programme for Monitoring of the Greenland Ice Sheet (PROMICE) at the Geological Survey of Greenland and Denmark showed June air temperatures ~1 std. dev. below average and several snowfall events that month. By July and August, PROMICE temperatures were all within 1 std. dev. of the 2008–22 average. September was unusually warm (>1 std. dev. above average), due in part to a persistent high-pressure weather system over the southeast coast and a low-pressure system over the Canadian Arctic Archipelago that, together, imported warm, moist southerly air over Greenland in early September. This system brought thick clouds and heavy rain to western Greenland.

Ablation (ice loss via melt or other processes) measured by PROMICE (Fig. 5.16a) was also close to the 1991–2020 average. Regional exceptions were a +70% ablation anomaly at Thule in northwest Greenland and −42% at Kronprins Christians Land in northeast Greenland. Surface melting determined daily from the Special Sensor Microwave Imager/Sounder (SSMIS; Fig. 5.16b) also indicated an overall typical melt season. The southwest and northeast experienced more melt days than average, although the overall lower total melt, shown in Fig. 5.16a, suggests that

on average, the melt on these days was of lower volume. The southeast experienced fewer melt days than average; however, on 4–5 September, the warm air mass mentioned above descended from the ice sheet summit and initiated substantial melt there.

Only twice in 2022 did SSMIS observe melt conditions on >30% of the ice sheet surface (Fig. 5.16c): a July melt episode that peaked at 688,000 km^2 (42%) of the surface experiencing melt and the early September melt episode when 592,000 km^2 (36%) of the surface melted. Another series of unprecedented melt events occurred in late September, when warm air associated with the remains of Hurricane Fiona reached Greenland and melt occurred on 245,000 km^2 (15%) of the surface.

Ablation changes the reflective character of the ice sheet surface through the surface broadband albedo, or the fraction of incident light energy it reflects at all wavelengths. Ablation can expose bare glacial ice, which has a lower albedo (i.e., absorbs more energy) than snow cover. The annual transition from a snow-covered surface to a bare glacial ice surface creates a step change in surface broadband albedo (Ryan et al. 2019; Wehrlé et al. 2021).

The annually averaged summer albedo measured from Sentinel-3 and the Moderate Resolution Imaging Spectroradiometer (MODIS) was above (more reflective than) average (Figs. 5.17a,b), especially in the western ablation zone and coastal areas in the east and northeast (Wehrlé et al. 2021). Seasonally, the high albedo paired with average or below-average bare-ice area through the summer (Fig. 5.17c). The bare-ice area reached ~130,000 km^2 (8%) of the ice-sheet surface on 1 August before dropping below 100,000 km^2, then peaked at ~140,000 km^2 during the abnormally warm September. A September bare-ice area maximum is unique in the six-year observational record.

The Modèle Atmosphérique Régional (MARv3.13) polar regional climate model, forced by the fifth European Centre for Medium-Range Weather Forecasts (ECMWF) Reanalysis (ERA5; Hersbach et al. 2020) fully coupled with a snow energy balance model, provides SMB figures at a horizontal resolution of 15 km. We present ice sheet-wide totals here. The total SMB was 436 Gt yr^{-1}, within the 1991–2020 average of 339±123 Gt yr^{-1}. This occurred from a combination of 12% larger snowfall accumulation than average (784 Gt yr^{-1}, the highest accumulation since 1996), average meltwater runoff (350 Gt yr^{-1}), average sublimation and

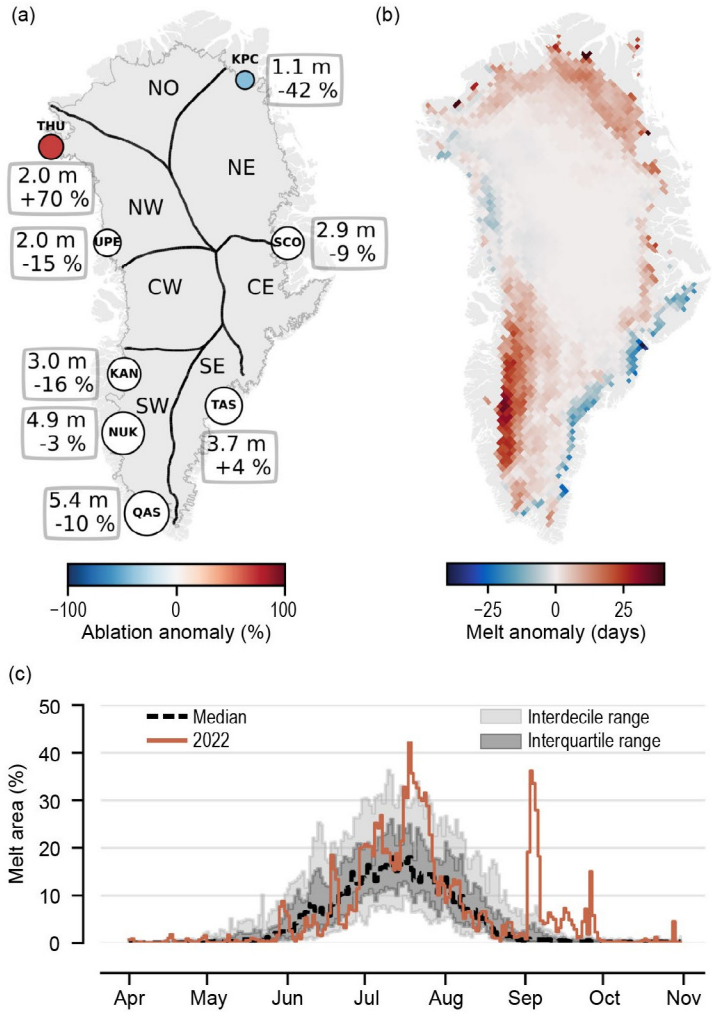

Fig. 5.16. (a) Net ablation for 2022 (m, top number) measured by PROMICE weather transects and referenced to the 1991–2020 period (%, bottom number). Circles are scaled in size to net ablation and scaled in color to the anomaly. White circles indicate anomaly values within methodological and measurement uncertainty. Stations are: Thule (THU), Upernavik (UPE), Kangerlussuaq (KAN), Nuuk (NUK), Qassimuit (QAS), Tasiliiq (TAS), Scoresby Sund (SCO), and Kronprins Christians Land (KPC). The regions North (NO), Northeast (NE), Northwest (NW), Central East (CE), Central West (CW), Southeast (SE), and Southwest (SW) are referenced in Fig. 5.18. (b) Number of melt days expressed as an anomaly with respect to the 1991–2020 reference period, from daily SSMIS 37 GHz, horizontally polarized passive microwave radiometer satellite data (Mote 2007). (c) Surface melt extent as a percentage of the ice sheet area during 2022 (solid orange) derived from SSMIS.

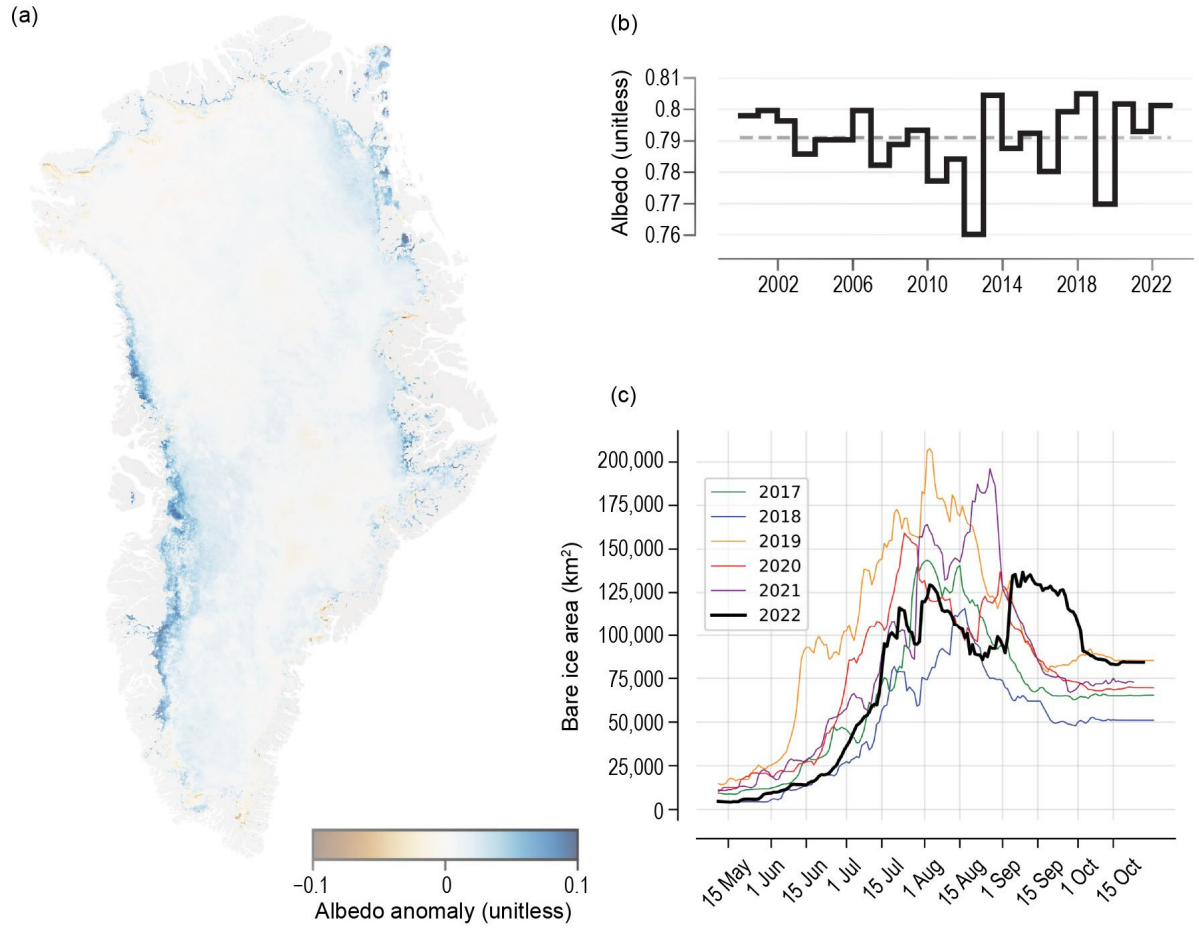

Fig. 5.17. (a) Albedo anomaly for Jun–Aug 2022 measured from Sentinel-3 data, relative to a 2017–2021 reference period (Wehrlé et al. 2021). (b) Time series for average Greenland Ice Sheet Jun–Aug albedo from MODIS. (c) Bare ice area (km²) measured from Sentinel-3 observations, with 2022 in black (Wehrlé et al. 2021).

evaporation (50 Gt yr^{-1}), and substantially greater annual rainfall than average (54 Gt yr^{-1}, an anomaly of +65% and >2 std. dev. above the mean), roughly half of which refroze in the snowpack. Much of the rainfall occurred in September, when fresh snow covered the ice sheet. That month, meltwater production was seven times larger than the 1991–2020 September average; snowfall quantities were also high, which allowed a large portion of this melt and rainwater to refreeze. This has the potential to affect local SMB in future melt seasons by forming ice lenses, which inhibit downward percolation of meltwater, allowing it to run off instead of being retained in the snowpack.

The second factor in the overall mass balance of the GrIS is solid ice discharge, which occurs around the perimeter of the ice sheet at hundreds of ice–ocean boundaries. Discharge is far less variable year-to-year than SMB, as continental ice flow responds to environmental changes relatively slowly (Mankoff et al. 2021). The 2022 discharge was 506±47 Gt yr^{-1} (Fig. 5.18), which is within the 1991–2020 average of 488±44 Gt yr^{-1}. In 2022, the sectors with the highest discharge continued to be the southeast (144 Gt yr^{-1}) and the northwest (115 Gt yr^{-1}), with a modest increasing trend in the northwest over the past ~20 years.

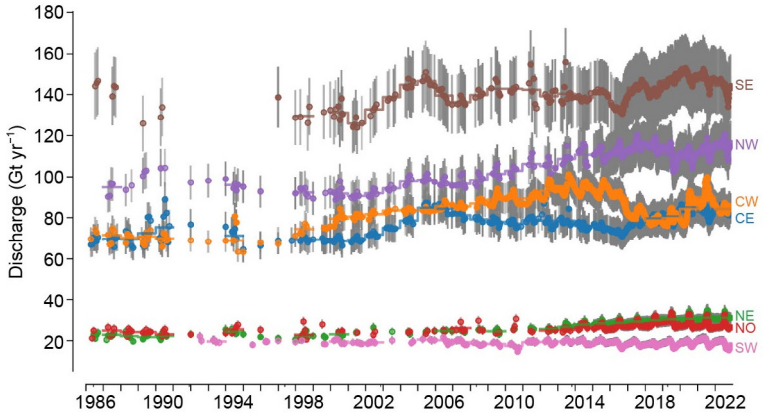

Fig. 5.18. Solid ice discharge (Gt yr^{-1}) based on ice velocity and thickness (Mankoff et al. 2020) by region of the Greenland Ice Sheet, as shown in Fig. 5.16a. Gray bars show uncertainty of ±10%.

g. Terrestrial snow cover

—L. Mudryk, A. Elias Chereque, C. Derksen, K. Luojus, and B. Decharme

Many components of the Arctic land surface are directly influenced by snow cover from autumn through spring, including the surface energy budget and ground thermal regime, with implications for the carbon cycle, permafrost, and terrestrial and freshwater ecosystems (Brown et al. 2017; Meredith et al. 2019, and references therein). Even following the snow-cover season, the influence of spring snow melt persists through impacts on river discharge timing and magnitude, surface water, soil moisture, vegetation phenology, and fire risk (Meredith et al. 2019).

Snow-cover extent anomalies (relative to the 1991–2020 climatology) in spring (May and June) 2022 are shown separately for the North American and Eurasian terrestrial sectors of the Arctic in Fig. 5.19 (data from the NOAA snow chart climate data record; Robinson et al. 2012). May anomalies were near average in the North American sector (29th lowest in the 56-year record available since 1967) but below average over the Eurasian sector (ninth lowest). Rapid snow loss after May resulted in low snow-cover extent across both sectors in June (second and third lowest, respectively).

Snow-cover duration (SCD) anomalies (relative to a 1998/99–2017/18 climatology) across the Arctic region for the 2021/22 snow season are shown in Figs. 5.20a,b as percent differences relative to the climatological number of snow-free days (data from the NOAA daily Interactive Multisensor Snow and Ice Mapping System [IMS] snow-cover product; U.S. National Ice Center 2008). Anomalies in the total number of days with snow cover were computed separately for each half of the snow season: August 2021–January 2022, referred to as "onset period," and February–July 2022, referred to as "melt period." Onset anomalies indicate that snow cover during 2021 began earlier than normal over Alaska, eastern Siberia, and Scandinavia, and began later than normal over central Arctic Canada and parts of central Siberia (Fig. 5.20a), a pattern consistent with below-average autumn temperatures (Thoman et al. 2022). Melt anomalies during spring 2022 show anomalously low SCD (indicating early melt) across much of the Arctic, with three areas as especially anomalous: east of the Ural Mountains, across eastern Siberia, and over the Canadian Arctic Archipelago (Fig. 5.20b), consistent with high spring and summer

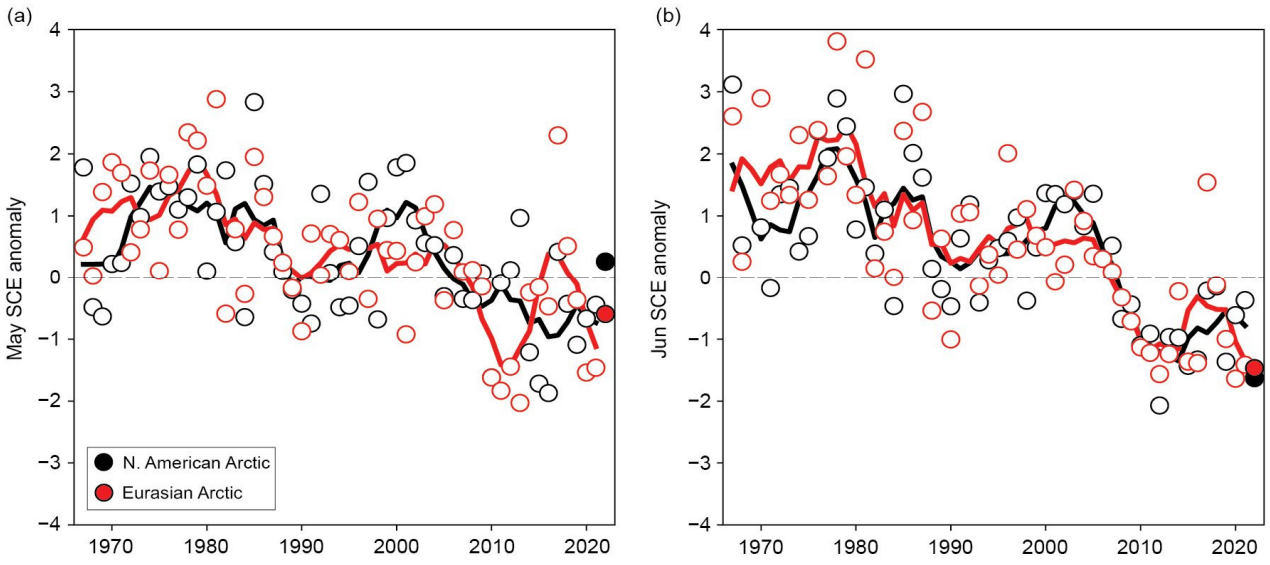

Fig. 5.19. Monthly snow-cover extent (SCE) anomalies for Arctic terrestrial land areas (>60°N) for (a) May and (b) Jun from 1967 to 2022. Anomalies are relative to the 1991–2020 average and standardized (each observation differenced from the mean and divided by the standard deviation, and thus unitless). Solid black and red lines depict 5-yr running means for North America and Eurasia, respectively. Filled circles highlight 2022 anomalies. (Source: Robinson et al. 2012).

2022 temperature anomalies (see Fig. 5.2). Similar to spring 2021, the duration of the spring 2022 snow-free period across broad expanses of Eurasia was 30%–50% longer than normal.

Snow water equivalent (SWE) characterizes the amount of water stored as snow, which enters the hydrologic cycle once it melts. SWE data during April–June were obtained from four daily-frequency gridded products over the 1981–2022 period: 1) the European Space Agency Snow Climate Change Initiative (CCI) SWE version 2 product derived through a combination of satellite passive microwave brightness temperatures and climate-station snow-depth observations (Luojus et al. 2022); 2) the Modern-Era Retrospective Analysis for Research and Applications version 2 (MERRA-2; GMAO 2015) daily SWE fields; 3) SWE output from the European Centre for Medium-Range Weather Forecasts (ECMWF) Reanalysis version 5-Land (ERA5-Land) analysis (Muñoz Sabater 2019); and 4) the physical snowpack model Crocus (Brun et al. 2013) driven by near-surface meteorological variables from ERA5. Reduced availability of climate-station

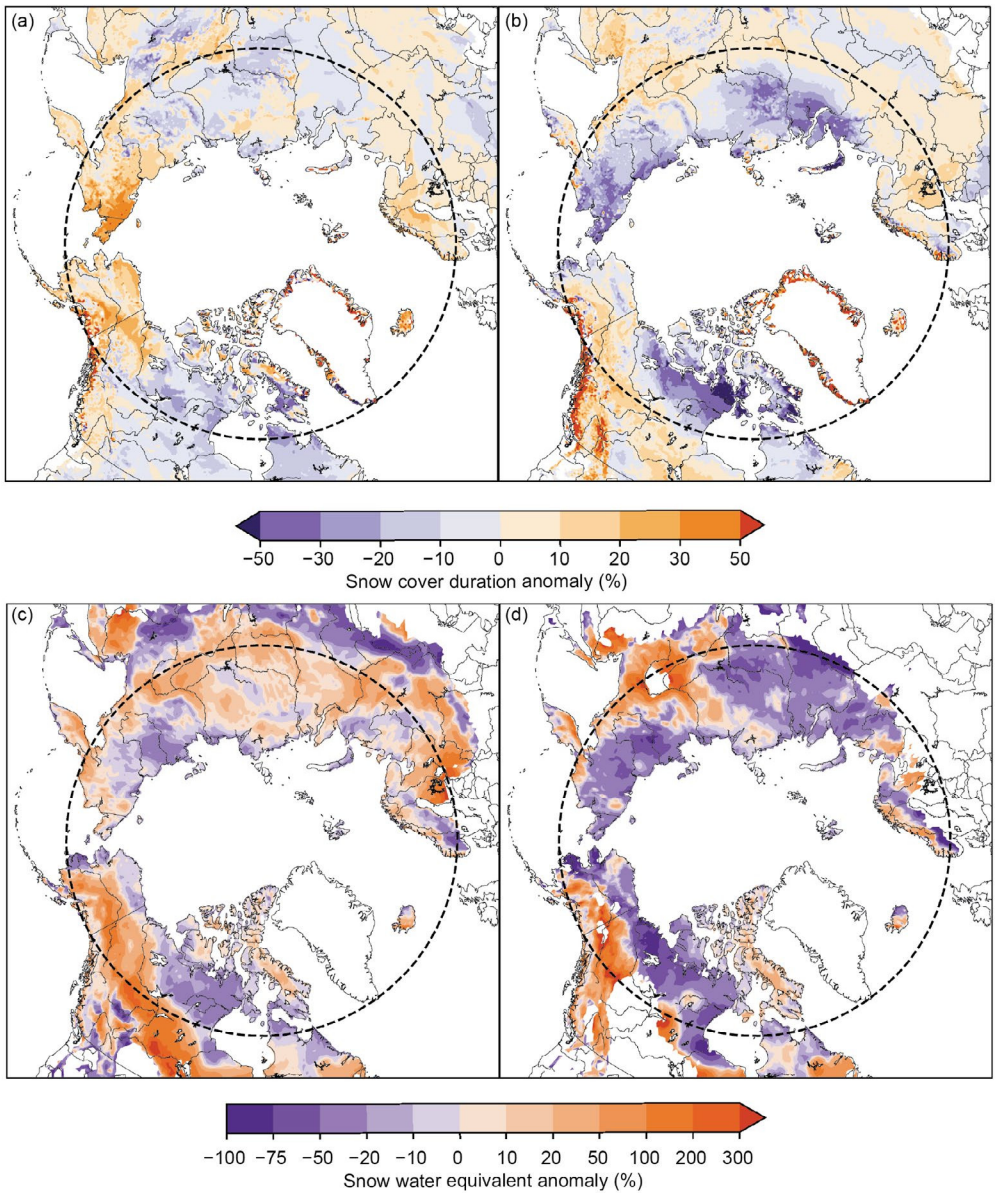

Fig. 5.20. Snow-cover duration (SCD) anomalies (% difference relative to climatological number of snow-free days for the 1998/99–2017/18 baseline) for the 2021/22 snow year: (a) snow onset period (Aug 2021–Jan 2022); and (b) snow melt period (Feb–Jul 2022). Purple (orange) indicates fewer (more) days than average. Snow water equivalent (SWE) anomalies (% difference from the 1991–2020 baseline) in 2022 for (c) Apr and (d) May. Purple (orange) indicates less (more) snow than average. Latitude 60°N marked by black dashed circle; land north of this defines the Arctic terrestrial area considered in this study. (Source: (a),(b) U.S. National Ice Center [2008]; (c),(d) four SWE products from Snow CCI [Luojus et al. 2022], MERRA2 [GMAO 2015], ERA5-Land [Muñoz Sabater 2019], and Crocus [Brun et al. 2013].)

snow-depth measurements limits the accuracy of the Snow CCI SWE product during May and June, hence it is omitted for those months. An approach using gridded products is required because in situ observations alone are too sparse to be representative of hemispheric snow conditions, especially in the Arctic.

For April, the spatially variable SWE data from each product are aggregated across Arctic land regions (>60°N) for both North American and Eurasian sectors and standardized relative to the 1991–2020 baseline to produce April snow-mass anomalies. The ensemble mean anomalies and the range of estimates among the products are presented in Fig. 5.21. April is chosen because it is the month in which total snow mass across the terrestrial pan-Arctic region typically peaks, reflecting total snowfall accumulations since the preceding autumn before increasing temperatures during May and June lead to melt. The 2022 anomalies highlighted in Fig. 5.21 indicate that snow accumulation was moderately above the 1991–2020 average across both the Eurasian and North American Arctic. Figures 5.20c,d illustrate how the SWE data varied spatially during both April and May, presented as percent differences of the ensemble-mean field relative to the 1991–2020 baseline. In April, both continents had mixed distributions of SWE: the northern regions of Arctic Eurasia had lower SWE than normal with higher-than-normal SWE located farther south. In North America, the central Canadian Arctic and northern Alaska had lower-than-normal SWE while higher-than-normal accumulations were present south of the Brooks Range and across the Yukon Territory. Melt during May caused widespread reductions in SWE across the Eurasian Arctic and further reduced the snowpack where it was already lower than average in the North American Arctic, consistent with the pattern of snow-cover duration anomalies shown in Fig. 5.20b. By June (not shown), SWE had melted across almost the entire Arctic except for the northern portion of the Canadian Arctic Archipelago, the Scandinavian mountains, and northernmost Taymyr Peninsula, consistent with the near-record lows in June snow extent across both continents (Fig. 5.19).

Similar to the previous year, the 2021/22 Arctic snow season saw a combination of increased snow accumulation (expressed as higher-than-average April snow mass in Fig. 5.21) and early snow melt (expressed in Fig. 5.20b as shorter snow-cover duration during the melt period). There is no significant trend in pan-Arctic snow mass since 1980, but there are significant reductions in spring snow extent, which has been persistently below normal for the last 15 years (Fig. 5.19). These attributes are consistent with the expected changes to Arctic snow cover in a warmer Arctic: regionally-dependent changes in snow accumulation but Arctic-wide reductions in spring snow extent and snow-cover duration (Meredith et al. 2019).

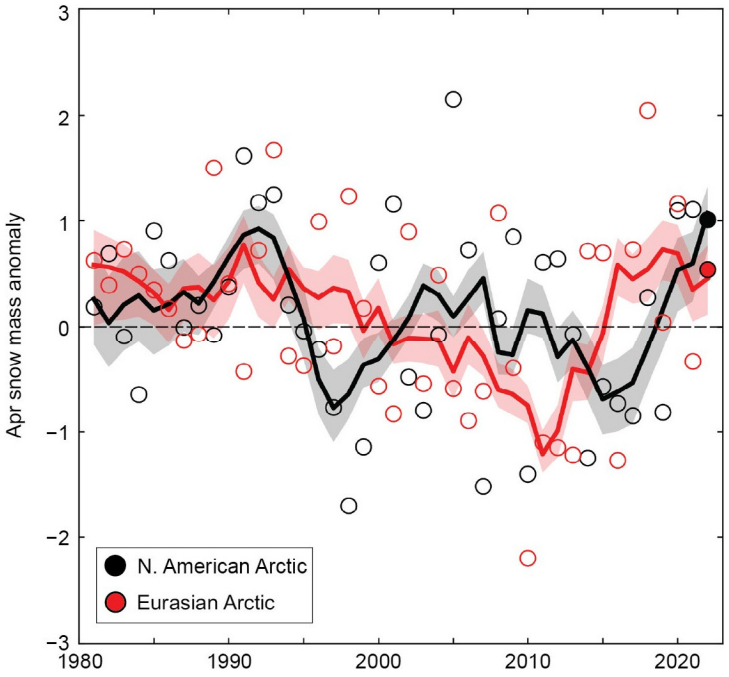

Fig. 5.21. Mean Apr snow mass anomalies for Arctic terrestrial areas calculated for North American (black) and Eurasian (red) sectors of the Arctic over 1981–2022. Anomalies are relative to the average for 1991–2020 and standardized (each observation differenced from the mean and divided by the standard deviation, and thus unitless). Filled circles highlight 2022 anomalies. Solid black and red lines depict 5-yr running means for North America and Eurasia, respectively, and the spread among the running means for individual datasets is shown in shading. (Source: four SWE products from Snow CCI [Luojus et al. 2022], MERRA2 [GMAO 2015], ERA5-Land [Muñoz Sabater 2019], and Crocus [Brun et al. 2013].)

h. Arctic river discharge

—J. W. McClelland, A. I. Shiklomanov, A. Suslova, M. Tretiakov, R. M. Holmes, R. G. M. Spencer, S. E. Tank, and S. Zolkos

The Arctic Ocean accounts for approximately 1% of the global ocean's volume but receives more than 10% of global river discharge (McClelland et al. 2012). Consequently, effects of river inputs on ocean processes are more pronounced in the Arctic and changes in river inputs have greater potential to impact ocean physics, chemistry, and biology than in other ocean basins. Because rivers naturally integrate the processes that are occurring throughout their watersheds, trends in the discharge and chemistry of Arctic rivers can also be indicative of widespread terrestrial change including permafrost thaw and the amount or seasonality of precipitation (Rawlins et al. 2010; Holmes et al. 2013).

Multiple studies over the past 20 years have demonstrated that discharge from Arctic rivers is increasing. Evidence first emerged from long-term Russian datasets (Peterson et al. 2002) and more recently from shorter U.S. and Canadian datasets (Durocher et al. 2019). While uncertainty remains around drivers of this trend, it is consistent with intensification of the Arctic hydrologic cycle (Rawlins et al. 2010). Warming is driving increased atmospheric moisture transport into the Arctic, resulting in greater precipitation (Box et al. 2019; section 5c). This is particularly evident during colder months of the year. For example, snowfall has increased during autumn and early winter in western Siberia (Wegmann et al. 2015) and in the Canadian Arctic (Kopec et al. 2016; Yu and Zhong 2021).

Fig. 5.22. Watersheds of the eight largest Arctic rivers featured in this analysis. Collectively, these rivers drain approximately 70% of the 16.8 million km² pan-Arctic watershed (indicated by the red boundary line). The red dots show the location of the discharge monitoring stations.

River discharge was last included in the *State of the Climate in 2020* report; therefore, discharge data for 2021 and 2022 are presented here. Data presentation and analysis focus on eight rivers that collectively drain much of the pan-Arctic watershed (Fig. 5.22). Six of these rivers are in Eurasia and two are in North America. Discharge measurements for the six Eurasian rivers began in 1936, whereas discharge measurements did not begin until 1973 for the Mackenzie River and 1976 for the Yukon River in North America. Years are presented as "water years", 1 October–30 September, a common practice in hydrology to align runoff and associated precipitation within the same year. Thus, water year 2022 covers the period 1 October 2021– 30 September 2022. The data used in this analysis are freely available through the Arctic Great Rivers Observatory (https://arcticgreatrivers.org/).

Discharge data for 2021 and 2022 are compared to a 1991–2020 reference period in this report, a change from the 1981–2010 reference period used for the previous report. Both the old and new reference periods are included in Table 5.1 to allow for continuity between reports. Combined annual discharge averaged 2397 km³ during the new reference period and 2348 km³ during the old reference period. While this only represents a modest 2.1% increase between the two periods, it reflects increases observed in seven out of eight individual rivers and is consistent with long-term trends of increasing Arctic river discharge.

Combined annual discharge for the eight rivers was 2555 km^3 for 2021 and 2516 km^3 for 2022 (Table 5.1). These values exceeded the 1991–2020 reference average by approximately 7% and 5%, respectively. Differences relative to the reference period were largely driven by elevated discharge in the Yukon, Mackenzie, and Yenisey Rivers, which exceeded their associated reference averages in both years. Annual discharge reached a record high in 2021 for the Yenisey. Although data accuracy for this river has declined significantly since 2003 due to a lack of rating curve updates (Tretiyakov et al. 2022), elevated values were reported across multiple gauges on the Yenisey during the summer and autumn of 2021. Annual discharge values in the Severnaya Dvina, Pechora, Ob, and Kolyma were lower than the 1991–2020 reference average in both 2021 and 2022.

Monthly data for the Eurasian rivers show that June discharge during 2021 and 2022 was well below the reference average, whereas discharge during most other months was above the reference average (Fig. 5.23a). In contrast, discharge in the North American rivers during 2021 and 2022 was above the reference average during all months (Fig. 5.23b). These results are still provisional, but patterns represented in aggregate were also evident in individual rivers. The observed increases during winter months on both sides of the Arctic are consistent with findings of other

Table 5.1. Annual discharge (km^3) for the eight largest Arctic rivers. Results are shown for 2021 and 2022 as well as mean values for old (1981–2010) and new (1991–2020) reference periods. *Italicized* values indicate provisional data and are subject to modification until official data are published.

Year[1]	Yukon (N. America)	Mackenzie (N. America)	S. Dvina (Eurasia)	Pechora (Eurasia)	Ob′ (Eurasia)	Yenisey (Eurasia)	Lena (Eurasia)	Kolyma (Eurasia)	Total
2022	*240*	*349*	*85*	*96*	*381*	*663*	*630*	*72*	*2516*
2021	*233*	*382*	*82*	*89*	*415*	*745*	*541*	*68*	*2555*
1981–2010	205	288	104	114	398	612	557	70	2348
1991–2020	*211*	*291*	*106*	*116*	*416*	*606*	*573*	*78*	*2397*

[1] Year refers to Water Year (1 October of the previous year to 30 September of the noted year)

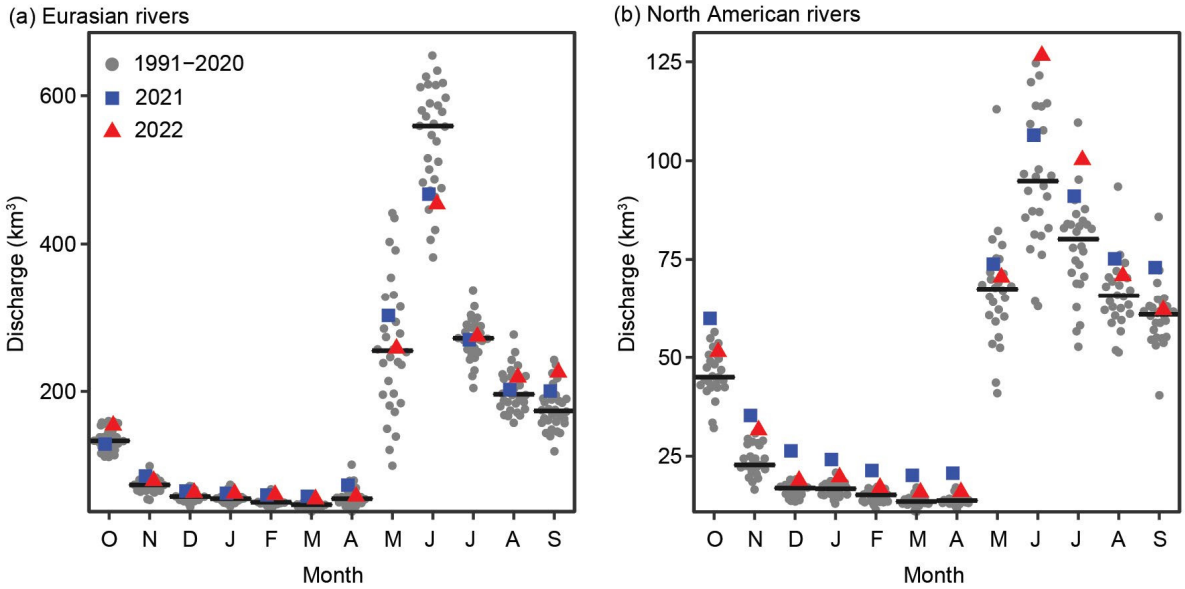

Fig. 5.23. Monthly discharge (km^3) in (a) Eurasian and (b) North American rivers for 2021 (blue squares) and 2022 (red triangles) compared to monthly discharge throughout the 1991–2020 reference period (gray circles). The black bars indicate average monthly discharge during the reference period. Note the different magnitudes of discharge between the Eurasian and North American rivers (see y-axes).

recent studies of northern rivers (Gohari et al. 2022; Whitfield et al. 2021; Hiyama et al. 2023). Widespread changes in winter discharge have been attributed to increasing baseflow as a consequence of general warming and associated permafrost degradation that supports greater groundwater contributions as well as changes in the timing and magnitude of snowmelt events (Shrestha et al. 2021; Liu et al. 2022).

The 87-year time series available for the Eurasian Arctic rivers demonstrates a continuing, and perhaps accelerating, increase in their combined discharge (Fig. 5.24a). The positive linear trend across this entire time series indicates that the average annual discharge of Eurasian Arctic rivers is increasing by 2.5 $km^3\ yr^{-1}$. When data are considered from 1976 through 2022 (the period of record for North American rivers), the average annual increase in discharge for Eurasian Arctic rivers is 4.2 $km^3\ yr^{-1}$. For the North American Arctic rivers, the average discharge increase over the period of record is 1.5 $km^3\ yr^{-1}$. These observations show that, although river discharge varies widely over interannual-to-decadal timeframes, longer-term increases in river discharge are a pan-Arctic phenomenon. Evidence of increasing Arctic river discharge is strongest for Eurasian rivers where datasets are longest, but the signal of change in North American rivers is becoming increasingly robust as discharge datasets lengthen. This serves as a reminder that maintaining long-term datasets is crucial for tracking and understanding change.

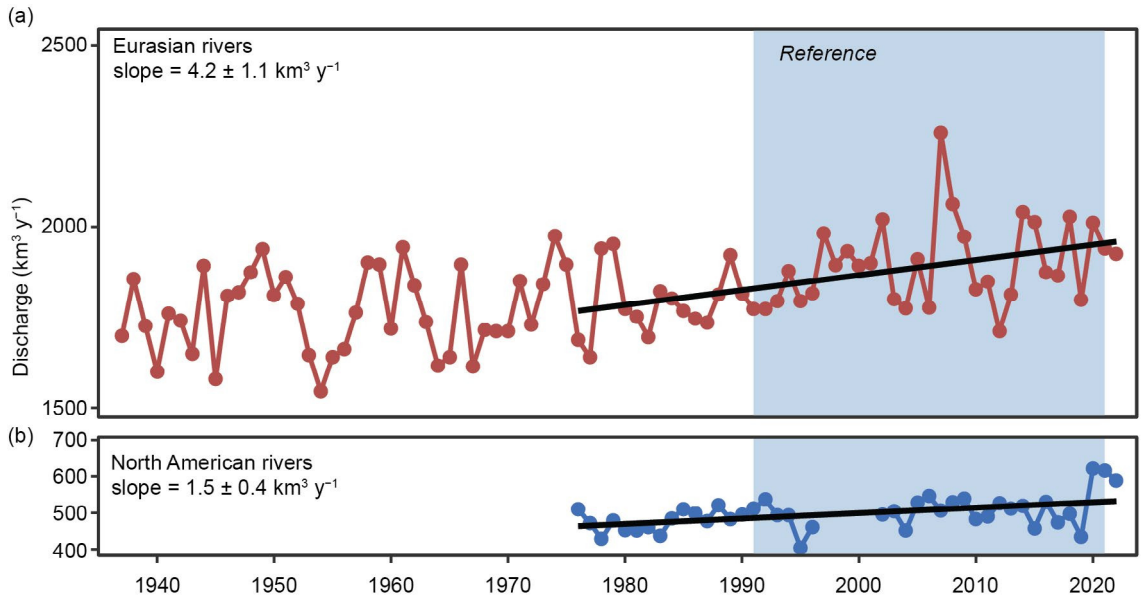

Fig. 5.24. Long-term trends in annual discharge (km^3) for (a) Eurasian and (b) North American Arctic rivers. The North American time series gap from 1996 to 2001 is due to insufficient data availability during those years. Reported slopes ($p < 0.001$ for both) are for 1976–2022.

i. Permafrost

—S. L. Smith, V. E. Romanovsky, K. Isaksen, K. E. Nyland, N. I. Shiklomanov, D. A. Streletskiy, and H. H. Christiansen

Permafrost refers to earth materials (e.g., bedrock, mineral soil, organic matter) that remain at or below 0°C for at least two consecutive years, although most permafrost has existed for much longer (centuries to several millennia). Overlying the permafrost is the active layer, which thaws and refreezes annually. Permafrost underlies extensive regions of the high-latitude landscape (Brown et al. 1997) and, especially if ice-rich, can play a critical role in the stability of Arctic landscapes. Warming of permafrost, active layer thickening, and ground-ice melt cause changes in surface topography, hydrology, and landscape stability, with implications for Arctic infrastructure and ecosystem integrity, as well as human livelihoods (Romanovsky et al. 2017; Hjort et al. 2022; Wolken et al. 2021). Changes in permafrost conditions can also affect the rate of greenhouse gas release to the atmosphere, with the potential to accelerate global warming (Schuur 2020).

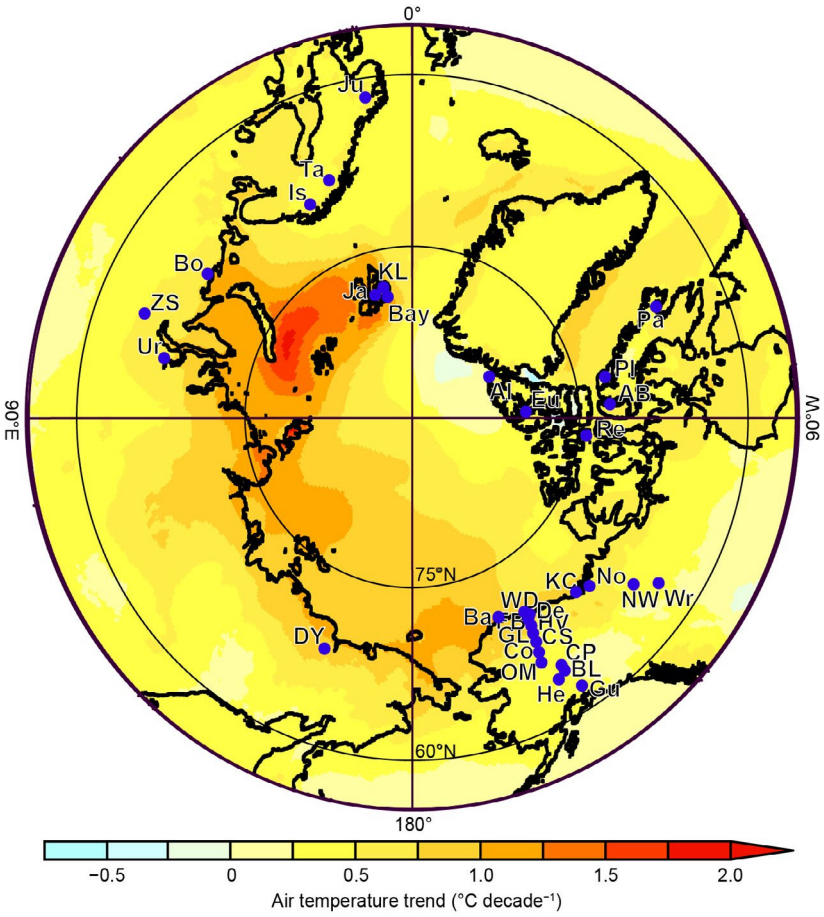

Fig. 5.25. Locations of the permafrost temperature monitoring sites (for which data are shown in Fig. 5.26), superimposed on average surface air temperature trends (°C decade^{-1}) during 1981–2020 from ERA5 reanalysis (Hersbach et al. 2020; data available at https://cds.climate.copernicus.eu). See Table 5.2 for site names. Information about these sites is available at http://gtnpdatabase.org/,http://permafrost.gi.alaska.edu/sites_map, and https://www2.gwu.edu/~calm/.

Permafrost conditions respond to shifts in the surface energy balance through a combination of interrelated changes in ground temperature and active layer thickness (ALT). Near the surface, ground temperatures fluctuate seasonally, while below the depth of seasonal temperature variation, ground temperatures reflect longer-term changes in climate. Long-term changes in permafrost temperatures are driven by changes in air temperature (Romanovsky et al. 2017); however, permafrost temperature trends also show local variability due to other important influences such as snow cover, vegetation characteristics, and soil moisture. Monitoring sites across the Arctic (Fig. 5.25) have been recording ground temperature in the upper 30 m for up to five decades, providing critical data on changes in permafrost stability. Observed changes in ALT are more reflective of shorter-term (year-to-year) fluctuations in climate and are especially sensitive to changes in summer air temperature and precipitation.

1. PERMAFROST TEMPERATURES

Permafrost temperatures continue to increase on a decadal time scale across the Arctic. Greater increases in permafrost temperature are generally observed in colder permafrost (temperature <–2°C) at higher latitudes (Smith et al. 2022a,b), partly due to greater increases in air temperature (Figs. 5.25, 5.26). Permafrost temperatures in 2022 were the highest on record at 11 of the 25 sites reporting. However, cooling that began in 2020 has continued at other sites and temperatures were lower in 2022 compared to 2021 at 13 sites (Fig. 5.26; Table 5.2). In the Beaufort-Chukchi region, permafrost temperatures in 2022 were up to 0.3°C lower than in 2021 at all sites except Utqiaġvik (Barrow; Fig 5.26a). The observed permafrost cooling in this region was a result of lower mean annual air temperatures after 2019. At Deadhorse (Prudhoe Bay, Alaska) for example, the average air temperature was almost 4°C lower in 2022 compared to 2018 and 2019. For discontinuous permafrost in Alaska and northwestern Canada, the 2022 permafrost temperatures were the highest on record at all sites except for three (Fig. 5.26b). Although the high-Arctic cold permafrost of Svalbard (Janssonhaugen) had been warmer each year from 2005 until 2019/20 (Isaksen et al. 2022), permafrost was colder in 2021 and 2022 but still among the five warmest years on record (Fig. 5.26d). In warmer permafrost at other Nordic sites, permafrost temperatures in 2022 were the highest on record. Permafrost was colder in 2022 at the one Russian site reporting.

Throughout the Arctic, the warming of permafrost with temperatures close to 0°C (i.e., at temperatures >–2°C) is slower (generally <0.3°C decade^{-1}) than colder permafrost sites due to latent heat effects related to melting ground ice. At cold continuous permafrost sites in the

Beaufort-Chukchi region, permafrost temperatures have increased by 0.3°C–0.7°C decade^{-1} (Fig. 5.26a; Table 5.2). In the eastern and high Canadian Arctic, similar increases (0.4°C–1.1°C decade^{-1}) have been observed (Fig. 5.26c; Table 5.2). Permafrost on Svalbard at the Janssonhaugen and Kapp Linne sites (Table 5.2), has warmed by about 0.7°C decade^{-1}. Significant permafrost warming has been detected to 100-m depth at Janssonhaugen (Isaksen et al. 2022).

Table 5.2. Rate of change in mean annual ground temperature (°C decade^{-1}) for permafrost monitoring sites shown in Fig. 5.25. For sites where measurements began prior to 2000, the rate of change for the entire available record and the period after 2000 are provided. The periods of record are shown in parenthesis below the rates of change. Stations with record-high temperatures in 2022 are shown underlined in red. Asterisks denote sites not reporting in 2022.

Region	Site	Entire Record	Since 2000
North of East Siberia *(Beaufort-Chukchi Region)*	Duvany Yar (DY)*	NA	+0.4 (2009–20)
Alaskan Arctic plain *(Beaufort-Chukchi Region)*	West Dock (WD), Deadhorse (De), Franklin Bluffs (FB), Barrow (Ba)	+0.4 to +0.7 (1978–2022)	+0.4 to +0.6 (2000–22)
Northern foothills of the Brooks Range, Alaska *(Beaufort-Chukchi Region)*	Happy Valley (HV), Galbraith Lake (GL)	+0.3 (1983–2022)	+0.3 (2000–22)
Northern Mackenzie Valley *(Beaufort-Chukchi Region)*	Norris Ck (No), KC-07 (KC)	NA	+0.6 to +0.7 (2008–22)
Southern foothills of the Brooks Range, Alaska *(Discontinuous Permafrost, Alaska and NW Canada)*	Coldfoot (Co), Chandalar Shelf (CS), Old Man (OM)	+0.1 to +0.3 (1983–2022)	+0.2 to +0.3 (2000–22)
Interior Alaska *(Discontinuous Permafrost, Alaska and NW Canada)*	College Peat (CP), Birch Lake (BL), Gulkana (Gu), Healy (He)	+0.1 to +0.3 (1983–2022)	<+0.1 to +0.3 (2000–22)
Central Mackenzie Valley *(Discontinuous Permafrost, Alaska and NW Canada)*	Norman Wells (NW), Wrigley (Wr)	Up to +0.1 (1984–2022)	<+0.1 to +0.2 (2000–22)
Baffin Island *(Baffin Davis Strait Region)*	Pangnirtung (Pa)*, Pond Inlet (PI)*	NA	+0.4 (2009–21)
High Canadian Arctic *(Baffin Davis Strait Region)*	Resolute (Re)	NA	+1.1 (2009–22)
High Canadian Arctic *(Baffin Davis Strait Region)*	Alert (Al) @ 15 m*, Alert (Al) @ 24 m	+0.6, +0.4 (1979–2022)	+0.9, +0.6 (2000–22)
North of West Siberia *(Barents Region)*	Urengoy 15-06* and 15-08* (Ur)	+0.2 to +0.5 (1974–2021)	+0.1 to +0.8 (2005–21)
Russian European North *(Barents Region)*	Bolvansky 56 and 65* (Bo)	+0.1 to +0.3 (1984–2022)	0 to +0.5 (2001–22)
Svalbard *(Barents Region)*	Janssonhaugen (Ja), Bayelva (Bay)*, Kapp Linne 1 (KL)	+0.7 (1998–2022)	+0.2 to +0.7 (2000–22)
Northern Scandinavia *(Barents Region)*	Tarfalarggen (Ta)*, Iskoras Is-B-2 (Is)	NA	+0.1 to +0.5 (2000–22)
Southern Norway *(Barents Region)*	Juvvasshøe (Ju)	+0.2 (1999–2022)	+0.2 (2000–22)

In the discontinuous permafrost regions of Scandinavia (Juvvasshøe and Iskoras), warming is continuing at rates of about 0.2°C decade^{-1}, with thawing occurring at Iskoras (Fig. 5.26d; Isaksen et al. 2022). Similar rates of warming were found for warm permafrost in Russia (e.g., Bolvansky #56; Malkova et al. 2022) and northwestern North America (Figs. 5.26b,d).

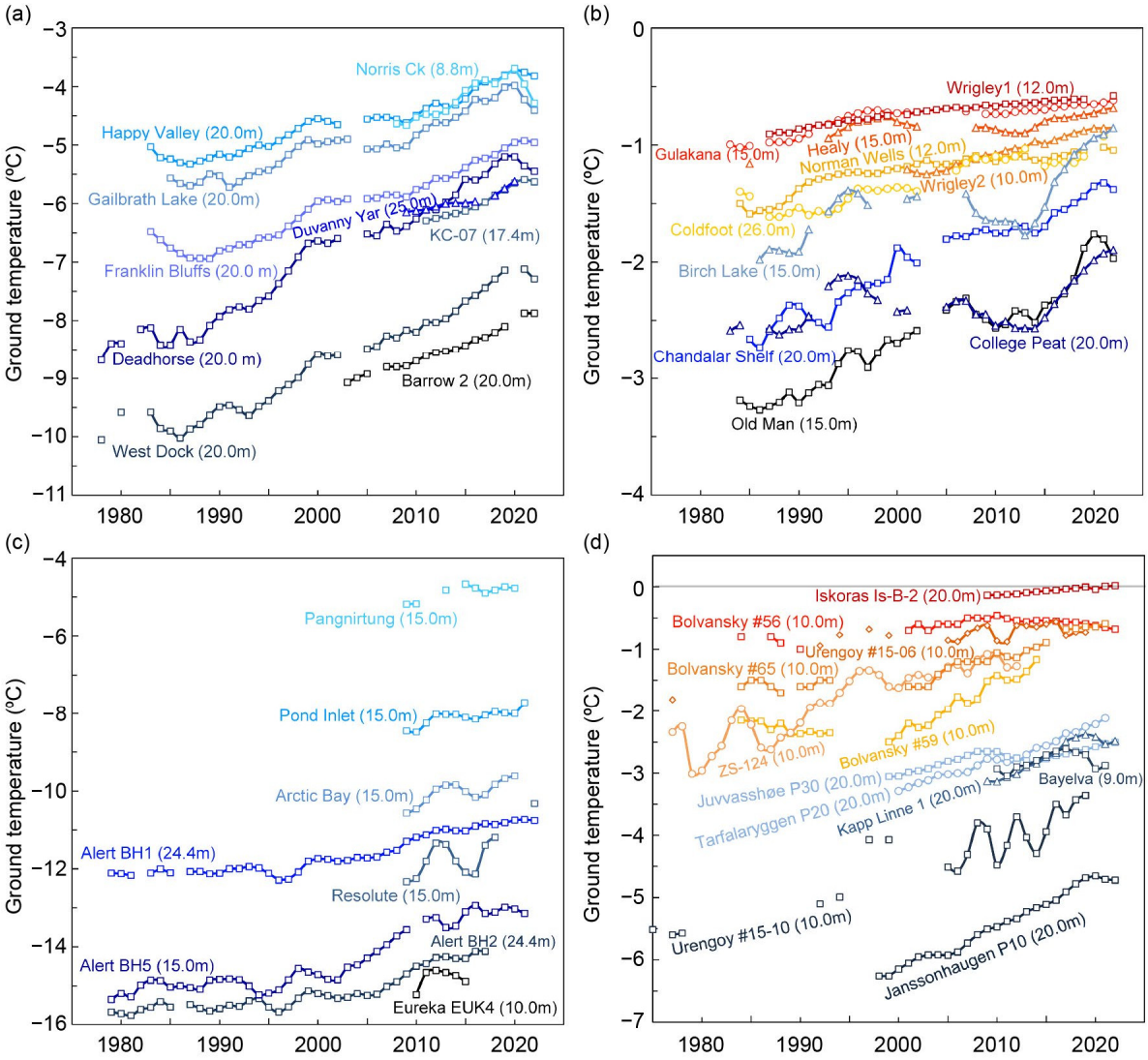

Fig. 5.26. Time series of mean annual ground temperature (°C) at depths of 9 m–26 m below the surface at selected measurement sites that fall roughly into Adaptation Actions for a Changing Arctic Project priority regions (see Romanovsky et al. 2017): (a) cold continuous permafrost of northwestern North America and northeastern East Siberia (Beaufort-Chukchi region); (b) discontinuous permafrost in Alaska and northwestern Canada; (c) cold continuous permafrost of eastern and High Arctic Canada (Baffin Davis Strait); and (d) continuous to discontinuous permafrost in Scandinavia, Svalbard, and Russia/Siberia (Barents region). Temperatures are measured at or near the depth of zero annual amplitude where the seasonal variations of ground temperature are less than 0.1°C. Note differences in y-axis value ranges. Borehole locations are shown in Fig. 5.25 (data are updated from Smith et al. 2022b).

2. ACTIVE LAYER THICKNESS

Active layer thickness is determined using direct measurements, such as mechanical probing and thaw tubes, and also indirectly by interpolation of the maximum seasonal depth of the 0°C isotherm from borehole temperature records. Long-term ALT trends shown in Fig. 5.27 are primarily generated from spatially distributed mechanical probing across representative landscapes to determine the top of permafrost (Shiklomanov et al. 2012).

Over the last 28 years, positive ALT trends are evident for all regions reported, but trends are less apparent for the Alaskan North Slope, northwest Canada, and East Siberia (Smith et al. 2022a). West Siberia, the Russian European North, and Interior Alaska all experienced ALT in 2022 well above the 2009–18 mean, continuing a several-year increase in ALT (e.g., Kaverin et al.

2021). The Russian European North, Interior Alaska, and West Siberia are experiencing the greatest rates of ALT increase over the observation period at 0.013, 0.015, and 0.016 m yr^{-1}, respectively.

Active layer thickness regional anomalies for summer 2022 were within 0.05 m of the 2009–18 mean for the North Slope of Alaska, Greenland, Svalbard, northwest Canada, and East Siberia. The negligible ALT trend for the Alaska North Slope and northwest Canada for example, may be the result of consolidation (subsidence) resulting from the thaw of ice-rich material, which is not accounted for by manual probing (Nyland et al. 2021; Smith et al. 2022a). Reduced ALT reported for 2022 for the Alaska North Slope, Greenland, Svalbard, and East Siberia may be due to a cooler summer (e.g., Nyland et al. 2021; Strand et al. 2021; Abramov et al. 2021).

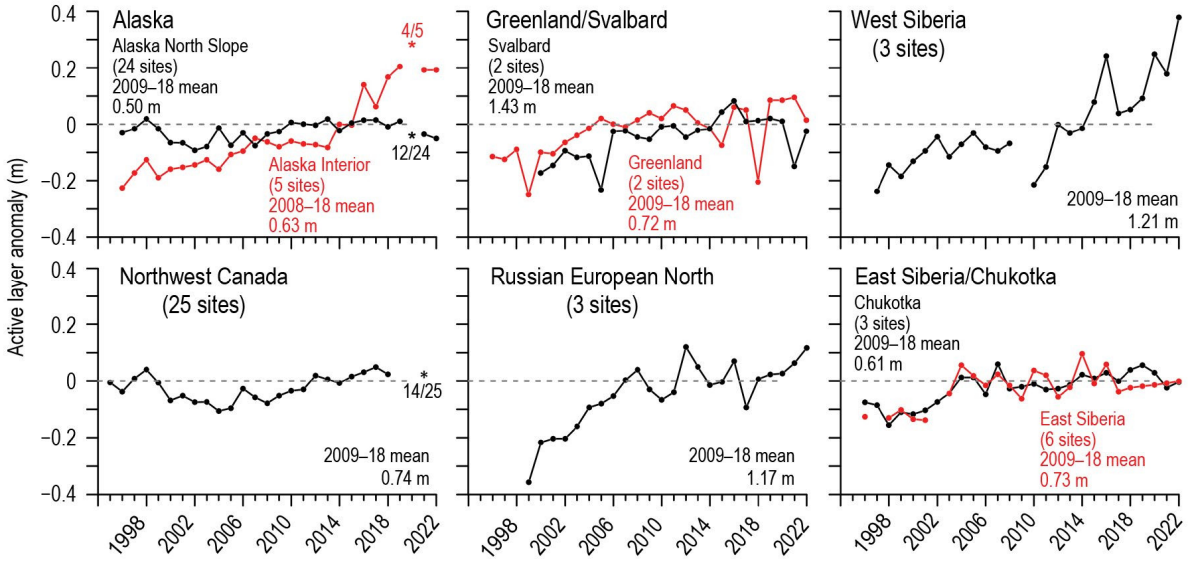

Fig. 5.27. Average annual active layer thickness (ALT) anomalies (m) relative to the 2009–18 mean for six Arctic regions as observed by the Circumpolar Active Layer Monitoring program. Positive and negative anomaly values indicate thicker or thinner ALT, respectively, than the 10-yr reference mean. Only sites with >20 years of continuous thaw depth observations are included. The number of sites and reference period mean ALT are provided on each figure panel. Asterisks indicate a lower number of observations due to pandemic-related restrictions, with the number of sites reporting provided on graph. Canadian ALT is derived from thaw tubes that record the maximum thaw depth over the previous year. Since Canadian sites were not visited in 2020 and 2021, the maximum thaw depth recorded during the 2022 visit could have occurred any summer from 2019 through 2021, although the data point is plotted in 2021. Site-specific data and metadata are available at www2.gwu.edu/~calm/.

j. Tundra greenness

—G. V. Frost, M. J. Macander, U. S. Bhatt, L. T. Berner, J. W. Bjerke, H. E. Epstein, B. C. Forbes, S. J. Goetz, M. J. Lara, R. Í. Magnússon, G. K. Phoenix, S. P. Serbin, H. Tømmervik, O. Tutubalina, D. A. Walker, and D. Yang

Earth's northernmost continental landmasses and island archipelagos are home to the Arctic tundra biome, a 5.1 million km^2 region characterized by low-growing, treeless vegetation (Raynolds et al. 2019). The tundra biome forms a belt of cold-adapted vegetation atop the globe, bordered by the Arctic Ocean to the north and the boreal forest "treeline" to the south. Arctic tundra ecosystems are experiencing profound changes as the vegetation, soils, and underlying permafrost respond to rapidly warming air temperatures and the precipitous decline of sea ice on the neighboring Arctic Ocean (Bhatt et al. 2021; sections 5b,e,h). In the late 1990s, Earth-observing satellites began to detect a sharp increase in the productivity of tundra vegetation, a phenomenon known today as "the greening of the Arctic." Arctic greening is dynamically linked with Earth's changing climate, permafrost, seasonal snow, and sea-ice cover.

Global vegetation has been consistently monitored from space since 1982 by the Advanced Very High Resolution Radiometer (AVHRR), a series of sensors that has entered its fifth decade of operation onboard a succession of polar-orbiting satellites. In 2000, the Moderate Resolution Imaging Spectroradiometer (MODIS) sensor became operational and provides observations with higher spatial resolution and improved calibration. AVHRR and MODIS data are used to monitor

vegetation greenness via the Normalized Difference Vegetation Index (NDVI), a spectral metric that exploits the unique way in which green vegetation absorbs and reflects visible and infrared light. The long-term AVHRR NDVI dataset analyzed here is the Global Inventory Modeling and Mapping Studies 3g V1.2 dataset (GIMMS-3g+) with a spatial resolution of about 8 km (Pinzon and Tucker 2014); at the time of writing, processed data were not available for the 2022 growing season, so the GIMMS-3g+ time series covers the period 1982–2021. For MODIS, we computed trends for the period 2000–22 at a higher spatial resolution of 500 m, combining 16-day NDVI products from the *Terra* (Didan 2021a) and *Aqua* (Didan 2021b) satellites, referred to as MCD13A1. All data were masked to include only ice-free land within the extent of the Circumpolar Arctic Vegetation Map (Raynolds et al. 2019). MODIS data were further masked to exclude permanent waterbodies based on the 2015 MODIS *Terra* Land Water Mask (MOD44W, version 6). We summarize the GIMMS-3g+ and MODIS records for the annual maximum NDVI (MaxNDVI), the peak greenness value which is typically observed during July or August.

Both AVHRR and MODIS records indicate that MaxNDVI has increased across most of the Arctic tundra biome since 1982 and 2000, respectively (Figs. 5.28a,b), and show virtually identical trends for the period of overlap (2000–21; Fig. 5.29). In North America, both records indicate strong greening on Alaska's North Slope and across continental Canada. In Eurasia, strong greening has occurred in Chukotka and the Laptev Sea region, but greenness has declined in parts of the Taymyr Peninsula and East Siberian Sea regions. Regional contrasts in greenness trends highlight the complexity of Arctic change and the interactions that connect tundra ecosystems with climate, sea ice, permafrost, seasonal snow, soil composition and moisture, disturbance processes, wildlife, and human activities (Heijmans et al. 2022; Zona et al. 2023). The neighboring boreal forest biome (Figs. 5.28a,b), which occupies extensive portions of northern Eurasia and North America, has also emerged as a "hotspot" of global environmental change and exhibits interspersed greening and "browning" (i.e., productivity decreases) that are also linked to interactions among climate change, wildfire, human land-use, and other factors (Berner and Goetz 2022; Jorgenson et al. 2022).

In 2021—the most recent year with observations from both AVHRR and MODIS—circumpolar mean MaxNDVI for tundra regions declined from the record-high values set in 2020 for both satellite records. AVHRR-observed MaxNDVI declined 8.3% from 2020; nonetheless, the

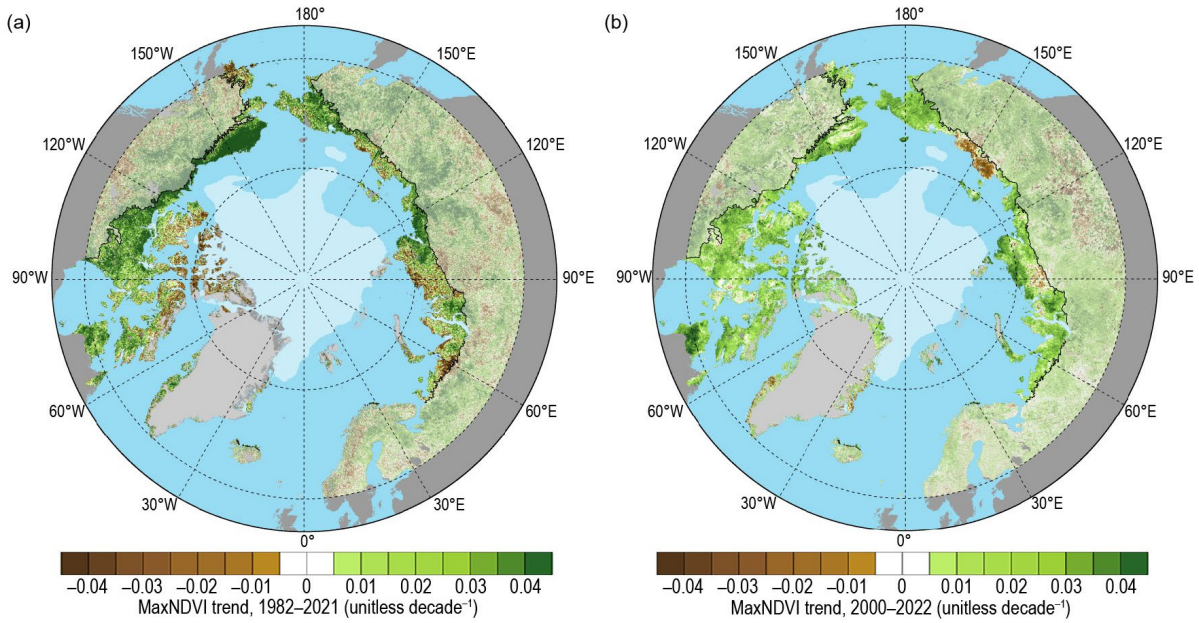

Fig. 5.28. Magnitude of Maximum Normalized Difference Vegetation Index (MaxNDVI) increases ("greening") and decreases ("browning") calculated as the change decade^{-1} via ordinary least squares regression for Arctic tundra (solid colors) and boreal forest north of 60° latitude (muted colors) during (a) 1982–2021 based on the AVHRR GIMMS 3-g+ dataset, and (b) 2000–22 based on the MODIS MCD13A1 dataset. The circumpolar treeline is indicated by a black line, and the 2022 minimum sea-ice extent is indicated by light shading in each panel.

2021 value still exceeded the 1991–2020 mean and was the 15th-highest value recorded in the full record (Fig. 5.29). Notably, the six highest circumpolar average MaxNDVI values in the long-term AVHRR record (1982–2021) have all been recorded in the last 10 years. The 2020 to 2021 decline in MaxNDVI was less pronounced for MODIS (2.7%), and the 2021 value was the second-highest value in the 22-year record for that sensor.

In 2022, the circumpolar MODIS-observed MaxNDVI value declined 0.9% from the previous year, but nonetheless represented the fourth-highest value in the 23-year MODIS record and continued a sequence of exceptionally high values that began in 2020 (Fig. 5.30). Tundra greenness was relatively high in the Canadian Arctic Archipelago, northern Quebec, and northwestern Siberia, but was strikingly low in northeastern Siberia, which experienced unusually persistent summer sea ice and northerly winds in summer 2022 (Fig. 5.30). The overall trend in MODIS-observed circumpolar MaxNDVI is strongly positive, and circumpolar values have exceeded the 23-year mean in 11 of the last 13 growing seasons (Fig. 5.29).

What are the drivers that underlie tundra greening and browning trends, and what types of change might an observer see on the ground? Increases in the abundance, distribution, and height of Arctic shrubs are a major driver of Arctic greening and have important impacts on biodiversity, surface energy balance, permafrost temperatures, and biogeochemical cycling (Mekonnen et al. 2021; Macander et al. 2022), with the potential to serve as a positive feedback to climatic warming (Pearson et al. 2013). Although satellite records provide unequivocal evidence of widespread Arctic greening, there is substantial regional variability in trends. For example, tundra near the East Siberian Sea exhibits widespread browning, which is likely due in part to increased surface water triggered by permafrost thaw, flooding, and recent climate extremes (Magnússon 2021). In 2022, several regions experienced widespread disturbance and extreme weather which can trigger abrupt declines in greenness (see Sidebar 5.1). For example, western Alaska's Yukon-Kuskokwim Delta

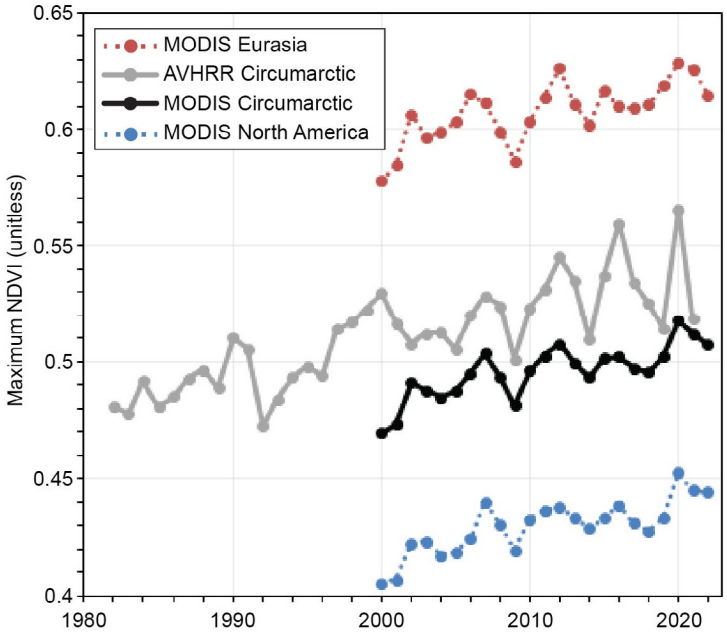

Fig. 5.29. Time series of Maximum Normalized Difference Vegetation Index (MaxNDVI) from the MODIS MCD13A1 (2000–22) dataset for the Eurasian Arctic (dark red), North American Arctic (blue), and the circumpolar Arctic (black), and from the long-term AVHRR GIMMS-3g+ dataset (1982–2021) for the circumpolar Arctic (gray).

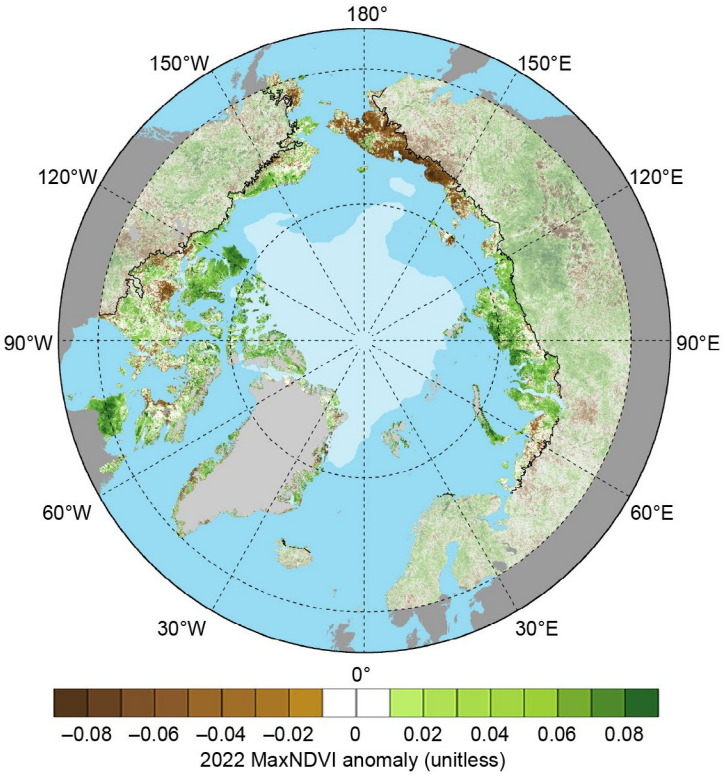

Fig. 5.30. Circumpolar Maximum Normalized Difference Vegetation Index (MaxNDVI) anomalies for the 2022 growing season relative to mean values (2000–22) for Arctic tundra (bright colors) and boreal forest north of 60° latitude (muted colors) from the MODIS MCD13A1 dataset. The circumpolar tree line is indicated by a black line, and the 2022 minimum sea-ice extent is indicated by light shading.

experienced extensive wildfires, continuing a series of years with burned areas far exceeding normal historical conditions. While warming is likely to continue to drive Arctic greening, increased disturbance, extreme events, and other causes of browning are also increasing in frequency (Christensen et al. 2021). Understanding the drivers and regional variability of complex Arctic greening trends continues to be a subject of multi-disciplinary scientific research (Myers-Smith et al. 2020; Rogers et al. 2022; Yang et al. 2022).

k. Ozone and UV radiation

—G. H. Bernhard, V. E. Fioletov, J.-U. Grooß, I. Ialongo, B. Johnsen, K. Lakkala, G. L. Manney, R. Müller, and T. Svendby

Past emissions of manufactured chlorine-containing substances such as chlorofluorocarbons (CFCs) have caused substantial chemical depletion of stratospheric ozone (WMO 2022). The resulting ozone loss led to increases of ultraviolet (UV) radiation at Earth's surface with adverse effects on human health and the environment (Barnes et al. 2019; EEAP 2023). The chemical destruction of polar ozone occurs within a cold stratospheric cyclone known as the polar vortex, which forms over the North Pole every year during winter (WMO 2022). The 2022 polar vortex was somewhat colder than usual; between late January and March 2022, minimum temperatures in the vortex near 16 km–20 km altitude were about 1 st. dev. below the 2005–21 average.

1. OZONE

Chemical processes that drive ozone depletion in the polar stratosphere are initiated at temperatures below about 195 K (–78°C) at altitudes of approximately 15 km–25 km. These low temperatures allow polar stratospheric clouds (PSCs) to occur. These clouds act as a catalyst to transform inactive forms of chlorine-containing substances into active, ozone-destroying chlorine species such as chlorine monoxide (ClO).

According to *Aura* Microwave Limb Sounder (MLS; 2005–present) observations (Waters et al. 2006), temperatures dropped low enough for PSC occurrence in late November 2021. Activation of chlorine started in early December 2021. ClO concentrations near ~16-km altitude (Fig. 5.31a) were near average (2004/05–2020/21) until early February 2022, were about 1 std. dev. above average from then until mid-March 2022, and returned to near-average values thereafter.

In 2021/22, the change of ozone concentrations inside the vortex near 16-km altitude (Fig. 5.31b) was consistent with the evolution of ClO (Fig. 5.31a). Ozone concentrations were near the mean of MLS measurements until mid-February 2022 and started to decrease after chemical depletion commenced. From late February through March 2022, ozone dropped more rapidly than the mean, indicating greater ozone destruction than typical, consistent with above-average ClO concentrations during that period. While there was more chemical destruction of ozone in late February and March 2022 compared to the mean (Fig. 5.31b), the ozone loss in 2022 was much less than in 2011 (e.g., Manney et al. 2011) or 2020 (e.g., Lawrence et al. 2020; Manney et al. 2020),

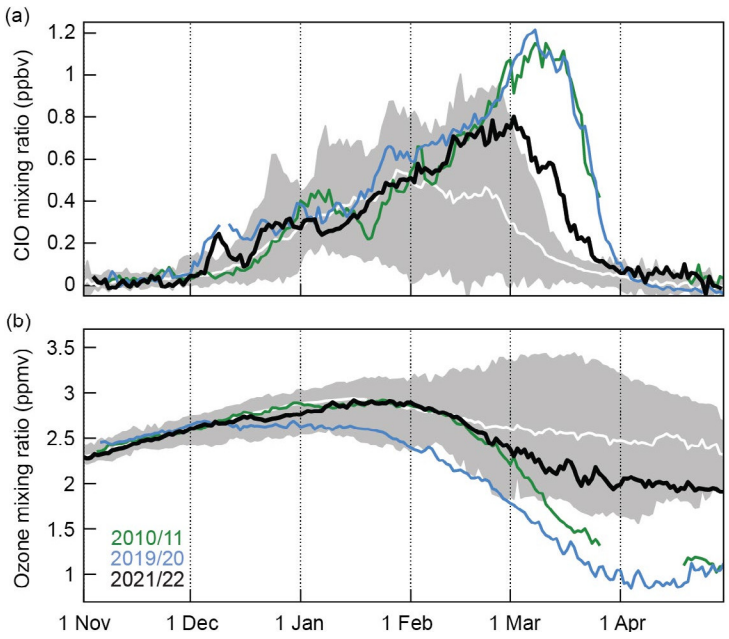

Fig. 5.31. Average (a) chlorine monoxide (ClO) and (b) ozone concentrations (expressed as mixing ratio in ppbv and ppmv, respectively) measured by MLS at an altitude of ~16 km for the area bounded by the Arctic stratospheric polar vortex. Data from 2010/11 (green), 2019/20 (blue), and 2021/22 (black) are compared with the average (solid white) and minimum/maximum range (gray shading) from 2004/05 to 2020/21, excluding the highlighted years. There is a gap in spring 2011 data due to an MLS instrument anomaly.

the years with the lowest ozone values in the MLS record (Fig. 5.31b) and the strongest and most persistent stratospheric polar vortices on record. These large year-to-year variations in Arctic ozone concentrations are mostly driven by differences in meteorological conditions and are expected to continue for as long as concentrations of human-made chlorine-containing substances remain elevated in the stratosphere (WMO 2022). In 2022, ozone concentrations in the lower stratosphere were less than 1 std. dev. below the mean for 2004/05–2020/21, but were near the lowest values of past observations at the end of April when the two extreme years of 2010/11 and 2019/20 are excluded. Compared to ozone concentrations at 16 km, ozone loss was near-average above 18 km but somewhat greater than average near 14 km–15 km.

Below-average ozone concentrations observed in the lower stratosphere after mid-February 2022 (Fig. 5.31b) contributed to below-average total ozone columns (TOC; i.e., ozone amounts integrated from Earth's surface to the top of the atmosphere) in February and March 2022. Figure 5.32 illustrates the variation in TOC between 1979 and 2022 for March by showing the minimum of the daily mean TOC within an area that encloses the polar vortex and is surrounded by the 63°N contour of "equivalent latitude" (Butchart and Remsberg 1986). March was selected because it has historically been the month with the largest potential for chemical ozone depletion in the Arctic (WMO 2022). In March 2022, the minimum Arctic daily TOC was 9.5% (36 Dobson units; DU) below the average TOC since the start of satellite observations in 1979 and 7.4% (27 DU) below the average of 366 DU for the period of measurements (2005–present) by MLS and the Ozone Monitoring Instrument (OMI). TOC values in April 2022 (and later months) were near-average despite the continuation of below-average ozone concentrations in the lower stratosphere of the polar vortex (Fig. 5.31b). This apparent discrepancy is due to the smaller contribution of the vortex to the area enclosed by the 63°N contour in April compared to March. Decreases in TOC observed between 1979 and ~1996 (Fig. 5.32) did not continue because of the phase-out of ozone-depleting substances prompted by the implementation of the Montreal Protocol and its amendments (WMO 2022).

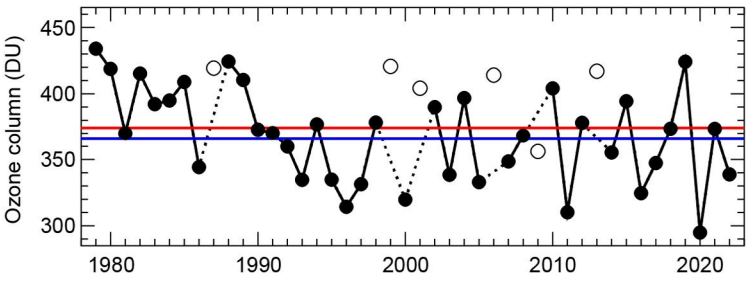

Fig. 5.32. Minimum of the daily average total ozone column (Dobson units, DU) for Mar poleward of 63°N equivalent latitude (Butchart and Remsberg 1986). Open circles represent years in which the polar vortex was not well-defined in Mar, resulting in relatively high values owing to mixing with lower-latitude air masses and a lack of significant chemical ozone depletion. Red and blue lines indicate the average total ozone column for 1979–2021 and 2005–21, respectively. Ozone data for 1979–2019 are based on the combined NIWA-BS total column ozone database version 3.5.1 (Bodeker and Kremser 2021). Ozone data for 2020–22 are from OMI. Adapted from Müller et al. (2008) and WMO (2022), and updated using ERA5 reanalysis data (Hersbach et al. 2020) to determine equivalent latitude.

Spatial deviations of monthly average TOCs from past (2005–21) averages were estimated from OMI measurements. In March 2022 (Fig. 5.33a), Arctic TOC anomalies varied between –20% and +10% but stayed within 2 std. dev. of past observations, with the exception of a small area in northern Siberia. In April 2022 (Fig. 5.33b), TOC anomalies varied to within ±10% and remained within 2 std. dev. Ozone anomalies between May and October 2022 were unremarkable.

2. ULTRAVIOLET RADIATION

Ultraviolet radiation is quantified with the UV Index (UVI), which measures the intensity of UV radiation in terms of causing erythema (sunburn) in human skin. The UVI depends mostly on the sun angle, TOC, clouds, aerosols, and surface albedo (EEAP 2023). In the Arctic, the UVI scale ranges from 0 to about 7, with UVI values <3 north of 80°N. (For comparison, the summertime UVI at midlatitudes may reach 12 [Bernhard et al. 2022]).

Figures 5.33c,d quantify spatial differences in monthly average noontime UVIs from past (2005–21) averages based on measurements by OMI. UVI anomalies in March 2022 (Fig. 5.33c) varied between –35% and +48% and exceeded 2 std. dev. of past observations over Poland, the

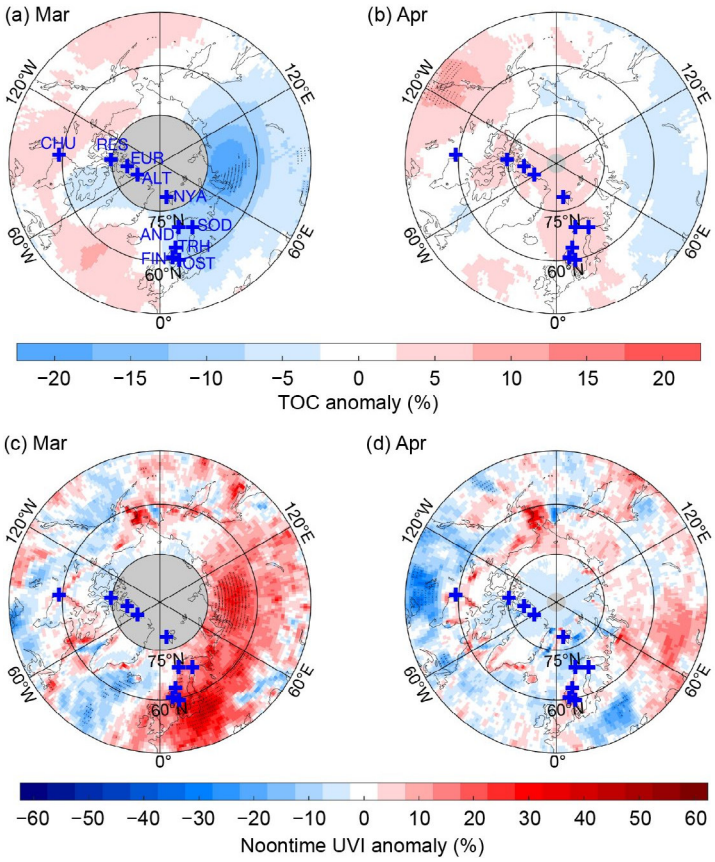

Fig. 5.33. Monthly mean anomaly maps of (a),(b) total ozone column (TOC; %) and (c),(d) noontime UV Index (UVI; %) for Mar and Apr 2022 relative to 2005–21 means. Stippling indicates pixels where anomalies exceed 2 st. dev. Gray-shaded areas centered at the North Pole indicate latitudes where no OMI data are available because of polar darkness. Locations of ground stations are indicated by blue crosses in every map, with labels added to the first map. Maps are based on the OMTO3 Level 3 total ozone product (Bhartia and Wellemeyer 2002). Site acronyms are provided in Table 5.3.

Baltic Sea, Lithuania, and northern Siberia. The larger variability compared to TOC (Fig. 5.33a) can be explained by the added effect from clouds. UVIs in April 2022 (Fig. 5.33d) remained within 2 std. dev. While UVI anomalies assessed with OMI data provide complete spatial coverage, they can sometimes indicate spurious anomalies of up to 60% (Bernhard et al. 2015) when the surface reflectivity (albedo) assumed in the retrieval algorithm (Tanskanen et al. 2003) deviates from the actual albedo. Anomalies for 2022 derived from OMI data agree with most ground-based measurements at 10 Arctic and sub-Arctic sites within ±14% (Table 5.3). Exceptions are Andøya in March (OMI anomaly +9%; ground-based anomaly –10%) and Trondheim in April (OMI anomaly +1%; ground-based anomaly +16%). The differences are caused by local cloud effects at these coastal sites not captured by OMI.

Table 5.3. Monthly mean anomalies (%) of the noontime UV Index (UVI) for Mar and Apr 2022 relative to 2005–21 means calculated from OMI and ground-based data. Site locations are shown in Fig. 5.33.

Site name (acronym)	Latitude	OMI UVI anomaly (March)	ground-based UVI anomaly (March)	OMI UVI anomaly (April)	ground-based UVI anomaly (April)
Alert (ALT)	83°	NA	–1%	–5%	–6%
Eureka (EUR)	80°	NA	5%	–3%	11%
Ny-Ålesund (NYA)	79°	NA	–1%	8%	1%
Resolute (RES)	75°	NA	2%	–2%	8%
Andøya (AND)	69°	9%	–10%	–7%	–4%
Sodankylä (SOD)	67°	16%	10%	1%	–2%
Trondheim (TRH)	63°	11%	6%	1%	16%
Finse (FIN)	61°	21%	8%	13%	9%
Østerås (OST)	60°	24%	13%	7%	6%
Churchill (CHU)	59°	2%	NA	–12%	NA

Sidebar 5.2: Alaska seabird die-offs and the changing Arctic marine ecosystem

—R. KALER, G. SHEFFIELD, S. BACKENSTO, J. LINDSEY, T. JONES, J. K. PARRISH, AND B. AHMASUK

Prior to 2015, seabird die-offs in Alaska were infrequent, typically occurred in mid-winter, and were associated with epizootic disease events or elevated ocean temperatures due to large-scale climate variability, such as El Niño (Bodenstein et al. 2015; Jones et al. 2019). From 2017 through 2022 (Fig. SB5.3), seabird die-offs occurred annually, and observations suggest that die-offs stem from multiple ecosystem changes associated with abnormally high ocean temperatures, including zooplankton and forage fish quantity and quality, increased foraging competition, or exposure to harmful algal bloom biotoxins. The specific cause of recent seabird die-offs in Alaska remains largely unknown but are likely linked to warmer ocean conditions and reductions to sea-ice extent and duration as Arctic marine food webs are supported by ice-associated algae in spring and phytoplankton in summer and energy contributions vary with community composition and nutritional quality (Stabeno et al. 2019; Koch et al. 2023). In addition to die-off events, observations at northern seabird breeding colonies indicate lack of breeding attempts or late and unsuccessful breeding in 2017 through 2019 and may be a result of a lack of food or unfavorable foraging conditions brought on by elevated ocean water temperatures (Romano et al. 2020; Will et al. 2020).

Seabirds are often considered marine ecosystem sentinels, as changes to seabird populations and diets reflect changes in the marine resources they depend upon (Cairns 1988). Planktivorous auklets (*Aethia* spp.) consume Euphausiids (krill), which are high-value prey but only locally and seasonally available, and copepods—a group of small crustaceans that vary in size and energy value depending on ocean temperatures. Piscivorous murres (*Uria* spp.), puffins (*Puffinus* spp.), and kittiwakes (*Rissa* spp.) prey on forage fish such as sand lance (*Ammodytes hexapterus*) and capelin (*Mallotus villosus*). In recent years, the numbers of sand lance and capelin have declined while the numbers of lower-quality, prey-like juvenile walleye pollock (*Gadus chalcogrammus*) and Pacific cod (*Gadus macrocephalus*) have increased in the northern Bering and southern Chukchi Seas (Duffy-Anderson et al. 2019).

During 2017–21, apparent emaciation was the most significant factor contributing to death, based on a combination of field reports, laboratory assessments, and necropsies (Table SB5.1; Bodenstein et al. 2022; US Geological Survey 2022). Researchers continue to evaluate possible contributing factors, including highly pathogenic avian influenza (HPAI). Seabird carcass collection was limited in 2022 due to potential human health concerns of HPAI transmission.

Table SB5.1. Summary of Bering and Chukchi Seas seabird necropsies, 2017–21. More than 14,000 dead seabirds were reported and a total of 117 carcasses were examined. Ninety-two cases had emaciation identified as the cause of death (COD), 7 cases where COD was undetermined, and 17 cases where COD was determined as "other", which included predation, trauma, encephalitis, peritonitis, and bacterial infection. Low pathogenic avian influenza (n=4; different from H5 or H7 highly pathogenic avian influenza strains which are highly infectious to poultry farms) and saxitoxin (n=15) were also detected; however, the virus and biotoxin were not determined to be the COD, except for one case in 2020 where saxitoxin toxicosis was suspected. Data are summarized from Bodenstein et al. (2022).

Necropsy data point	2017	2018	2019	2020	2021	Total
Total reported	>1600	>1200	>9000	>330	>2200	>14,330
Total examined	19	25	39	20	14	117
Reported cause of death — Emaciation	17	19	31	13	12	92
Reported cause of death — Undetermined	0	3	2	1	1	7
Reported cause of death — Other	2	3	6	6	1	18
Avian influenza detected	0	2	0	1	1	4
Saxitoxin detected	11	BDL[1]	3	1[2]	BDL[1]	15

[1] BDL - below detection limits for the laboratory test used.

[2] Saxitoxin toxicosis was also suspected to be the cause of death.

Fortunately, seabirds nesting in dense colonies (e.g., murres, kittiwakes) appeared to be unaffected in 2017–22.

Harmful algal bloom biotoxins have been detected in seabird tissues in the region. Most notably, saxitoxin, which is associated with paralytic shellfish poisoning, was detected in the majority of northern fulmar (*Fulmarus glacialis*) carcasses collected in 2017. While direct neurotoxic effects from saxitoxin could not be confirmed and starvation appeared to be the proximate cause of death, exposure to saxitoxin could have been a contributing factor (Van Hemert et al. 2021). Little is known about the occurrence of these biotoxins or their impacts on wild seabirds; USGS Alaska Science Center researchers continue investigations (M. Smith, US Geological Survey 2022, pers. comm.).

Beached seabird carcasses continue to be reported over a wide geographic range throughout summer and autumn on an annual basis (Fig. SB5.4). Reported counts have been considerably lower in some recent years (e.g., 2020 and 2022).

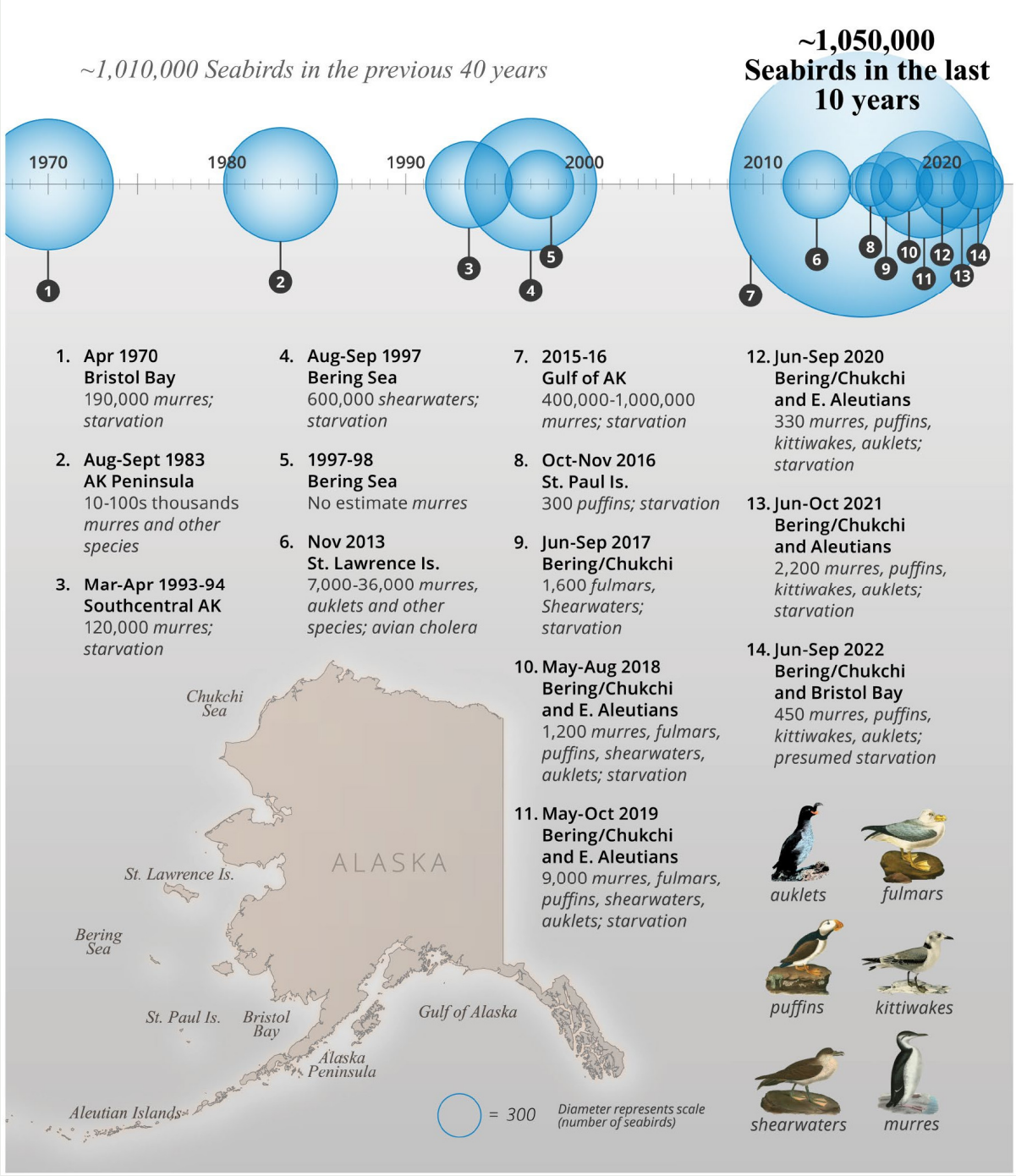

Fig. SB5.4 Alaska seabird die-offs, 1970 to present. Since 2015, mass die-offs have annually occurred in the northern Bering and southern Chukchi sea region. Species primarily affected include murres, puffins, auklets, shearwaters, fulmars, and kittiwakes.

However, due to the expansive and remote nature of Alaska's coastline, much bird mortality goes unreported. Even when bird carcasses are found, reported counts represent a small fraction of the total as many more are lost either due to sinking or scavenging before they can be documented.

The period of seabird die-offs and reduced reproductive success co-occurred with the northward expansion of gadid fishes, such as walleye pollock and Pacific cod (Duffy-Anderson et al. 2019). This may have caused increased competition for forage resources (Piatt et al. 2020) as gadids and piscivorous seabirds feed on much of the same prey. This shift was also layered onto a reduction in the availability of high-quality forage fish (sand lance, capelin) and an increase in lower-quality prey, such as juvenile gadids, in the northern Bering and southern Chukchi Seas in recent years (Duffy-Anderson et at. 2019). Additional work is needed to better understand the links between prey availability and the health and productivity of local seabird populations.

Wildlife mortality events are a public health concern for coastal communities that rely on ocean resources for their nutritional, cultural, and economic well-being. Seabirds and their eggs are important subsistence foods for remote Indigenous communities in rural Alaska. Members of subsistence-focused communities in the northern Bering and southern Chukchi Sea region are frustrated by the lack of timely answers regarding the cause of seabird die-off events and whether birds and eggs are safe to consume. Some communities have requested assistance to document these die-offs and collect samples for testing. The past three years have been especially challenging due to the COVID-19 pandemic, which limited abilities to conduct necropsies on carcasses to determine causes of death, as well as due to increased concerns regarding HPAI in 2022.

With increasing ocean temperatures and decreasing sea ice, the next decade will be critical for determining how marine mammals, marine birds, and human communities adapt to a fast-changing environment in northern Alaska.

Acknowledgments

The editors wish to thank several anonymous reviewers for their efforts. Their careful read and thoughtful input improved each of the sections and, importantly, led to better coherency across the chapter.

a. Overview

Matthew Druckenmiller and Twila Moon appreciate support from NOAA's Arctic Research Office. Rick Thoman appreciates support from NOAA's Climate Program Office.

c. Precipitation

Rune Graversen, Brian Brettschneider, and Rick Thoman contributed information used in this essay.

d. Sea surface temperature

Mary Louise Timmermans acknowledges support from the National Science Foundation Office of Polar Programs, and the Office of Naval Research. Zachary Labe acknowledges support under award NA18OAR4320123 from the National Oceanic and Atmospheric Administration, U.S. Department of Commerce.

h. Rivers

James McClelland and coauthors acknowledge NSF support for the Arctic Great Rivers Observatory (NSF 1913888, 1914081, 1914215, 1913962, 2230812). Shiklomanov and Tretiakov also acknowledge support from the Russian Foundation for Basic Research (grants 18-05-60192 and 18-05-60240). Discharge data for the Mackenzie River are courtesy of Environment Canada.

k. Ozone and UV radiation

Germar Bernhard and coauthors acknowledge the support of Biospherical Instruments, San Diego; the Research Council of Norway through its Centres of Excellence funding scheme, project number 223268/F50; the Academy of Finland for supporting UV measurements through the FARPOCC, SAARA, and CHAMPS (grant no. 329225) projects; the European Space Agency for supporting the DACES project; the Norwegian Environment Agency for funding UV measurements at Andøya and Ny-Ålesund; and the European Union for supporting e-shape. The authors also would like to thank Bodeker Scientific, funded by the New Zealand Deep South National Science Challenge, for providing the combined NIWA-BS total column ozone database; the Microwave Limb Sounder team at NASA's Jet Propulsion Laboratory for data-processing and analysis support; the European Centre for medium-range weather forecasts for providing reanalysis data; and Juha M. Karhu, Tomi Karppinen, and Markku Ahponen from the Finnish Meteorological Institute for operating the Brewer UV spectroradiometer at Sodankylä.

Appendix 1: Chapter 5 – Acronyms

AA	Arctic amplification
ALT	active layer thickness
AMJ	April–May
AVHRR	Advanced Very High Resolution Radiometer
BDL	below detection limits
CCI	Climate Change Initiative
CDD	consecutive dry days
ClO	chlorine monoxide
COD	cause of death
CWD	consecutive wet days
DU	Dobson Units
ERA5	European Centre for Medium-Range Weather Forecasts Reanalysis version 5
ERA-Interim	European Centre for Medium-Range Weather Forecasts Reanalysis Interim
ESA	European Space Agency
GEUS	Geological Survey of Denmark and Greenland
GIMMS-3g+	Global Inventory Modeling and Mapping Studies 3g V1.2 dataset
GISTEMP v4	Goddard Institute for Space Studies Surface Temperature analysis version 4
GPCC	Global Precipitation Climatology Centre
GRACE-FO	Gravity Recovery and Climate Experiment Follow-on
GrIS	Greenland Ice Sheet
HPAI	highly pathogenic avian influenza
ICESat-2	Ice, Cloud and land Elevation Satellite-2
IMS	Ice Mapping System
IPCC	Intergovernmental Panel on Climate Change
JAS	July–September
JFM	January–March
KC	KC-07
KL	Kapp Linne 1
KPC	Kronprins Christians Land
MaxNDVI	Maximum Normalized Difference Vegetation Index
MERRA-2	Modern-Era Retrospective Analysis for Research and Applications version 2
MLS	Microwave Limb Sounder
MOD44W	MODIS *Terra* Land Water Mask
MODIS	Moderate Resolution Imaging Spectroradiometer
NDVI	Normalized Difference Vegetation Index
NOAA	National Oceanic and Atmospheric Administration
OISST	Optimum Interpolation SST
OMI	Ozone Monitoring Instrument
OND	October–December
PROMICE	Programme for Monitoring of the Greenland Ice Sheet
PSC	polar stratospheric clouds
QAS	Qassimuit
Rx1	one-day precipitation
Rx5	five-day precipitation
SCD	snow-cover duration
SCE	snow-cover extent
SLP	sea-level pressure
SMB	surface mass balance
SMOS	Soil Moisture and Ocean Salinity

SSMIS	Special Sensor Microwave Imager/Sounder
SST	sea-surface temperature
SWE	snow water equivalent
TOC	total ozone column
UV	ultraviolet
UVI	UV Index

References

Abramov, A., and Coauthors, 2021: Two decades of active layer thickness monitoring in northeastern Asia. *Polar Geogr.*, **44**, 186–202, https://doi.org/10.1080/1088937X.2019.1648581.

Alaska Division of Forestry, 2022: Wildfires burn more than 3 million acres in Alaska. https://akfireinfo.com/2022/07/21/wildfires-burn-more-than-3-million-acres-in-alaska/.

Barnes, P. W., and Coauthors, 2019: Ozone depletion, ultraviolet radiation, climate change and prospects for a sustainable future. *Nat. Sustainability*, **2**, 569–579, https://doi.org/10.1038/s41893-019-0314-2.

Becker, A., P. Finger, A. Meyer-Christoffer, B. Rudolf, K. Schamm, U. Schneider, and M. Ziese, 2013: A description of the global land-surface precipitation data products of the Global Precipitation Climatology Centre with sample applications including centennial (trend) analysis from 1901–present. *Earth Syst. Sci. Data*, **5**, 71–99, https://doi.org/10.5194/essd-5-71-2013.

Benestad, R. E., and Coauthors, 2022: Global hydro-climatological indicators and changes in the global hydrological cycle and rainfall patterns. *PLOS Climate*, **1**, e0000045, https://doi.org/10.1371/journal.pclm.0000045.

Berner, L. T., and S. J. Goetz, 2022: Satellite observations document trends consistent with a boreal forest biome shift. *Global Change Biol.*, **28**, 3275–3292, https://doi.org/10.1111/gcb.16121.

Bernhard, G., and Coauthors, 2015: Comparison of OMI UV observations with ground-based measurements at high northern latitudes. *Atmos. Chem. Phys.*, **15**, 7391–7412, https://doi.org/10.5194/acp-15-7391-2015.

—— , R. L. McKenzie, K. Lantz, and S. Stierle, 2022: Updated analysis of data from Palmer Station, Antarctica (64°S), and San Diego, California (32°N), confirms large effect of the Antarctic ozone hole on UV radiation. *Photochem. Photobiol. Sci.*, **21**, 373–384, https://doi.org/10.1007/s43630-022-00178-3.

Bhartia, P. K., and C. W. Wellemeyer, 2002: TOMS-V8 total O3 algorithm. OMI Algorithm Theoretical Basis Doc. Volume II, NASA Goddard Space Flight Center Tech. Doc. ATBD-OMI-02, 15–31, https://eospso.gsfc.nasa.gov/sites/default/files/atbd/ATBD-OMI-02.pdf.

Bhatt, U. S., and Coauthors, 2021: Climate drivers of Arctic tundra variability and change using an indicators framework. *Environ. Res. Lett.*, **16**, 055019, https://doi.org/10.1088/1748-9326/abe676.

Blanchard-Wrigglesworth, E., M. Webster, L. Boisvert, C. Parker, and C. Horvat, 2022: Record Arctic cyclone of January 2022: Characteristics, impacts, and predictability. *J. Geophys. Res. Atmos.*, **127**, e2022JD037161, https://doi.org/10.1029/2022JD037161.

Bodeker, G. E., and S. Kremser, 2021: Indicators of Antarctic ozone depletion: 1979 to 2019. *Atmos. Chem. Phys.*, **21**, 5289–5300, https://doi.org/10.5194/acp-21-5289-2021.

Bodenstein, B., K. Beckman, G. Sheffield, K. Kuletz, C. Van Hemert, B. Berlowski, and V. Shearn-Bochsler, 2015: Avian cholera causes marine bird mortality in the Bering Sea of Alaska. *J. Wildl. Dis.*, **51**, 934–937, https://doi.org/10.7589/2014-12-273.

—— , R. J. Dusek, M. M. Smith, C. R. Van Hemert, and R. S. A. Kaler, 2022: USGS National Wildlife Health Center necropsy results to determine cause of illness/death for seabirds collected in Alaska from January 1, 2017 through December 31, 2021. U.S. Geological Survey, accessed 11 July 2023, https://doi.org/10.5066/P9XHBX75.

Box, J. E., and Coauthors, 2019: Key indicators of Arctic climate change: 1971–2017. *Environ. Res. Lett.*, **14**, 045010, https://doi.org/10.1088/1748-9326/aafc1b.

Brady, M. B., and R. Leichenko, 2020: The impacts of coastal erosion on Alaska's North Slope communities: A co-production assessment of land use damages and risks. *Polar Geogr.*, **43**, 259–279, https://doi.org/10.1080/1088937X.2020.1755907.

Brown, J., O. J. Ferrians Jr., J. A. Heginbottom, and E. S. Melnikov, 1997: Circum-Arctic map of permafrost and ground-ice conditions: Map CP-45. U.S. Geological Survey, 1 pp., https://pubs.er.usgs.gov/publication/cp45.

Brown, R., D. Vikhamar Schuler, O. Bulygina, C. Derksen, K. Luojus, L. Mudryk, L. Wang, and D. Yang, 2017: Arctic terrestrial snow cover. ow, Water, Ice and Permafrost in the Arctic (SWIPA) 2017, Arctic, Monitoring and Assessment Programme, 25–64, www.amap.no/documents/doc/snow-water-ice-and-permafrost-in-the-arctic-swipa-2017/1610.

Brun, E., V. Vionnet, A. Boone, B. Decharme, Y. Peings, R. Valette, F. Karbou, and S. Morin, 2013: Simulation of northern Eurasian local snow depth, mass, and density using a detailed snowpack model and meteorological reanalyses. *J. Hydrometeor.*, **14**, 203–219, https://doi.org/10.1175/JHM-D-12-012.1.

Butchart, N., and E. E. Remsberg, 1986: The area of the stratospheric polar vortex as a diagnostic for tracer transport on an isentropic surface. *J. Atmos. Sci.*, **43**, 1319–1339, https://doi.org/10.1175/1520-0469(1986)0432.0.CO;2.

Cairns, D. K., 1988: Seabirds as indicators of marine food supplies. *Biol. Oceanogr.*, **5**, 261–271.

Christensen, T. R., and Coauthors, 2021: Multiple ecosystem effects of extreme weather events in the Arctic. *Ecosystems*, **24**, 122–136, https://doi.org/10.1007/s10021-020-00507-6.

Chylek, P., C. Folland, J. D. Klett, M. Wang, N. Hengartner, G. Lesins, and M. K. Dubey, 2022: Annual mean Arctic amplification 1970–2020: Observed and simulated by CMIP6 climate models. *Geophys. Res. Lett.*, **49**, e2022GL099371, https://doi.org/10.1029/2022GL099371.

Cohen, J., and Coauthors, 2020: Divergent consensuses on Arctic amplification influence on mid-latitude severe winter weather. *Nat. Climate Change*, **10**, 20–29, https://doi.org/10.1038/s41558-019-0662-y.

—— , L. Agel, M. Barlow, C. I. Garfinkel, and I. White, 2021: Arctic change reduces risk of cold extremes—Response. *Science*, **375**, 729–730, https://doi.org/10.1126/science.abn8954.

Crozier, L. G., B. J. Burke, B. E. Chasco, D. L. Widener, and R. W. Zabel, 2021: Climate change threatens Chinook salmon throughout their life cycle. *Commun. Biol.*, **4**, 222, https://doi.org/10.1038/s42003-021-01734-w.

Davidson, S. C., and Coauthors, 2020: Ecological insights from three decades of animal movement tracking across a changing Arctic. *Science*, **370**, 712–715, https://doi.org/10.1126/science.abb7080.

Didan, K., 2021a: MODIS/terra vegetation indices 16-day L3 global 500m SIN grid V061 [Data set]. NASA EOSDIS Land Processes DAAC, accessed 27 February 2023, https://doi.org/10.5067/MODIS/MOD13A1.061.

—— , 2021b: MODIS/aqua vegetation indices 16-day L3 global 500m SIN Grid V061 [Data set]. NASA EOSDIS Land Processes DAAC, accessed 27 February 2023, https://doi.org/10.5067/MODIS/MYD13A1.061.

Duffy-Anderson, J. T., and Coauthors, 2019: Responses of the northern Bering Sea and southeastern Bering Sea pelagic ecosystems following record-breaking low winter sea ice. *Geophys. Res. Lett.*, **46**, 9833–9842, https://doi.org/10.1029/2019GL083396.

Durocher, M., A. I. Requena, D. H. Burn, and J. Pellerin, 2019: Analysis of trends in annual streamflow to the Arctic Ocean. *Hydrol. Processes*, **33**, 1143–1151, https://doi.org/10.1002/hyp.13392.

EEAP, 2023: Environmental effects of stratospheric ozone depletion, UV radiation, and interactions with climate change. 2022 Assessment Rep., Environmental Effects Assessment Panel, United Nations Environment Programme, 372 pp., https://ozone.unep.org/system/files/documents/EEAP-2022-Assessment-Report-May2023.pdf.

England, M. R., I. Eisenman, N. J. Lutsko, and T. J. W. Wagner, 2021: The recent emergence of Arctic amplification. *Geophys. Res. Lett.*, **48**, e2021GL094086, https://doi.org/10.1029/2021GL094086.

Fetterer, F., K. Knowles, W. N. Meier, M. Savoie, and A. K. Windnagel, 2017: Sea ice index, version 3. National Snow and Ice Data Center, accessed 27 August 2021, https://doi.org/10.7265/N5K072F8.

Frey, K. E., J. C. Comiso, L. W. Cooper, C. Garcia-Eidell, J. M. Grebmeier, and L. V. Stock, 2022: Arctic Ocean primary productivity: The response of marine algae to climate warming and sea ice decline. *Arctic Report Card 2022*, M. L. Druckenmiller, R. L. Thoman, and T. A. Moon, Eds., NOAA Tech. Rep. OAR ARC-22-08, 55–65, https://doi.org/10.25923/0je1-te61.

GMAO, 2015: MERRA-2tavg1_2d_lnd_Nx:2d, 1-hourly, time-averaged, single-level, assimilation, land surface diagnostics V5.12.4. Goddard Earth Sciences Data and Information Services Center (GESDISC), accessed 13 February 2023, https://doi.org/10.5067/RKPHT8KC1Y1T.

Gohari, A., A. J. Shahrood, S. Ghadimi, M. Alborz, E. R. Patro, B. Klöve, and A. T. Haghighi, 2022: A century of variations in extreme flow across Finnish rivers. *Environ. Res. Lett.*, **17**, 124027, https://doi.org/10.1088/1748-9326/aca554.

Heijmans, M. M. P. D., and Coauthors, 2022: Tundra vegetation change and impacts on permafrost. *Nat. Rev. Earth Environ.*, **3**, 68–84, https://doi.org/10.1038/s43017-021-00233-0.

Hersbach, H. B., and Coauthors, 2020: The ERA5 global reanalysis. *Quart. J. Roy. Meteor. Soc.*, **146**, 1999–2049, https://doi.org/10.1002/qj.3803.

Hiyama, T., H. Park, K. Kobayashi, L. Lebedeva, and D. Gustafsson, 2023: Contribution of summer net precipitation to winter river discharge in permafrost zone of the Lena River basin. *J. Hydrol.*, **616**, 128797, https://doi.org/10.1016/j.jhydrol.2022.128797.

Hjort, J., D. Streletskiy, G. Doré, Q. Wu, K. Bjella, and M. Luoto, 2022: Impacts of permafrost degradation on infrastructure. *Nat. Rev. Earth Environ.*, **3**, 24–38, https://doi.org/10.1038/s43017-021-00247-8.

Holmes, R. M., and Coauthors, 2013: Climate change impacts on the hydrology and biogeochemistry of Arctic Rivers. *Climactic Change and Global Warming of Inland Waters: Impacts and Mitigation for Ecosystems and Societies*, C. R. Goldman, M. Kumagai, and R. D. Robarts, Eds., Wiley, 3–26.

Huang, B., C. Liu, V. Banzon, E. Freeman, G. Graham, B. Hankins, T. Smith, and H. Zhang, 2021: Improvements of the Daily Optimum Interpolation Sea Surface Temperature (DOISST) version 2.1. *J. Climate*, **34**, 2923–2939, https://doi.org/10.1175/JCLI-D-20-0166.1.

IPCC, 2021: *Climate Change 2021: The Physical Science Basis*. V. Masson-Delmotte et al., Eds., Cambridge University Press, 2391 pp.

Irrgang, A. M., and Coauthors, 2022: Drivers, dynamics and impacts of changing Arctic coasts. *Nat. Rev. Earth Environ.*, **3**, 39–54, https://doi.org/10.1038/s43017-021-00232-1.

Isaksen, K., J. Lutz, A. M. Sorensen, O. Godoy, L. Ferrighi, S. Eastwood, and S. Aaboe, 2022: Advances in operational permafrost monitoring on Svalbard and in Norway. *Environ. Res. Lett.*, **17**, 095012, https://doi.org/10.1088/1748-9326/ac8e1c.

Ivanova, N., O. M. Johannessen, L. T. Pedersen, and R. T. Tonboe, 2014: Retrieval of Arctic sea ice parameters by satellite passive microwave sensors: A comparison of eleven sea ice concentration algorithms. *IEEE Trans. Geosci. Remote Sens.*, **52**, 7233–7246, https://doi.org/10.1109/TGRS.2014.2310136.

Jones, T., L. Divine, H. Renner, S. Knowles, K. A. Lefebvre, H. K. Burgess, C. Wright, and J. Parrish, 2019: Unusual mortality of Tufted puffins (Fratercula cirrhata) in the eastern Bering Sea. *PLOS ONE*, **14**, e0216532, https://doi.org/10.1371/journal.pone.0216532.

Jorgenson, M. T., D. R. N. Brown, C. A. Hiemstra, H. Genet, B. G. Marcot, R. J. Murphy, and T. A. Douglas, 2022: Drivers of historical and projected changes in diverse boreal ecosystems: Fires, thermokarst, riverine dynamics, and humans. *Environ. Res. Lett.*, **17**, 045016, https://doi.org/10.1088/1748-9326/ac5c0d.

Kaverin, D., and Coauthors, 2021: Long-term active layer monitoring at CALM sites in the Russian European North. *Polar Geogr.*, **44**, 203–216, https://doi.org/10.1080/1088937X.2021.1981476.

Koch, C. W., and Coauthors, 2023: Year-round utilization of sea ice-associated carbon in Arctic ecosystems. *Nat. Commun.*, **14**, 1964, https://doi.org/10.1038/s41467-023-37612-8

Kopec, B., X. Feng, F. A. Michel, and E. Posmentier, 2016: Influence of sea ice on Arctic precipitation. *Proc. Natl. Acad. Sci. USA*, **113**, 46–51, https://doi.org/10.1073/pnas.1504633113.

Kusunoki, S., R. Mizuta, and M. Hosaka, 2015: Future changes in precipitation intensity over the Arctic projected by a global atmospheric model with a 60-km grid size. *Polar Sci.*, **9**, 277–292, https://doi.org/10.1016/j.polar.2015.08.001.

Landy, J. C., and Coauthors, 2022: A year-round satellite sea-ice thickness record from CryoSat-2. *Nature*, **609**, 517–522, https://doi.org/10.1038/s41586-022-05058-5.

Lavergne, T., and Coauthors, 2019: Version 2 of the EUMETSAT OSI SAF and ESA CCI sea-ice concentration climate data records. *Cryosphere*, **13**, 49–78, https://doi.org/10.5194/tc-13-49-2019.

Lawrence, Z. D., J. Perlwitz, A. H. Butler, G. L. Manney, P. A. Newman, S. H. Lee, and E. R. Nash, 2020: The remarkably strong Arctic stratospheric polar vortex of winter 2020: Links to record-breaking Arctic oscillation and ozone loss. *J. Geophys Res. Atmos.*, **125**, e2020JD033271, https://doi.org/10.1029/2020JD033271.

Lenssen, N. J., G. A. Schmidt, J. E. Hansen, M. J. Menne, A. Persin, R. Ruedy, and D. Zyss, 2019: Improvements in the GISTEMP uncertainty model. *J. Geophys. Res. Atmos.*, **124**, 6307–6326, https://doi.org/10.1029/2018JD029522.

Liu, S., and Coauthors, 2022: Mechanisms behind the uneven increases in early, mid- and late winter streamflow across four Arctic river basins. *J. Hydrol.*, **606**, 127425, https://doi.org/10.1016/j.jhydrol.2021.127425.

Luojus, K., and Coauthors, 2022: ESA Snow Climate Change Initiative (Snow_cci): Snow Water Equivalent (SWE) level 3C daily global climate research data package (CRDP) (1979–2020), version 2.0. NERC EDS Centre for Environmental Data Analysis, accessed 8 September 2022, https://doi.org/10.5285/4647cc9ad3c044439d6c643208d3c494.

Macander, M. J., P. R. Nelson, T. W. Nawrocki, G. V. Frost, K. M. Orndahl, E. C. Palm, A. F. Wells, and S. J. Goetz, 2022: Time-series maps reveal widespread change in plant functional type cover across Arctic and boreal Alaska and Yukon. *Environ. Res. Lett.*, **17**, 054042, https://doi.org/10.1088/1748-9326/ac6965.

Magnússon, R. Í., 2021: Shrub decline and expansion of wetland vegetation revealed by very high resolution land cover change detection in the Siberian lowland tundra. *Sci. Total Environ.*, **782**, 146877, https://doi.org/10.1016/j.scitotenv.2021.146877.

Malkova, G., and Coauthors, 2022: Spatial and temporal variability of permafrost in the western part of the Russian Arctic. *Energies*, **15**, 2311, https://doi.org/10.3390/en15072311.

Mallory, C. D., and M. S. Boyce, 2018: Observed and predicted effects of climate change on Arctic caribou and reindeer. *Environ. Rev.*, **26**, 13–25, https://doi.org/10.1139/er-2017-0032.

Mamen, J., H. T. T. Tajet, and K. Tunheim, 2022: Klimatologisk månedsoversikt, June 2022. MET Info 6/2022 (in Norwegian). Meteorologisk Institutt, 23 pp., www.met.no/publikasjoner/met-info/met-info-2022.

Mankoff, K. D., A. Solgaard, W. Colgan, A. P. Ahlstrøm, S. A. Khan, and R. S. Fausto, 2020: Greenland Ice Sheet solid ice discharge from 1986 through March 2020. *Earth Syst. Sci. Data*, **12**, 1367–1383, https://doi.org/10.5194/essd-12-1367-2020.

——, and Coauthors, 2021: Greenland ice sheet mass balance from 1840 through next week. *Earth Syst. Sci. Data*, **13**, 5001–5025, https://doi.org/10.5194/essd-13-5001-2021.

Manney, G. L., and Coauthors, 2011: Unprecedented Arctic ozone loss in 2011. *Nature*, **478**, 469–475, https://doi.org/10.1038/nature10556.

——, and Coauthors, 2020: Record-low Arctic stratospheric ozone in 2020: MLS observations of chemical processes and comparisons with previous extreme winters. *Geophys. Res. Lett.*, **47**, e2020GL089063, https://doi.org/10.1029/2020GL089063.

McClelland, J. W., R. M. Holmes, K. H. Dunton, and R. Macdonald, 2012: The Arctic Ocean estuary. *Estuaries Coasts*, **35**, 353–368, https://doi.org/10.1007/s12237-010-9357-3.

McCrystall, M., J. Stroeve, M. C. Serreze, B. C. Forbes, and J. Screen, 2021: New climate models reveal faster and larger increases in Arctic precipitation than previously projected. *Nat. Commun.*, **12**, 6765, https://doi.org/10.1038/s41467-021-27031-y.

Meier, W. N., F. Fetterer, A. K. Windnagel, and J. S. Stewart, 2021a: NOAA/NSIDC climate data record of passive microwave sea ice concentration, version 4. National Snow and Ice Data Center, accessed 10 September 2022, https://doi.org/10.7265/efmz-2t65.

——, ——, ——, and ——, 2021b: Near-real-time NOAA/NSIDC climate data record of passive microwave sea ice concentration, version 2. National Snow and Ice Data Center, accessed 10 September 2022, https://doi.org/10.7265/tgam-yv28.

Mekonnen, Z. A., and Coauthors, 2021: Arctic tundra shrubification: A review of mechanisms and impacts on ecosystem carbon balance. *Environ. Res. Lett.*, **16**, 053001, https://doi.org/10.1088/1748-9326/abf28b.

Meredith, M., and Coauthors, 2019: Polar regions. *IPCC Special Report on the Ocean and Cryosphere in a Changing Climate*, H.-O. Pörtner et al., Eds., Cambridge University Press, 203–320.

Moore, G. W. K., S. E. L. Howell, M. Brady, X. Xu, and K. McNeil, 2021: Anomalous collapses of Nares Strait ice arches leads to enhanced export of Arctic sea ice. *Nat. Commun.*, **12**, 1, https://doi.org/10.1038/s41467-020-20314-w.

Morlighem, M., and Coauthors, 2017: BedMachine v3: Complete bed topography and ocean bathymetry mapping of Greenland from multi-beam radar sounding combined with mass conservation. *Geophys. Res. Lett.*, **44**, 11 051–11 061, https://doi.org/10.1002/2017GL074954.

Mote, T., 2007: Greenland surface melt trends 1973–2007: Evidence of a large increase in 2007. *Geophys. Res. Lett.*, **34**, L22507, https://doi.org/10.1029/2007GL031976.

Mouginot, J., and Coauthors, 2019: Forty-six years of Greenland Ice Sheet mass balance from 1972 to 2018. *Proc. Natl. Acad. Sci. USA*, **116**, 9239–9244, https://doi.org/10.1073/pnas.1904242116.

Müller, R., J.-U. Grooß, C. Lemmen, D. Heinze, M. Dameris, and G. Bodeker, 2008: Simple measures of ozone depletion in the polar stratosphere. *Atmos. Chem. Phys.*, **8**, 251–264, https://doi.org/10.5194/acp-8-251-2008.

Muñoz Sabater, J., 2019: ERA5-land hourly data from 1981 to present. Copernicus Climate Change Service (C3S) Climate Data Store (CDS), accessed 8 September 2022, https://doi.org/10.24381/cds.e2161bac.

Myers-Smith, I. H., and Coauthors, 2020: Complexity revealed in the greening of the Arctic. *Nat. Climate Change*, **10**, 106–117, https://doi.org/10.1038/s41558-019-0688-1.

Nielsen, D. M., P. Pieper, A. Barkhordarian, P. Overduin, T. Ilyina, V. Brovkin, J. Baehr, and M. Dobrynin, 2022: Increase in Arctic coastal erosion and its sensitivity to warming in the twenty-first century. *Nat. Climate Change.*, **12**, 263–270, https://doi.org/10.1038/s41558-022-01281-0.

NOAA, 2022: The Global Climate during El Niño and La Niña. Accessed 21 May 2023, https://psl.noaa.gov/enso/compare/.

Nyland, K. E., N. I. Shiklomanov, D. A. Streletskiy, F. E. Nelson, A. E. Klene, and A. L. Kholodov, 2021: Long-term Circumpolar Active Layer Monitoring (CALM) program observations in Northern Alaskan tundra. *Polar Geogr.*, **44**, 176–185, https://doi.org/10.1080/1088937X.2021.1988000.

Overland, J. E., 2022: Arctic climate extremes. *Atmosphere*, **13**, 1670, https://doi.org/10.3390/atmos13101670.

Pearson, R. G., S. J. Phillips, M. M. Loranty, P. S. A. Beck, T. Damoulas, S. J. Knight, and S. J. Goetz, 2013: Shifts in Arctic vegetation and associated feedbacks under climate change. *Nat. Climate Change*, **3**, 673–677, https://doi.org/10.1038/nclimate1858.

Peng, G., W. N. Meier, D. J. Scott, and M. H. Savoie, 2013: A long-term and reproducible passive microwave sea ice concentration data record for climate studies and monitoring. *Earth Syst. Sci. Data*, **5**, 311–318, https://doi.org/10.5194/essd-5-311-2013.

Peterson, B. J., R. M. Holmes, J. W. McClelland, C. J. Vorosmarty, R. B. Lammers, A. I. Shiklomanov, I. A. Shiklomanov, and S. Rahmstorf, 2002: Increasing river discharge to the Arctic Ocean. *Science*, **298**, 2171–2173, https://doi.org/10.1126/science.1077445.

Petty, A. A., N. T. Kurtz, R. Kwok, T. Markus, and T. A. Neumann, 2020: Winter Arctic sea ice thickness from ICESat 2 freeboards. *J. Geophys. Res. Oceans*, **125**, e2019JC015764, https://doi.org/10.1029/2019JC015764.

——, ——, ——, ——, and ——, 2021: ICESat-2 L4 monthly gridded sea ice thickness, version 1. NASA National Snow and Ice Data Center Distributed Active Archive Center, accessed 9 September, https://doi.org/10.5067/CV6JEXEE31HF.

—— , N. Keeney, A. Cabaj, P. Kushner, and M. Bagnardi, 2023: Winter Arctic sea ice thickness from ICESat-2: Upgrades to freeboard and snow loading estimates and an assessment of the first three winters of data collection. *Cryosphere*, **17**, 127–156, https://doi.org/10.5194/tc-17-127-2023.

Piatt, J. P., and Coauthors, 2020: Extreme mortality and reproductive failure of common murres resulting from the northeast Pacific marine heatwave of 2014–2016. *PLOS ONE*, **15**, e0226087, https://doi.org/10.1371/journal.pone.0226087.

Pinzon, J., and C. Tucker, 2014: A non-stationary 1981–2012 AVHRR NDVI3g time series. *Remote Sens.*, **6**, 6929–6960, https://doi.org/10.3390/rs6086929.

Previdi, M., K. L. Smith, and L. M. Polvani, 2021: Arctic amplification of climate change: A review of underlying mechanisms. *Environ. Res. Lett.*, **16**, 093003, https://doi.org/10.1088/1748-9326/ac1c29.

Rantanen, M., A. Y. Karpechko, A. Lipponen, K. Nordling, O. Hyvärinen, K. Ruosteenoja, T. Vihma, and A. Laaksonen, 2022: The Arctic has warmed nearly four times faster than the globe since 1979. *Commun. Earth Environ.*, **3**, 168, https://doi.org/10.1038/s43247-022-00498-3.

Rawlins, M. A., and Coauthors, 2010: Analysis of the Arctic system freshwater cycle intensification: Observations and expectations. *J. Climate*, **23**, 5715–5737, https://doi.org/10.1175/2010JCLI3421.1.

Raynolds, M. K., and Coauthors, 2019: A raster version of the Circumpolar Arctic Vegetation Map (CAVM). *Remote Sens. Environ.*, **232**, 111297, https://doi.org/10.1016/j.rse.2019.111297.

Reynolds, R. W., N. A. Rayner, T. M. Smith, D. C. Stokes, and W. Wang, 2002: An improved in situ and satellite SST analysis for climate. *J. Climate*, **15**, 1609–1625, https://doi.org/10.1175/1520-0442(2002)0152.0.CO;2.

—— , T. M. Smith, C. Liu, D. B. Chelton, K. S. Casey, and M. G. Schlax, 2007: Daily high-resolution-blended analyses for sea surface temperature. *J. Climate*, **20**, 5473–5496, https://doi.org/10.1175/2007JCLI1824.1.

Ricker, R., S. Hendricks, L. Kaleschke, X. Tian-Kunze, J. King, and C. Haas, 2017: A weekly Arctic sea-ice thickness data record from merged CryoSat-2 and SMOS satellite data. *Cryosphere*, **11**, 1607–1623, https://doi.org/10.5194/tc-11-1607-2017.

Robinson, D. A., T. W. Estilow, and NOAA CDR Program, 2012: NOAA Climate Data Record (CDR) of Northern Hemisphere (NH) Snow Cover Extent (SCE), version 1 [r01]. NOAA National Centers for Environmental Information, accessed 15 August 2022, https://doi.org/10.7289/V5N014G9.

Rogers, A., S. P. Serbin, and D. A. Way, 2022: Reducing model uncertainty of climate change impacts on high latitude carbon assimilation. *Global Change Biol.*, **28**, 1222–1247, https://doi.org/10.1111/gcb.15958.

Romano, M., H. M. Renner, K. J. Kuletz, J. K. Parrish, T. Jones, H. K. Burgess, D. A. Cushing, and D. Causey, 2020: Die-offs and reproductive failure of murres in the Bering and Chukchi Seas in 2018. *Deep-Sea Res. II*, **181–182**, 104877, https://doi.org/10.1016/j.dsr2.2020.104877.

Romanovsky, V., and Coauthors, 2017: Changing permafrost and its impacts. Snow, Water, Ice and Permafrost in the Arctic (SWIPA) 2017, Arctic, Monitoring and Assessment Programme, 65–102, www.amap.no/documents/doc/snow-water-ice-and-permafrost-in-the-arctic-swipa-2017/1610.

Ryan, J. C., L. C. Smith, D. van As, S. W. Cooley, M. G. Cooper, L. H. Pitcher, and A. Hubbard, 2019: Greenland ice sheet surface melt amplified by snowline migration and bare ice exposure. *Sci. Adv.*, **5**, eaav3738, https://doi.org/10.1126/sciadv.aav3738.

Schneider, U., P. Finger, E. Rustemeier, M. Ziese, and S. Hänsel, 2022: Global precipitation analysis products of the GPCC. DWD, 17 pp., https://opendata.dwd.de/climate_environment/GPCC/PDF/GPCC_intro_products_v2022.pdf.

Schuur, E. A. G., 2020: Permafrost carbon [in "State of the Climate in 2019"]. *Bull. Amer. Meteor. Soc.*, **101** (8), S270–S271, https://doi.org/10.1175/BAMS-D-20-0086.1.

SEARCH, and Coauthors, 2022: Consequences of rapid environmental Arctic change for people. *Arctic Report Card 2022,* M. L. Druckenmiller, R. L. Thoman, and T. A. Moon, Eds., NOAA Tech. Rep. OAR ARC-22-16, 123–129, https://doi.org/10.25923/kgm2-9k50.

Shiklomanov, N. I., D. A. Streletskiy, and F. E. Nelson, 2012: Northern Hemisphere component of the global Circumpolar Active Layer Monitoring (CALM) Program. *Proc. 10th Int. Conf. on Permafrost*, Vol. 1, Salekhard, Russia, Tyumen Oil and Gas University, 377–382.

Shrestha, R. R., K. E. Bennett, D. L. Peters, and D. Yang, 2021: Hydrologic extremes in Arctic rivers and regions: Historical variability and future perspectives. *Arctic Hydrology, Permafrost and Ecosystems*, D. Yang and D. L. Kane, Eds., Springer, 187–218, https://doi.org/10.1007/978-3-030-50930-9_7.

Sillmann, J., V. V. Kharin, F. W. Zwiers, X. Zhang, and D. Bronaugh, 2013: Climate extremes indices in the CMIP5 multimodel ensemble: Part 2. Future climate projections. *J. Geophys. Res. Atmos.*, **118**, 2473–2493, https://doi.org/10.1002/jgrd.50188.

Smith, S. L., and Coauthors, 2022a: Permafrost [in "State of the Climate in 2021"]. *Bull. Amer. Meteor. Soc.*, **103** (8), S286–S290, https://doi.org/10.1175/BAMS-D-22-0082.1.

—— , H. B. O'Neill, K. Isaksen, J. Noetzli, and V. E. Romanovsky, 2022b: The changing thermal state of permafrost. *Nat. Rev. Earth Environ.*, **3**, 10–23, https://doi.org/10.1038/s43017-021-00240-1.

Stabeno, P. J., R. L. Thoman, and K. Wood, 2019: Recent warming in the Bering Sea and its impacts on the ecosystem. *Arctic Report Card 2019*, J. Richter-Menge, M. L. Druckenmiller, and M. Jeffries, Eds., NOAA Tech. Rep., 81–87, https://arctic.noaa.gov/Portals/7/ArcticReportCard/Documents/ArcticReportCard_full_report2019.pdf.

Strand, S. M., H. H. Christiansen, M. Johansson, J. Akerman, and O. Humlum, 2021: Active layer thickening and controls on interannual variability in the Nordic Arctic compared to the circum-Arctic. *Permafrost Periglacial. Processes*, **32**, 47–58, https://doi.org/10.1002/ppp.2088.

Stroh, J. N., G. Panteleev, S. Kirillov, M. Makhotin, and N. Shakhova, 2015: Sea-surface temperature and salinity product comparison against external in situ data in the Arctic Ocean. *J. Geophys. Res. Oceans*, **120**, 7223–7236, https://doi.org/10.1002/2015JC011005.

Tanskanen, A., A. Arola, and J. Kujanpää, 2003: Use of the moving time-window technique to determine surface albedo from the TOMS reflectivity data. *Proc. SPIE*, **4896**, 239–250, https://doi.org/10.1117/12.483407.

Tapley, B. D., and Coauthors, 2019: Contributions of GRACE to understanding climate change. *Nat. Climate Change*, **9**, 358–369, https://doi.org/10.1038/s41558-019-0456-2.

Thoman, R., M. L. Druckenmiller, and T. A. Moon, Eds., 2022: The Arctic [in "State of the Climate in 2021"]. *Bull. Amer. Meteor. Soc.*, **103** (8), S257–S306, https://doi.org/10.1175/BAMS-D-22-0082.1.

Timmermans, M.-L., and Z. Labe, 2022: Sea surface temperature [in "State of the Climate in 2021"]. *Bull. Amer. Meteor. Soc.*, **103** (8), S268–S270, https://doi.org/10.1175/BAMS-D-22-0082.1.

Tretiyakov, M. V., O. V. Muzhdaba, A. A. Piskun, and R. A. Terekhova, 2022: The state of the Roshydromet Hydrological Observation Network in the mouth areas of RFAZ. *Water Resour.*, **49**, 796–807, https://doi.org/10.1134/S0097807822050153.

Tschudi, M., W. N. Meier, and J. S. Stewart, 2019a: Quicklook Arctic weekly EASE-grid sea ice age, version 1 [March, 2021]. NASA National Snow and Ice Data Center Distributed Active Archive Center, accessed 1 September 2021, https://doi.org/10.5067/2XXGZY3DUGNQ.

——, ——, ——, C. Fowler, and J. Maslanik, 2019b: EASE-grid sea ice age, version 4 [March, 1984–2020]. NASA National Snow and Ice Data Center Distributed Active Archive Center, accessed 1 September 2021, https://doi.org/10.5067/UTAV7490FEPB.

U.S. Geological Survey, 2022: Wildlife Health Information Sharing Partnership–Event Reporting System (WHISPers) on-line database. Accessed October 2022, https://whispers.usgs.gov/home.

U.S. National Ice Center, 2008: IMS daily Northern Hemisphere snow and ice analysis at 1 km, 4 km, and 24 km resolutions, version 1. National Snow and Ice Data Center, accessed 13 August 2022, https://doi.org/10.7265/N52R3PMC.

Van Hemert, C., and Coauthors, 2021: Investigation of algal toxins in a multispecies seabird die-off in the Bering and Chukchi seas. *J. Wildl. Dis.*, **57**, 399–407, https://doi.org/10.7589/JWD-D-20-00057.

Walsh, J. E., T. J. Ballinger, E. S. Euskirchen, E. Hanna, J. Mård, J. E. Overland, H. Tangen, and T. Vihma, 2020: Extreme weather and climate events in northern areas: A review. *Earth-Sci. Rev.*, **209**, 103324, https://doi.org/10.1016/j.earscirev.2020.103324.

Waters, J. W., and Coauthors, 2006: The Earth Observing System Microwave Limb Sounder (EOS MLS) on the Aura satellite. *IEEE Trans. Geosci. Remote Sens.*, **44**, 1075–1092, https://doi.org/10.1109/TGRS.2006.873771.

Wegmann, M., and Coauthors, 2015: Arctic moisture source for Eurasian snow cover variations in autumn. *Environ. Res. Lett.*, **10**, 054015, https://doi.org/10.1088/1748-9326/10/5/054015.

Wehrlé, A., J. E. Box, A. M. Anesio, and R. S. Fausto, 2021: Greenland bare-ice albedo from PROMICE automatic weather station measurements and Sentinel-3 satellite observations. *Geol. Surv. Denmark Greenl. Bull.*, **47**, https://doi.org/10.34194/geusb.v47.5284.

White, J., J. E. Walsh, and R. L. Thoman Jr., 2021: Using Bayesian statistics to detect trends in Alaskan precipitation. *Int. J. Climatol.*, **41**, 2045–2059, https://doi.org/10.1002/joc.6946.

Whitfield, P. H., P. D. A. Kraaijenbrink, K. R. Shook, and J. W. Pomeroy, 2021: The spatial extent of hydrological and landscape changes across the mountains and prairies of Canada in the Mackenzie and Nelson River basins based on data from a warm-season time window. *Hydrol. Earth Syst. Sci.*, **25**, 2513–2541, https://doi.org/10.5194/hess-25-2513-2021.

Will, A., and Coauthors, 2020: The breeding seabird community reveals that recent sea ice loss in the Pacific Arctic does not benefit piscivores and is detrimental to planktivores. *Deep-Sea Res.*, **181–182**, 104902, https://doi.org/10.1016/j.dsr2.2020.104902.

WMO, 2022: Scientific assessment of ozone depletion: 2022. WMO GAW Rep. 278, 509 pp., https://csl.noaa.gov/assessments/ozone/2022/.

Wolken, G. J., and Coauthors, 2021: Glacier and permafrost hazards. *Arctic Report Card 2021*, T. A. Moon, M. L. Druckenmiller, and R. L. Thoman, Eds., NOAA Tech. Rep. OAR ARC-21-13, NOAA, 93–101, https://doi.org/10.25923/v40r-0956.

Yang, D., and Coauthors, 2022: Remote sensing from unoccupied aerial systems: Opportunities to enhance Arctic plant ecology in a changing climate. *J. Ecol.*, **110**, 2812–2835, https://doi.org/10.1111/1365-2745.13976.

Ye, H., D. Yang, A. Behrangi, S. L. Stuefer, X. Pan, E. Mekis, Y. Dibike, and J. E. Walsh, 2021: Precipitation characteristics and changes. *Arctic Hydrology, Permafrost and Ecosystems*, D. Yang and D. L. Kane, Eds., Springer, 25–59, https://doi.org/10.1007/978-3-030-50930-9_2.

Yu, L., and S. Zhong, 2021: Trends in Arctic seasonal and extreme precipitation in recent decades. *Theor. Appl. Climatol.*, **145**, 1541–1559, https://doi.org/10.1007/s00704-021-03717-7.

Zona, D., and Coauthors, 2023: Pan-Arctic soil moisture control on tundra carbon sequestration and plant productivity. *Global Change Biol.*, **29**, 1267–1281, https://doi.org/10.1111/gcb.16487.